An ALMA survey of submillimeter galaxies in the COSMOS field: Multiwavelength counterparts and redshift distribution

Drew Brisbin[1], Oskari Miettinen[2], Manuel Aravena[1], Vernesa Smolčić[2], Ivan Delvecchio[2], Chunyan Jiang[3,4,1], Benjamin Magnelli[5], Marcus Albrecht[5], Alejandra Muñoz Arancibia[6], Hervé Aussel[7], Nikola Baran[2], Frank Bertoldi[5], Matthieu Béthermin[8,9], Peter Capak[10], Caitlin M. Casey[11], Francesca Civano[12], Christopher C. Hayward[13,12], Olivier Ilbert[8], Alexander Karim[5], Olivier Le Fevre[8], Stefano Marchesi[14], Henry Joy McCracken[15], Felipe Navarrete[5], Mladen Novak[2], Dominik Riechers[16], Nelson Padilla[17,18], Mara Salvato[19], Kimberly Scott[20], Eva Schinnerer[21], Kartik Sheth[22], and Lidia Tasca[8]

1 Núcleo de Astronomía, Facultad de Ingeniería y Ciencias , Universidad Diego Portales, Av. Ejército 441, Santiago, Chile
2 Department of Physics, Faculty of Science, University of Zagreb, Bijenička cesta 32, 10000 Zagreb, Croatia
3 CAS Key Laboratory for Research in Galaxies and Cosmology, Shanghai Astronomical Observatory, Nandan Road 80, Shanghai 200030, China
4 Chinese Academy of Sciences South America Center for Astronomy, 7591245 Santiago, Chile
5 Argelander-Institut für Astronomie, Universität of Bonn, Auf dem Hügel 71, D-53121 Bonn, Germany
6 Instituto de Física y Astronomía, Universidad de Valparaíso, Avda. Gran Bretana 1111, Valparaíso, Chile
7 Laboratoire AIM, IRFU/Service d'Astrophysique - CEA/DSM - CNRS - Université Paris Diderot, Bât. 709, CEA-Saclay, 91191 Gif-sur-Yvette Cedex, France
8 Aix Marseille Université, CNRS, LAM (Laboratoire d'Astrophysique de Marseille) UMR 7326, 13388, Marseille, France
9 European Southern Observatory, Karl-Schwarzschild-Str. 2, 85748 Garching, Germany
10 Department of Astronomy, California Institute of Technology, MC 249-17, 1200 East California Blvd, Pasadena, CA
11 Department of Astronomy, The University of Texas at Austin, 2515 Speedway Blvd Stop C1400, Austin, TX 78712, USA
12 Harvard-Smithsonian Center for Astrophysics, 60 Garden Street, Cambridge, MA 02138, USA
13 Center for Computational Astrophysics, Flatiron Institute, 162 Fifth Avenue, New York, NY 10010, USA
14 Department of Physics and Astronomy, Clemson University, Kinard Lab of Physics, Clemson, SC 29634-0978, USA
15 Sorbonne Universités, UPMC Univ Paris 06, UMR 7095, Institut d'Astrophysique de Paris, F-75005, Paris, France
16 Astronomy Department, Cornell University, 220 Space Sciences Building, Ithaca, NY 14853, USA
17 Instituto de Astrofísica, Universidad Católica de Chile, Av. Vicuna Mackenna 4860, 782-0436 Macul, Santiago, Chile
18 Centro de Astro-Ingeniería, Universidad Católica de Chile, Av. Vicuna Mackenna 4860, 782-0436 Macul, Santiago, Chile
19 Max-Planck-Institut für Extraterrestrische Physik (MPE), Postfach 1312, D-85741 Garching, Germany
20 National Radio Astronomy Observatory, 520 Edgemont Road, Charlottesville, VA 22903, USA
21 Max-Planck-Institut für Astronomie, Königstuhl, 17, 69117 Heidelberg, Germany
22 NASA Headquarters, 300 E. St SW, Washington DC 20546, USA

September 11, 2017

ABSTRACT

We carried out targeted ALMA observations of 129 fields in the COSMOS region at 1.25 mm, detecting 152 galaxies at S/N≥5 with an average continuum RMS of 150 μJy. These fields represent a S/N-limited sample of AzTEC / ASTE sources with 1.1 mm S/N≥4 over an area of 0.72 square degrees. Given ALMA's fine resolution and the exceptional spectroscopic and multiwavelength photometric data available in COSMOS, this survey allows us unprecedented power in identifying submillimeter galaxy counterparts and determining their redshifts through spectroscopic or photometric means. In addition to 30 sources with prior spectroscopic redshifts, we identified redshifts for 113 galaxies through photometric methods and an additional nine sources with lower limits, which allowed a statistically robust determination of the redshift distribution. We have resolved 33 AzTEC sources into multi-component systems and our redshifts suggest that nine are likely to be physically associated. Our overall redshift distribution peaks at z ~2.0 with a high-redshift tail skewing the median redshift to $\bar{z}$=2.48±0.05. We find that brighter millimeter sources are preferentially found at higher redshifts. Our faintest sources, with $S_{1.25mm}$<1.25 mJy, have a median redshift of $\bar{z}$=2.18±0.09, while the brightest sources, $S_{1.25mm}$>1.8 mJy, have a median redshift of $\bar{z}$=3.08±0.17. After accounting for spectral energy distribution shape and selection effects, these results are consistent with several previous submillimeter galaxy surveys, and moreover, support the conclusion that the submillimeter galaxy redshift distribution is sensitive to survey depth.

Key words.

1. Introduction

Submillimeter bright galaxies (SMGs) represent a key population of star forming galaxies during the transitional epochs of galaxy assembly and peak star formation. Better understanding the physical characteristics of SMGs and their role in galaxy evolution has been an ongoing goal in astronomy since their initial discovery in low-resolution SCUBA observations (Smail et

al. 1997; Hughes et al. 1998; Barger et al. 1998). Infrared and submillimeter (submm) observations reveal that SMGs actively form stars at rates of approximately hundreds to thousands of $M_\odot$ yr^{-1} with correspondingly bright infrared luminosities $\gtrsim 10^{12}$ L$_\odot$ (Casey et al. 2014). Although they are similar in luminosity to local ultraluminous infrared galaxies (ULIRGs), local ULIRGs make up a very small fraction of the total star formation in the local universe and often have intense, compact star forming cores, whereas SMGs apparently compose a significant percentage of the star formation rate density in the early Universe, and may often host more extended star formation (e.g., Menéndez-Delmestre et al. 2009; Magnelli et al. 2011; Hodge et al. 2015, 2016). This suggests that our understanding of SMGs is crucial to elucidating the evolution of galaxies in the early universe.

Early investigations of SMGs have been hindered by the large single-dish beam sizes of (sub-)mm observations and the difficulty in finding counterparts at other wavelengths to determine galaxy properties and redshifts. A common procedure to pinpoint SMGs includes first surveying large areas of the sky using bolometer cameras mounted on single-dish (sub-)mm telescopes. The modest dish sizes of these telescopes ($\sim 10 - 30$m) imply that the typical beam size of such observations at wavelengths between 870μm and 1.2 mm range approximately from $11''$ to $30''$. Secondly, since the number of sources in optical images within a typical submm beam element is typically more than five, it has been necessary to filter the possible counterpart identification by pre-selecting either faint radio or 24μm sources identified in deep radio interferometer or infrared maps (see Ivison et al. 2002, 2007; Bertoldi et al. 2007; Biggs et al. 2011; Smolčić et al. 2012). The utility of radio pre-selection relies on the correlation between radio and infrared luminosities observed out to high redshifts (Helou et al. 1985; Carilli & Yun 1999; Yun et al. 2001), and assuming that both radio and infrared emission largely come from star formation activity. Finally, with the available radio or 24 μm counterpart, a nearby optical to near-infrared source is identified. Using the multiwavelength photometry typically available in the target submm fields, photometric redshifts are computed or optical-infrared follow-up spectroscopy is performed (e.g., Chapman et al. 2005). Alternatively, using various color-selection criteria shows promise as a method to identify potential optical SMG counterparts, especially in recent efforts using multiple color selections (Chen et al. 2016).

Due to the negative K correction in the Rayleigh-Jeans part of the dust spectral energy distribution (SED), the (sub)millimeter flux density remains almost constant with redshift out to $z \sim 10$ for a fixed IR luminosity. The radio and 24 μm emission, however, drop rapidly with redshift, becoming difficult to detect for most SMGs at $z = 3$. Therefore, apart from being observationally expensive, the identification of SMGs based on radio or infrared selection fundamentally biases any study of SMGs to relatively low redshift, and raises the possibility of counterpart mis-identification by association with unassociated radio sources. Due to these limitations, direct (sub)millimeter interferometric follow-up of single-dish-selected sources has been used to directly find accurate SMG positions and counterparts (Downes et al. 1999, Iono et al. 2006; Younger et al. 2007, 2009; Aravena et al. 2010; Smolčić et al. 2011, 2012a; Hodge et al. 2013; Miettinen et al. 2015a; Simpson et al. 2015).

Radio-identified SMGs typically lie at redshifts $z \sim$2-3 (e.g., Chapman et al. 2005; Wardlow et al. 2011). However, increasing evidence from time-consuming follow-up observations and proper source identifications working against selection biases from faint optical and radio counterpart identification has suggested a possible high-redshift tail ($z = 4 - 6$) for this population

(Daddi et al. 2009a,b; Capak et al. 2008, 2011; Coppin et al. 2009; Knudsen et al. 2010; Smolčić et al. 2011; Barger et al. 2012; Walter et al. 2012).

The Atacama Large Millimeter Array (ALMA) submm follow-up of 870 μm selected SMGs in the Extended *Chandra* Deep Field South (ECDFS), the ALESS survey, suggests that the SMG redshift distribution is similar to initial studies that were based on radio identification of SMGs, with a median redshift of 2.3-2.5 (Simpson et al. 2014; Fig. 2 therein), and a modest high-redshift tail at $z \gtrsim 3.5$. Several studies show evidence for the existence of an abundant $z > 4$ SMG population (Fig. 2; Capak et al. 2008, 2011; Schinnerer et al. 2008; Riechers et al. 2010, 2014; Aravena et al. 2010; Barger et al. 2012; Smolčić et al. 2011, 2012a,b). The existence of a high-redshift tail has received support from ALMA spectroscopic follow up of SMGs discovered with the South Pole Telescope (SPT), with initial survey samples finding a median redshift of 3.5, and a later, expanded sample finding a median value of 3.9 (Vieira et al. 2013; Weiß et al. 2013; Strandet et al. 2016). Both the initial and the expanded samples were selected with relatively high 1.4 mm flux limits of 20 and 16 mJy, respectively, strongly biasing the samples toward lensed systems and therefore systems at higher redshifts. Although lensing bias corrections revise the median redshift downward to z=3.1, this is still significantly higher than previous results (Strandet et al. 2016). Galaxies with very red SEDs, rising with wavelength out to 500 μm have also been shown to strongly correlate with galaxies at $z\gtrsim 4$, and their abundance in blind Herschel surveys similarly suggests a relatively abundant high-redshift tail (Riechers et al. 2013; Dowell et al. 2014; Asboth et al. 2016). The abundance of these high-redshift SMGs poses problems for cosmological models, given the difficulty in creating large amounts of dust, stellar mass, and galaxy halos at early cosmic times (e.g. Baugh et al. 2005; Younger et al. 2007; Dwek et al. 2011; Hayward et al. 2011; Hayward et al. 2013b; Ferrara et al. 2016).

These results clearly show the need for an independent, quantitative study of SMGs to minimize biases from previous studies. These include general cosmic variance from small sample sizes used in the mm follow-up of SMGs in COSMOS (Smolčić et al. 2012a,b), the CO spectroscopy of H-ATLAS sources and the SPT SMGs (Harris et al. 2012; Weiß et al. 2013), and in the submm follow-up studies of SMGs in the ECDFS (Weiß et al. 2009); as well as potential bias from the selection waveband, as mm-selected sources may lie at higher redshift than submm-selected ones (Greve et al. 2008), and from UV-NIR and radio counterpart identification.

In this paper, we present counterparts and redshifts for a sample of 129 SMGs that were initially discovered with the AzTEC camera on ASTE, and are now identified with high-resolution 1.25 mm ALMA imaging. Analyzed in conjunction with the most up-to-date panchromatic COSMOS data sets, we determine the multiwavelength counterparts and redshift distribution of our SMGs. In Sect. 2 we discuss our new observations and the ancillary multiwavelength COSMOS data. In Sect. 3 we present the methods of counterpart detection, in Sect. 4 we present the methods of our redshift determinations, and in Sect. 5 we discuss the redshift distribution of our sample in comparison to other SMG studies. This paper is one in a series of works analyzing this sample. M. Aravena et al. (in prep) discusses the observations, source catalog, and the flux distribution and clustering of the properties of sources revealed as multiples. C. Jiang et al. (in prep) analyzes the potential physical associations of those multiples. Miettinen et al. (2017a) presents a spatial analysis of the radio emission and its implications for star formation. Miettinen

et al. (2017b) presents the multiwavelength SEDs of the sample and discusses the physical characteristics we determine based on these.

We adopt a flat ΛCDM cosmology, with Ω_Λ=0.73, Ω_M=0.27, and H_0=72 km s^{-1} Mpc^{-1}.

2. Data

2.1. ALMA observations

We carried out targeted observations of 129 fields within the COSMOS region in cycle 2 ALMA operations at 1.25 mm (240 GHz). The observations were taken between 09 and 11 December 2014, under good weather conditions. These fields were drawn from Aretxaga et al. (2011) to include a flux-limited sample of AzTEC /ASTE sources with (deboosted) 1.1 mm flux densities ≥3.5 mJy covering the inner 0.72 square degrees of COSMOS.

Band 6 continuum observations were taken with an aggregate bandwidth of 7.5 GHz centered on 240 GHz. Our observations have fields of view of 26″3. We used the array in a relatively compact configuration using between 32 and 40 antennas, with a maximum baseline of ∼ 340 m. Initial continuum images were created from the visibilities by collapsing along the frequency axis and using natural weighting, resulting in a synthesized beam size of 1.6×0.93". Sources which were detected in single pixels at significance levels above 5σ were then masked with tight boxes around the source, and cleaned down to a 2.5σ threshold. All fields reach a homogenous RMS of ~150 μJy beam^{-1} at an effective wavelength of 1.25 mm.

After cleaning the resulting images, 152 sources were detected at ≥5σ, within the beam width of the initial AzTEC observations in each target field. Flux boosting due to the Eddington bias is expected to be very small at our achieved sensitivities and signal to noise. Simulation tests, performed by inserting false sources with signals in the range 2-40 σ confirm that at ≥5σ, flux boosting does not exceed map RMS. Therefore we did not apply any deboosting correction to our ALMA flux densities.

The sources, listed in Table 2, include 33 AzTEC sources that have been resolved into multiple components in the ALMA maps. These multi-component sources are noted by an alphabetical tag in order of their brightness (e.g., AzTEC/C1a is brighter than AzTEC/C1b). For an in-depth discussion of the ALMA observations and source data see M. Aravena et al. (in prep).

2.2. UV-NIR

We used the latest COSMOS photometric catalog (COSMOS2015 hereafter; Laigle et al. 2016), which includes photometric measurements from the UV/optical to IR in over 20 bands, including 6 broad bands (*B*, *V*, *g*, *r*, *i*, z^{++}), 12 medium bands, and 2 narrow bands, as well as *Y*, *J*, *H* and *Ks* data from the UltraVISTA Data Release 2, new HyperSuprime-Cam Subaru *Y* band, and new SPLASH 3.6 and 4.5 μm *Spitzer*/Infrared Array Camera (IRAC) data (Sanders et al. 2007; Capak et al. 2007; McCracken et al. 2012; Ilbert et al. 2013; see Laigle et al. 2016 for details). The sources listed in the catalog were selected using the $z^{++}YJHKs$ χ^2 stacked mosaic generated after point-spread function homogenization across all bands (except *GALEX* and *Spitzer*/IRAC). For the homogenized bands aperture photometry is reported in the catalog, as well as the correction of those to total magnitudes. The photometry in *GALEX* and *Spitzer*/IRAC bands was extracted using source-fitting techniques. Particular care was taken to robustly deblend the lower-

resolution IRAC photometry (using the tool IRACLEAN and prior positions extracted from the χ^2 image; see Laigle et al. 2016 for details).

2.3. Spectroscopy

We also use the COSMOS spectroscopic redshift catalog (M. Salvato et al., in prep.), which compiles all available spectroscopic redshifts, both available only to the COSMOS collaboration and from the literature (zCOSMOS (Lilly et al. 2007, 2009), IMACS (Trump et al. 2007), MMT (Prescott et al. 2006), VIMOS Ultra Deep Survey (VUDS, Le Fèvre et al. 2015; Tasca et al. 2017), Subaru/FOCAS (T. Nagao et al., priv. comm.), and SDSS DR8 (Aihara et al. 2011)). In total, over 97,000 spectroscopic redshifts are listed in the catalog, including 24 of our ALMA sources.

We also use the COSMOS spectroscopic redshift catalog (M. Salvato et al., in prep.), which compiles all available spectroscopic redshifts, both available only to the COSMOS collaboration and from the literature. This includes sources from the zCOSMOS bright survey, with sources selected based on an I_{AB} magnitude < 22.5 (Lilly et al. 2007, 2009); the IMACS survey of x-ray and radio selected AGN with I_{AB} < 24 (Trump et al. 2007); MMT which targeted quasars in the SDSS field with g band magnitudes <22.5 (Prescott et al. 2006); the VIMOS Ultra Deep Survey with sources selected for I_{AB} < 25 (VUDS, Le Fèvre et al. 2015; Tasca et al. 2017); Subaru/FOCAS (T. Nagao et al., priv. comm.); and SDSS DR8 (Aihara et al. 2011)). In total, over 97,000 spectroscopic redshifts are listed in the catalog, including 24 of our ALMA sources. At modest and high redshifts ($z \gtrsim 1$) the various I_{AB} and optical selections will probe rest frame UV emission. Therefore these spectroscopic surveys may present a selection bias against high-redshift sources with obscured dusty star formation. This emphasizes the need to adopt alternate methods for determining redshifts when spectroscopic results are unavailable.

3. ALMA source counterparts and photometry

3.1. UV-NIR counterparts and photometry

We searched for UV-radio counterparts to our 152 ALMA sources by cross-matching our ALMA positions to the COSMOS2015 catalog and the 3.6 μm *Spitzer*/IRAC selected catalog (Sanders et al. 2007) by relying on visual inspection of the optical to NIR images. Visual inspection proved necessary to avoid potential mismatches from foreground sources. In total, we find counterparts for 135/152 (94%) sources. Out of these, 97 were drawn from the COSMOS2015 catalog. An additional 38 ALMA sources had blended catalog photometry (in some of the optical or NIR bands) or were not present in the COSMOS2015 catalog. The latter occurs in case counterpart sources are present in bands blueward of z^{++} (e.g., *i*-band-detected sources; see e.g., AzTEC/C71b in Fig. 10) and/or redward of *Ks* (e.g., 3.6 μm; see e.g., AzTEC/C60b in Fig. 10), and not detected in the $z^{++}YJHK$ stacked mosaic (see Laigle et al. 2016). For these 38 counterparts we have specifically extracted the photometry in *u*, *g*, *r*, *i*, z^{++}, UltraVISTA *Y*, *J*, *H*, *Ks*, and *Spitzer*/IRAC 3.6, 4.5, 5.8 and 8.0 μm bands, and deblended where needed. This was done following the procedure described in detail in Smolčić et al. (2012a), and further applied in Smolčić et al. (2012b). Briefly, aperture and total magnitudes were first extracted for a sample of 100 randomly selected galaxies in the COSMOS field to calibrate the photometry extraction, that is, match it to that in the

COSMOS2015 catalog. The same tool was then applied to extract the photometry toward the 38 sources. Deblending was performed from case-to-case using prior positions, mostly fitting Gaussians to the blended sources, and subtracting the contaminating source (see Smolčić et al. 2012a for more details on the procedure). The extracted photometry for these sources is available in the Appendix in Tables 3 and 4. All magnitudes are given in AB units.

Zoomed images of the $z^{++}YJHKs$ stacked, *Spitzer*/IRAC, and *Spitzer*/MIPS 24 μm (as well as 1.4 and 3 GHz radio maps – see Sect. 3.2) for each source, with ALMA contours overlaid and the counterpart indicated are shown in Fig. 10 in the Appendix. A list of the counterparts is given in Table 2.

The median separation between the ALMA position and that of the counterparts in the COSMOS2015 catalog for the 97 matches is 0″.25, with an interquartile range from 0″.11 to 0″.46, and a maximum separation of 0″.95. Out of the COSMOS2015 counterparts only 14/97 (14%) have separations larger than 0″.6.

3.2. Radio counterparts

We also cross-matched our ALMA catalog with an internal VLA-COSMOS 1.4 GHz catalog (see Schinnerer et al. 2007) as well as a 3 GHz catalog (Smolčić et al. 2017).

Using search radii matching the mean resolutions in the radio surveys (1.8 and 0.75" at 1.4 GHz and 3 GHz respectively) we find 48 counterparts at 1.4 GHz and 115 at 3 GHz (in total 117 counterparts with either 1.4 GHz or 3 GHz counterparts). This includes eight sources which do not have a UV-NIR counterpart. The median separation between the ALMA and 3GHz (S/N$_{3GHz}$ $\geq$ 5) radio positions is only 0″.12, with an interquartile range of 0″.07 − 0″.18, while for the 1.4 GHz sources (S/N$_{3GHz}$ $\geq$ 5) the median separation is 0″.20 and the interquartile range is 0″.13 − 0″.30.

The better agreement between the ALMA positions and the radio positions (compared to ALMA and the UV-NIR positions) is expected as i) the astrometric accuracy in the radio mosaic (0″.01 at S/N$_{3GHz}$ > 20; Smolčić et al. 2017) is much higher than that in the $z^{++}YJHK$ stacked mosaic (better than 0″.15; Laigle et al. 2016), and ii) radio and mm wavelengths are both relatively unaffected by dust and are expected to trace roughly equivalent star-forming regions within the targeted galaxies. In practice, although the peak positions of radio and dust emissions appear to be coincident, the spatial scales appear different in the sense that the radio-emitting region of SMGs is on average about 2-4 times larger than that of the rest-frame FIR (see Miettinen et al. 2015b).

3.3. FIR - (sub-)mm counterparts and photometry

In addition to including flux densities from the 1.1 mm AzTEC observations (Aretxaga et al. 2011), we also cross-matched our ALMA sources with several submm and mm data sets including SCUBA 450 and 850 μm catalogs (Casey et al. 2013), LABOCA 870 μm (F. Navarrete, in prep.), SMA 890 μm data (Younger et al. 2007, 2009), MAMBO-2 1.2 mm (Bertoldi et al. 2007), and Herschel photometry from the Herschel Multitiered Extragalactic Survey (HerMES) and PACS Evolutionary Probe (PEP) projects (Oliver et al. 2012 and Lutz et al. 2011, respectively). In cases of our ALMA multiple sources we used the low-resolution photometry from AzTEC and LABOCA to establish upper limits on flux densities. For photometry from SCUBA and MAMBO-2 we established upper limits only if the reported detections were

within one beam width of multiple ALMA sources (7″, 15″, and 11″ for SCUBA 450 μm, SCUBA 850 μm, and MAMBO-2 respectively) and otherwise associated the single dish photometry with the ALMA source within half of a beam width. The Herschel photometry includes PACS and SPIRE photometry at 100,160, 250, 350, and 500 μm. Source photometry was extracted and deblended according to techniques detailed in Magnelli et al. (2013), based both on our ALMA positions and 24 μm *Spitzer* sources as prior positions. For the AzTEC/C6 multi-SMG system we also included 870 μm ALMA data from Bussmann et al. (2015).

4. Redshift determinations

4.1. Spectroscopic and photometric

In total we find spectroscopic redshifts for 30 objects; six of them are based on CO measurements: AzTEC/C1a (Yun et al in prep); C2a (D. Riechers, in prep); C5 (Yun et al. 2015); C6a and C6b (G. Guijarro, in prep; Wang et al. 2016); and C17 (Capak et al. 2008; Schinnerer et al. 2008). The source AzTEC/C3a has both a CO-determined spectroscopic redshift of 1.126 as well as an [O II] line-determined redshift of 1.124 (E. F. Jiménez Andrade, in prep.). As a working value we adopt z=1.125, although we note that it is possible this source lies at a much higher redshift (as indicated by its radio-mm and FIR SED determined redshifts) with the spectral lines coming from a foreground galaxy. The remainder of our spectroscopic redshifts are drawn from the COSMOS spectroscopic catalog.

For sources with at least four observed UV-NIR photometry bands we compute the photometric redshifts via a χ^2 minimization procedure using this photometry, extracted as described above, and a set of spectral templates developed in GRASIL (Silva et al. 1998; Iglesias-Paramo et al. 2007) and optimized for SMGs by Michałowski et al. (2010). The minimization is done using Hyper-z (Bolzonella et al. 2000)[1] assuming a Calzetti et al. (2000) extinction law, reddening varying from 0 to 5, and allowing for a redshift range of 0-7. We adopt this procedure from Smolčić et al. (2012a), Smolčić et al. (2012b), and Miettinen et al. (2015a). From the total χ^2 distribution for each source we construct the likelihood function ($\mathcal{L} \propto e^{-\chi^2/2}$) and extract the most likely photometric redshift (corresponding to the maximum likelihood point) and its error (corresponding to the interval encompassing 68% of the integrated likelihood function). The χ^2 distributions and likelihood functions are shown in Figs. 11 and 12 in the Appendix. We reject the photometric redshift likelihood functions for three of our sources, AzTEC/C62, C101b, and C118, because the fit failed to converge to any solutions within the redshift interval 0-7.

In Fig. 1 we compare the derived photometric redshifts with the available spectroscopic redshifts. As discussed in Sect. 4.5, the χ^2 distributions for photometric redshifts in several sources yield ambiguous photometric redshifts either because the redshift likelihood function has significant power at the extremes of our redshift range, or the likelihood function has multiple significant peaks indicating more than one likely redshift. Specifically, to determine whether a likelihood function has multiple significant peaks, we consider the set of redshift ranges (not necessarily continuous) which enclose 68% of the area in the likelihood function and also encompass the highest amplitudes of the likelihood function. If this set includes more than one redshift range then we compare the areas enclosed in each redshift range. If

---

[1] http://webast.ast.obs-mip.fr/hyperz/

any of the enclosed areas in these secondary peaks are greater than 33% of the largest enclosed area then we consider the likelihood function to be significantly multi-peaked. These ambiguous photo-z values include two sources which also have a spectroscopic redshift. For the time being we leave these sources out of our comparison. This leaves us with 24 sources from our sample to compare photometric and spectroscopic redshifts. We additionally include AK03 and Vd-17871 ($z_{\rm spec}$=4.757 and 4.622, respectively) (Karim et al. in prep, Smolčić et al. 2015) in our comparison. These were fit photometrically in an identical manner and are included to improve the robustness of our fit. In general our photometric and spectroscopic redshifts are consistent with a relatively small deviation of $\langle \Delta z/(1 + z_{\rm spec}) \rangle$=0.096. Previously Smolčić et al. (2012a) found a weak trend with redshift indicating that the photometric redshifts are slightly underestimated at low redshifts and slightly overestimated at high redshifts, consistent with our current data. Weighing by the photometric redshift uncertainty we find

$$z_{\rm spec} = 0.95 \times z_{\rm phot} + 0.20. \tag{1}$$

At $z_{\rm phot}$ ~6 this results in a minor correction downward by Δz=0.09, and at $z_{\rm phot}$ ~1 this results in a correction upward by Δz=0.15. In Fig. 1 we show the raw uncorrected $z_{\rm phot}$ as well as the systematic offset trend, Eq. 1. In Table 2 and throughout the remainder of the paper we use the corrected photometric redshifts. The correction is applied to the nominal $z_{\rm phot}$ values, their error bars, and the underlying redshift likelihood functions.

4.2. AGN templates and X-ray detected sources

Eight sources from our sample are also clearly associated with detections by the *Chandra X-ray Observatory* (Elvis et al. 2009, Puccetti et al. 2009, Civano et al. 2012, Civano et al. 2016). The likely presence of an active galactic nucleus (AGN) powering their X-ray emission could also significantly affect their UV-NIR SEDs and thus the reliability of our photometric redshift determinations. Marchesi et al. (2016) used the combined X-ray and UV-IR SEDs to fit photometric redshifts based on the procedure from Salvato et al. (2011). Using SED templates based on either normal galaxies (Ilbert et al. 2009) or hybrid AGN and galaxy emission (Salvato et al. 2009) they established reliable photometric redshifts for seven of the sources (with one source lacking an optical counterpart and therefore a photometric redshift). Based on their careful treatment of X-ray-detected sources, we consider their photometric redshift determinations of these seven sources to be superior to ours. Table 2 notes the Salvato et al. (2011) redshifts for these sources. Five of the seven sources have spectroscopic redshifts, so the Marchesi et al. (2016) photometric redshifts represent the best redshift determination for only two sources. An additional source, AzTEC/C74a, is also marginally associated with an X-ray source at a separation of 1″7. This separation is larger than expected and may be a spurious association, so we consider our photometric redshift ($z_{\rm phot}$ = 2.10) in our analysis, but also note the photometric redshift determined by Marchesi et al. (2016) (z = 2.948) in Table 2.

4.3. Radio - millimeter redshifts

We also consider redshifts determined by the radio - millimeter spectral index method pioneered by Carilli & Yun (1999, 2000). We follow the method presented in Aravena et al. (2010) in using the modeled SED of Arp 220 as an emission template
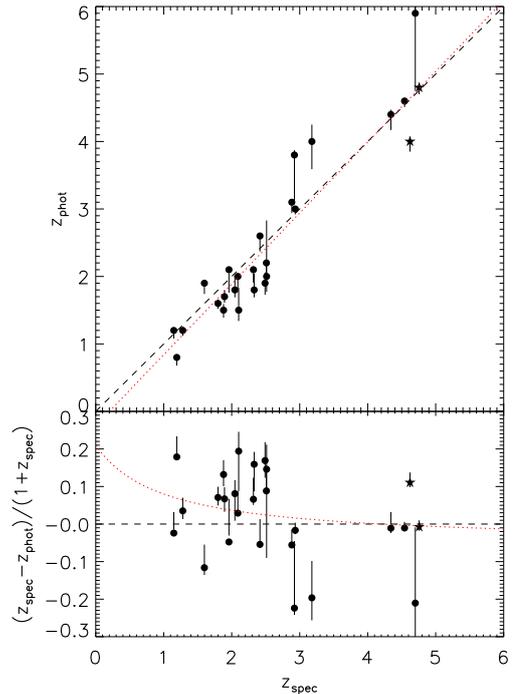

Fig. 1: (Top panel) Measured $z_{\rm phot}$ as a function of $z_{\rm spec}$. $z_{\rm phot}$=$z_{\rm spec}$ is plotted as a dashed black line. Four sources from our sample with ambiguous photometric redshifts have been ignored. We have also included two sources from outside our sample, AK03 and Vd-17871 ($z_{\rm spec}$=4.757 and 4.622, repectively), plotted as stars. These were fit photometrically in an identical manner and are included to improve the robustness of our fit. We detect a slight systematic offset with $z_{\rm spec}$ (Eq. 1) plotted as a red dotted line. (Bottom panel) $\Delta z/(1+z_{\rm spec})$ as a function of $z_{\rm spec}$. With data and Eq. 1 plotted as in the top panel.

which we vary in redshift to model the observed spectral index relating our 240 GHz ALMA continuum to radio continuum. This model is closely matched by a modified black body dust emission with $T_{\rm d}$=45 K and dust emissivity index β=1, although the redshift determination is not sensitive to modifications in β=1-2.

In Fig. 2 we show the functions relating radio to mm spectral indices, α, to redshift. Spectral index is defined as $\alpha_y^x \equiv \log(S_x/S_y)/\log(\nu_x/\nu_y)$ where we have used x=240 GHz and both y=3 GHz and y=1.4 GHz. We calculate the uncertainty based on the intrinsic uncertainty of the observed spectral index, as well as from the dust SED model, assuming a range of dust temperatures from 25 to 60 K, using the greater of the two uncertainty ranges. We note that at lower dust temperatures the spectral index actually turns over at z ~5.7 with maximum spectral indices $\alpha_{3{\rm GHz}}^{240{\rm GHz}}$ ~1.06 and $\alpha_{1.4{\rm GHz}}^{240{\rm GHz}}$ ~0.8. For spectral indices above these values we have an undefined upper limit on our redshift. In these cases we assume an upper limit of z=7, which coincides with the maximum photometric redshift considered. In sources without detected radio counterparts we use the 3σ detection thresholds of the radio surveys to establish lower limits on α and therefore lower limits on the redshift. Radio-mm determined redshifts are also included in Table 2.
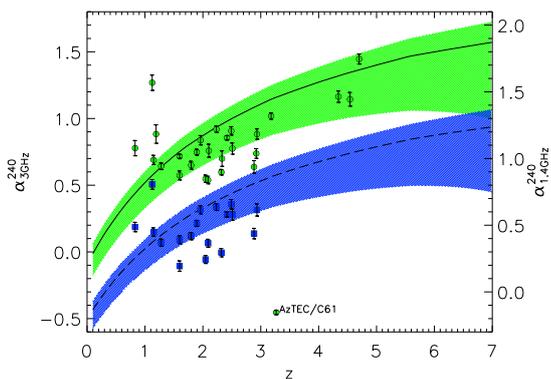
Fig. 2: Modeled radio-mm spectral indices, α as a function of redshift. The solid and dashed lines correspond to $\alpha_{3\mathrm{GHz}}^{240\mathrm{GHz}}$ and $\alpha_{1.4\mathrm{GHz}}^{240\mathrm{GHz}}$, respectively, while the green and blue hashed regions correspond to the uncertainty range due to varying dust SED temperatures spanning 25 to 60 K. The axes for the two spectral indices have been offset for clarity. Green circles and blue squares indicate represent those sources in our sample with spectroscopic redshifts which are detected at 3 and 1.4 GHz respectively. AzTEC/C61 demonstrates an inverted radio spectrum and is suspected of hosting an AGN, so its extreme spectral index is not used as a redshift indicator (Miettinen et al. 2017a).

4.4. Far-infrared redshifts

Dust warmed by star formation in SMGs emits in a characteristic modified black body spectrum typically peaking around 60-120 μm (e.g., Pope et al. 2008). Despite the breadth of this continuum feature, broad-band FIR to mm photometry has been used to select candidate high-redshift galaxies and even estimate the source redshifts (Greve et al. 2012; Weiß et al. 2013; Riechers et al. 2013; Dowell et al. 2014; Asboth et al. 2016; Ivison et al. 2016; Su et al. 2016). This estimate may be particularly useful in choosing from multiple photo-z solutions (in particular, low vs. high redshft).

We constructed FIR SEDs using our ALMA 1.25 mm detections along with FIR - (sub-)mm observations from the literature (see Sect. 3.3). For a robust fit to the FIR peak we required that sources be detected in at least four bands without obvious deviations from a plausible thermal dust SED (i.e., any anomalously low flux densities causing a dip in the middle of the SED were not counted toward the criterion of four good detections). We also required that the observations trace out a rising and falling SED to ensure sufficient wavelength coverage to locate the peak.

To calibrate the SED fits we used a training set of 16 sources with spectroscopic redshifts that met our criteria. This includes 15 sources from our COSMOS ALMA sample and an additional galaxy, Vd-17871, at z=4.622 (Smolčić et al. 2015). This additional source, which is similar to the sources in our sample in that it is a COSMOS SMG, is included to improve the strength of the SED fits at redshifts z>4, for which we have few spectroscopic candidates that meet our FIR fitting criteria. We fit the observed SED of each source with a simple parabola through χ^2 minimization and recorded the wavelength of the parabola peak, $\lambda_{\mathrm{observed\ peak}}$ along with an uncertainty range encompassing 68% of the resulting likelihood distribution for $\lambda_{\mathrm{observed\ peak}}$. As shown in Fig. 3 we observe a strong positive correlation in our training set between peak wavelength and spectroscopic redshift with a Pearson correlation coefficient R=0.88. We fit this

correlation with a straight line, $z = \mathrm{m} \times \lambda_{\mathrm{peak}} + \mathrm{b}$, and find m = 0.0187 ± 0.0007, and b = −3.8 ± 0.2.
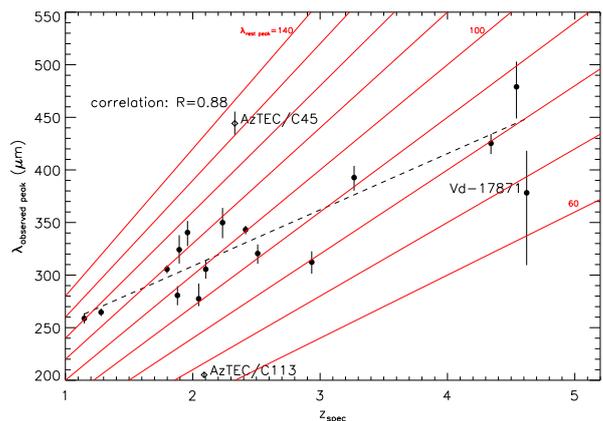

Fig. 3: Parabolic-fitted peak wavelength, $\lambda_{\mathrm{observed\,peak}}$, vs. z_{spec} for the sources in our z_{FIR} training set. AzTEC/C113 and AzTEC/C45 are plotted although they were not used in our training set since they are extreme outliers. The source Vd-17871 is included in the training set since it fits our training set selection criteria and is a similar COSMOS field SMG (Smolčić et al. 2015). The fitted correlation $z = \mathrm{m} \times \lambda_{\mathrm{peak}} + \mathrm{b}$ is shown as a dashed line. Tracks of constant rest wavelength are overlaid as red lines progressing in intervals of 10 μm from $\lambda_{\mathrm{restpeak}}$=60 μm in the lower right to 140 μm in the upper left.

The sources AzTEC/C113 (z_{spec}=2.09) and AzTEC/C45 (z_{spec}=2.33) also meet our fitting criteria, however they are both outliers in the overall trend of wavelength peak versus redshift. AzTEC/C113 has the shortest rest-wavelength peak in our entire training set, and AzTEC/C45 has the longest. Although the correlation between spectroscopic redshift and peak wavelength remains strong even if these sources are included, (R=0.73), the overall fit suffers and is much poorer when compared to the larger sample of photometric redshifts. We therefore exclude them from our training set.

The correlation between λ_{peak} and redshift remains strong even in a more diverse set of sources from the literature, although the scatter increases. In Table 1 and Fig. 4 we note the z_{FIR} values calculated for our AzTEC sources with spectroscopic redshifts along with SMG sources from the literature. These include several highly lensed star-forming SPT sources. The correlation coefficient in this expanded sample is R=0.72 (R=0.43 when our training set sources are excluded). In this extended sample of sources we find that the uncertainty derived from standard propagation of error based on the uncertainty of m, b, and λ_{peak} is generally smaller than the observed discrepancy between z_{FIR} and z_{spec}. This is not surprising as, at any given redshift, a diverse population of galaxies will exhibit a wide range of FIR dust temperatures and we should not expect a one-to-one correspondence between $\lambda_{\mathrm{observed\ peak}}$ and redshift. Since this is not considered in our fitting model we implement an empirically determined uncertainty that is 2.5 times larger than the error derived through standard error propagation. The expanded error bars encompass 68% (28 out of 41) of the tested literature sources with spectroscopic redshifts.

Our straight-line fit between z_{spec} and $\lambda_{\mathrm{observed\ peak}}$ implies a continuous shift of the dust emission peak to shorter rest-frame wavelengths at high redshift. Although this is consistent with predictions of some models of galaxy formation (e.g., Béther-
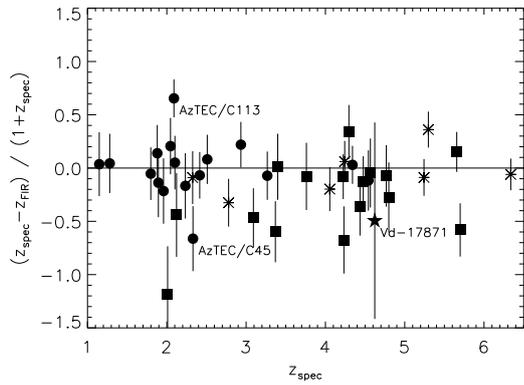
:

Fig. 4: Comparison of z_{FIR} with spectroscopic redshifts. Circles indicate AzTEC/C sources, squares represent SPT sources (Weiß et al. 2013), and asterisks represent galaxies from other surveys (see Table 1). The star represents Vd-17871 (also included in our training set). The error bars show the error due to the combined uncertainty of λ_{peak} and the linear relation between λ_{peak} and z_{spec} multiplied by a factor of 2.5× such that 68% of the sample has consistent values of z_{FIR} and z_{spec}.

min et al. 2012) we caution against over interpretation based on these data. Our simple model does not attempt to characterize the physical dust conditions such as mass, emissivity, multiple dust components, and so on. which would be required for a detailed investigation into the evolution of galaxy SEDs. We also attempted fits to the FIR SEDs using more advanced equations, including third degree polynomials and modified blackbodies. While these more complex models fit individual SEDs better, the overall correlation between spectroscopic redshift and FIR model redshift is strongest with the simple parabola-fitting method. We fit 81 sources in our sample with FIR redshifts. Although the FIR method is the primary redshift determination for only seven sources, it also helps constrain the photometric redshifts in an additional seven sources (see Sect. 4.5).

4.5. Redshift comparison

We consider the redshift determination methods in decreasing order of reliability: spectroscopic, UV-NIR photometric, FIR dust peak, and radio-mm spectral index. In several cases, however, the photometric redshift is ambiguous due to likelihood functions in which the confidence interval extends to either $z=0$ or $z=7$, or in which there are multiple significant local maxima yielding more than one potential redshift solution. Radio-mm and FIR redshift determinations can help refine these ambiguous photometric redshifts. For these sources we construct a final synthetic redshift likelihood function by convolving the photometric redshift likelihood function with a likelihood function based on the next most reliable redshift indicator. For sources with z_{FIR} we use Gaussians with σ based on the z_{FIR} uncertainty, and for sources with radio-mm redshifts we use two Gaussians stitched together in the middle with σ defined by the asymmetric error bars. We have constructed these synthetic redshifts for 17 sources. They are noted in Table 2 and their likelihood functions are overlaid on the photometric likelihood functions in Figs. 11 and 12.

Four of these source redshifts remain ambiguous even after constructing z_{synth} (noted in Table 2). In general they are characterized by large uncertainties and treated with caution in our analysis that follows. One of these sources, AzTEC/C8b with

Table 1: z_{FIR} and z_{spec} for sources in Fig. 4.

Source	z_{FIR}	z_{spec}	Ref.
AzTEC/C52	1.1 ± 0.6	1.148	COSMOS2015
AzTEC/C59	1.2 ± 0.6	1.280	COSMOS2015
AzTEC/C65	1.9 ± 0.7	1.798	COSMOS2015
AzTEC/C124	1.5 ± 0.8	1.880	COSMOS2015
AzTEC/C112	2.3 ± 0.9	1.894	COSMOS2015
AzTEC/C84b	2.6 ± 0.9	1.959	COSMOS2015
SPT0452-50	5.6 ± 1.4	2.010	Weiß et al. (2013)
AzTEC/C47	1.4 ± 0.8	2.047	COSMOS2015
AzTEC/C113	0.1 ± 0.5	2.090	COSMOS2015
AzTEC/C95	1.9 ± 0.8	2.102	COSMOS2015
SPT0551-50	3.5 ± 1.2	2.123	Weiß et al. (2013)
AzTEC/C118	2.8 ± 1.0	2.234	COSMOS2015
Cosmic Eyelash	2.6 ± 0.8	2.326	Swinbank et al. (2010) Ivison et al. (2010)
AzTEC/C45	4.5 ± 1.0	2.330	COSMOS2015
AzTEC/C36	2.6 ± 0.7	2.415	COSMOS2015
AzTEC/C25	2.2 ± 0.8	2.510	COSMOS2015
SMM J0658	4.0 ± 0.8	2.779	Johansson et al. (2012)
AzTEC/C67	2.1 ± 0.8	2.934	COSMOS2015
SPT0103-45	5.0 ± 1.1	3.092	Weiß et al. (2013)
AzTEC/C61	3.6 ± 1.0	3.267	COSMOS2015
SPT0529-54	6.0 ± 1.3	3.369	Weiß et al. (2013)
SPT0532-50	3.3 ± 1.4	3.399	Weiß et al. (2013)
SPT2147-50	4.1 ± 1.5	3.760	Weiß et al. (2013)
GN20	5.1 ± 1.0	4.055	Tan et al. (2014)
SPT0418-47	4.6 ± 1.1	4.225	Weiß et al. (2013)
SPT0113-46	7.8 ± 1.7	4.233	Weiß et al. (2013)
ID 141	3.9 ± 1.0	4.243	Cox et al. (2011)
SPT0345-47	2.5 ± 1.3	4.296	Weiß et al. (2013)
AzTEC/C5	4.2 ± 1.0	4.341	Yun et al. (2015)
SPT2103-60	6.4 ± 1.5	4.436	Weiß et al. (2013)
SPT0441-46	5.2 ± 1.3	4.477	Weiß et al. (2013)
AzTEC/C17	5.2 ± 1.6	4.542	Schinnerer et al. (2008)
SPT2146-55	4.8 ± 1.8	4.567	Weiß et al. (2013)
Vd-17871	3.3 ± 2.7	4.622	Smolčić et al. (2015)
SPT2132-58	5.2 ± 1.7	4.768	Weiß et al. (2013)
SPT0459-59	6.4 ± 1.9	4.799	Weiß et al. (2013)
HLSJ091828.6+514223	5.8 ± 1.1	5.243	Combes et al. (2012)
AzTEC3	3.0 ± 1.1	5.298	Riechers et al. (2010)
SPT0346-52	4.6 ± 1.2	5.656	Weiß et al. (2013)
SPT0243-49	9.6 ± 1.7	5.699	Weiß et al. (2013)
HFLS3	6.8 ± 1.1	6.337	Riechers et al. (2013)

photometric (and synthetic) redshift solutions at $z \sim 1$ and 1.8, is also included in the COSMOS2015 catalog, with a photometric redshift of 2.02. Furthermore, fitting its panchromatic SED (covering UV-radio wavelengths) shows a significantly better fit with a redshift of $z \sim 2$ (Miettinen et al. 2017b). So for this source we suggest the higher synthetic z solution with an uncertainty interval that extends to the lower peak as well, $z=1.8^{+0.2}_{-0.8}$.

In Fig. 5 we compare the five main redshift determinations among our sample. Ultraviolet-NIR photometric redshifts have a well established record of use (e.g., Smolčić et al. 2012a,b, Ilbert et al 2009), and they compare well to spectroscopic redshifts in our sample. AzTEC/C61, which has an ambiguous photometric redshift likelihood function that extends to $z=7$, is the one significant outlier. The synthetic redshifts for AzTEC/C61 are in much better agreement with its spectroscopic redshift. The radio-mm redshift determinations based on either 3 GHz or 1.4 GHz compare less favorably with spectroscopic redshifts. The comparison between redshifts derived from FIR SEDs and spectroscopic redshifts illustrates the good correlation found in our training set.

For completeness we note all available redshifts in Table 2. For each source in the analysis that follows we consider the most reliable redshift available. Our resulting sample of 152 sources and their best-determined redshifts then includes 30 sources with spectroscopic redshifts, 88 determined by our UV-NIR photometric methods, 2 based on the photometric redshifts established

by Marchesi et al. (2016), 11 synthetic redshifts, 7 determined from the FIR dust peak, 9 with lower limits determined from $\alpha_{1.4\mathrm{GHz}}^{240\mathrm{GHz}}$, and 5 with redshifts from $\alpha_{3\mathrm{GHz}}^{240\mathrm{GHz}}$.

4.6. Redshift distribution

In Fig. 6 (top panel) we show the redshift distribution for our SMG sample. To investigate possible contamination of the redshift distribution due to inclusion of uncertain redshifts, we show histograms of a strict sample, including only sources with spectroscopic or unambiguous photometric redshifts (including both our own photometric redshifts and those from Marchesi et al. 2016), as well as an extended sample which includes all sources with redshift determinations or lower limits. The nine sources with lower limits are included in the histogram bin containing their limit. The strict sample consists of 116 sources and has a median redshift $\tilde{z}=2.3\pm0.6$ (this uncertainty range corresponds to the median absolute deviation). The extended sample consists of 152 sources with a median of $\tilde{z}=2.2\pm0.6$. The complementary set of 36 sources which are in the extended sample but excluded from the strict sample does appear to preferentially skew towards low redshifts. This is almost entirely due to our including those sources with redshift lower limits. When we exclude those nine sources with only redshift lower limits, a Kolmogorov-Smirnov (KS) test comparing the strict sample to the 27 sources in the complementary sample finds an associated probability of 0.32, providing no evidence that the samples are drawn from a different underlying population. In the same panel we also plot the redshift density likelihood function of the extended sample. This distribution is the cumulative addition of each source's individual redshift likelihood, constructed as in Miettinen et al. (2015a). Sources with spectroscopic redshifts are included as Dirac delta functions centered at z_{spec}. Photometric and synthetic redshifts are included using their underlying likelihoods, and radio-mm and FIR-based redshifts are included as Gaussians with standard deviations according to their associated redshift errors (as in the construction of the synthetic redshifts – see Sect. 4.5). The advantage of this estimation of the redshift distribution is that less certain redshift determinations affect the overall redshift distribution less, and redshifts with significantly asymmetric positive and negative error bars can be appropriately accounted for. Sources with only lower limits are each included as a uniform likelihood extending from their lower limits to $z=7$ which avoids the problem of inappropriately reducing the overall redshift distribution (seen in the slight difference between the median values of the strict and extended histogram samples). We note that regardless of whether this small number of lower limits is included, our median redshift remains unchanged to two significant figures. Redshifts are then randomly sampled from each of the 152 redshift likelihood functions and the sample median is determined in each of 1000 Monte-Carlo trials. The median value across all the Monte-Carlo runs is then reported as the redshift density likelihood function median, and the uncertainty corresponds to the range which encompasses 68% of the Monte-Carlo runs (i.e., 680 sample medians). Since this distribution properly takes into account the significant and asymmetric uncertainty in many of our redshifts, we take this to be the most accurate description of the sample redshift distribution. The median of this distribution is $\tilde{z}=2.48\pm0.05$.

With our large sample size, we are able to subdivide our sample and directly examine how the redshift distribution is affected by the underlying flux density limit. In the bottom three panels of Fig. 6 we divide our sample roughly in thirds by flux density, showing the redshift distribution of sources with $S_{1.25\mathrm{mm}}<1.25$
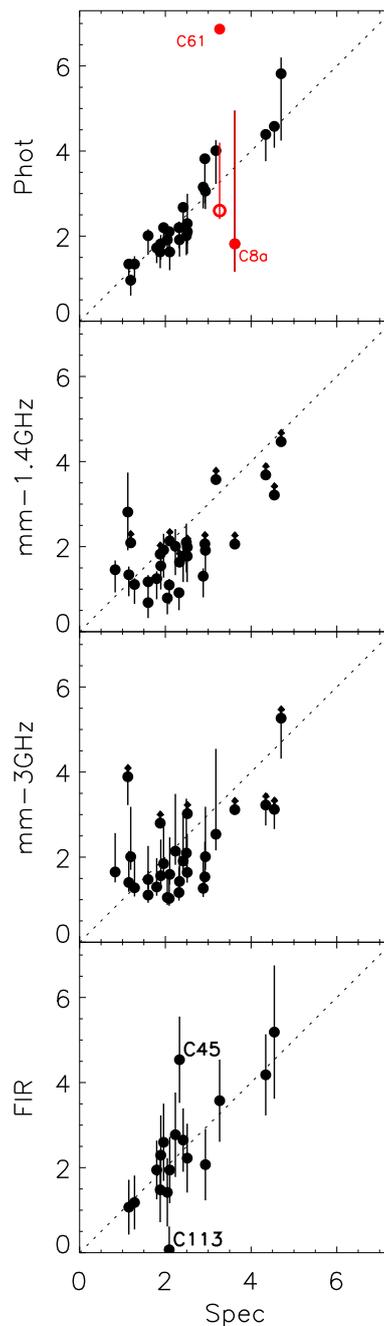
Fig. 5: A comparison of the various redshift methods used in this work. For the top plot, photometric vs. spectroscopic, we have highlighted in red sources AzTEC/C61 and C8a which have ambiguous photometric redshifts. Source C61 also has a synthetic redshift, which we have plotted as an open red circle. The large negative error bar for the photometric redshift of AzTECC61 has been suppressed for clarity. In the bottom plot, FIR vs. spectroscopic, we have noted AzTEC/C113 and AzTEC/C45 which, despite meeting our criteria for being part of the training set, proved to be a significant outliers and were therefore ultimately ignored in our z vs. λ_{peak} fit. The dashed line in each panel indicates a 1:1 redshift match.
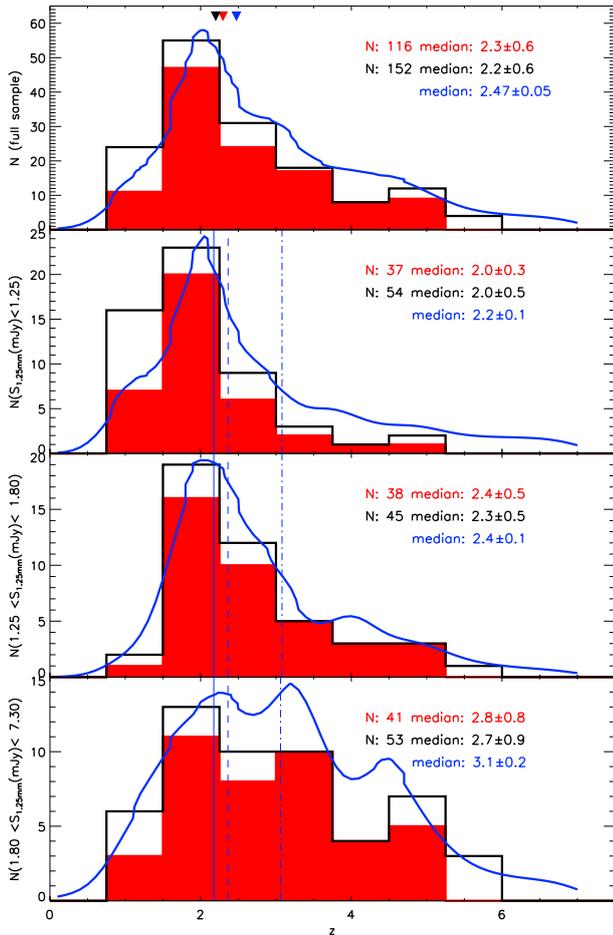
Fig. 6: (*Top panel:*) Redshift distribution of our full SMG sample. The filled red histogram includes only the 116 sources with spectroscopic or unambiguous photometric redshifts, our strict sample. The solid black line represents our extended sample, which additionally includes sources with radio-mm redshifts, FIR dust peak SEDs, less certain photometric redshifts, and sources which only have redshift lower limits. The smoothed blue line gives the redshift density likelihood function of the extended sample. Median values are noted in the figure and plotted as red, black, and blue colored triangles for the strict sample histogram, extended sample histogram, and the extended sample redshift density distribution (note that the strict and extended sample histogram medians are nearly coincident). (*Bottom three panels:*) The redshift distributions of our samples subdivided by their ALMA 1.25 mm flux density. Sources with flux densities $S_\nu < 1.25$ mJy are shown in the second panel, 1.25 mJy $\leq S_\nu \leq 1.8$ mJy in the third, and $S_\nu > 1.8$ mJy in the bottom panel. Our strict sample histogram, extended sample histogram, and redshift density likelihood function are plotted as in the top panel. Three blue vertical lines spanning all three panels show the redshift density distribution median redshifts for the various subsamples. Solid, dashed, and dot-dashed lines correspond to the faintest to brightest flux density divisions respectively.

mJy, 1.25 mJy $<S_{1.25mm}<1.8$ mJy, and $S_{1.25mm}>1.8$ mJy. The three flux density selections respectively include 37, 38, and 41 sources from our strict sample, and 54, 45, and 53 sources from our extended sample. The redshift density medians clearly increase with flux density, from $\tilde{z}=2.2\pm0.1$ in the faintest sample to $\tilde{z}=3.1\pm0.2$ in the brightest sample, with strict and extended samples presenting median values almost identical to each other. A KS test comparing the brightest and faintest extended (strict) samples reveals an associated probability of 1.4e-3 (2.3e-4) strongly indicating that the underlying redshift distributions in the brightest and faintest subsamples are different.

4.7. Multi-component SMGs

Several of our AzTEC / ASTE sources are resolved into multiple components by ALMA. Given that a certain fraction of single-dish detected SMGs are expected to be composed of multiple systems in chance alignment, it is reasonable to ask how many of our multi-component sources are due to chance alignment and how many may be physically related (Wang et al. 2011; Hayward et al. 2013a). Here we discuss potential physical associations based only on the source redshifts. For a discussion of the flux distribution among sources with multiple components see M. Aravena et al. (in prep), and for a comparison of our sample with clustering and evolutionary models see C. Jiang et al. (in prep). A total of 28 fields in our observations revealed two components within the area of the AzTEC primary beam. Among those resolved into two components, we consider nine pairs to be likely physical associations. The redshifts of the components in these paired systems are consistent with being identical, and the individual redshift uncertainties are less than ±1. These systems include AzTEC/C 13, 22, 24, 28, 43, 48, 80, and 101. We also consider AzTEC/C 6 to be a likely physical association. Although the components C6a and C6b are separated by $\Delta z=0.023$, just slightly larger than the threshold Hayward et al. (2013a) suggest for differentiating between physical associations and chance alignment, the system consists of at least five submm-bright sources (Bussmann et al. 2015) and is also located within an X-ray emitting cluster with 17 spectroscopically confirmed member galaxies (Casey et al. 2015; Wang et al. 2016). The median separation of the pair components in all of our likely associations is 6″5 (53 kpc at our median redshift, $\tilde{z}=2.47$) with an interquartile range of 4″9 to 11″3. The AzTEC/C6 and C22 systems, in particular, are likely to contain physically associated components, as they each have spectroscopically confirmed components with similar redshifts. In the case of C22, the two components also appear to be connected by a radio-emitting bridge, which supports a scenario where the sources are gravitationally interacting (Miettinen et al. 2015b; Fig. 2 therein (their source AzTEC11); and Miettinen et al. 2017a).

An additional ten pairs are possible physical associations. Although their component redshifts are less well determined with uncertainties greater than ±1, they are within 1σ of one another. Their median component separation is 13″1 (106 kpc) with an interquartile range of 6″5 to 19″2. Nine source pairs have larger redshift offsets, showing no signs of physical association ($\Delta z>1\sigma$). Their median component separation is 12″4 (100 kpc) with an interquartile range of 8″0 to 17″0.

An additional five fields revealed three components. Three of these systems show tentative evidence that they may be physically associated. The AzTEC/C9 triplet consists of two sources with spectroscopic redshifts of 2.922 and 2.884, and a third source with $z_{phot} = 2.68^{+0.24}_{-0.51}$. Each of the components lies within 13″ (101 kpc at $z=2.9$) of its closest neighbor. Although

these redshifts differ by more than is typical for physical associations, the system lies within a BzK galaxy over-density. AzTEC/C90 includes three components within 13" (106 kpc at z=2.4) of one another and with photometric redshifts between 2.1 and 2.8. The AzTEC/C55 system includes one component with only a redshift lower limit, and two components with photometric redshifts consistent with being identical. The components of this system are separated by up to 17''2 (141 kpc at z=2.55). The final triplet systems show no evidence of physical association. AzTEC/C10 includes components separated by up to 17''4 (141 kpc at our median redshift, $\bar{z}$=2.47). Two components have effective lower limits from their radio-mm spectral indices ($z_{3-240\text{GHz}} = 3.40^{+3.60}_{-0.59}$ and $z_{3-240\text{GHz}} = 3.37^{+3.63}_{-0.52}$ for C10a and C10c, respectively) and C10b has a redshift $z_{\text{synth}} = 2.90^{+0.30}_{-0.90}$, providing no useful evidence to evaluate their physical association. AzTEC/C3 includes components separated by up to 20" (163 kpc). One component has only a redshift lower limit, one component, C3a, has a tentative $z_{\text{spec}} = 1.125$ (as discussed in Sect. 4.1), and one component has a radio-mm redshift, $z_{3-240\text{GHz}} = 2.03^{+1.19}_{-0.31}$, which suggests that the components are a chance alignment.

5. Discussion

There is considerable discussion surrounding the differences in reported SMG redshift distributions and their associated selection biases. Several studies of SMG redshifts suggest a positive correlation between flux density and median redshift (Ivison et al. 2002, Pope et al. 2005, Younger et al. 2007, Biggs et al. 2011, Smolčić et al. 2012b), as well as a correlation between longer, mm-wavelength-based selections and higher redshifts (Blain et al. 2002, Zavala et al. 2014, Casey et al. 2013), while other works have not borne out this trend (Simpson et al. 2014, Miettinen et al. 2015a).

In Fig. 7 we compare the redshift distribution of our extended sample to previous SMG survey results. The sources represented in our redshift distribution are subject to two selection criteria: they were initially selected at or above a deboosted flux limit of 3.5 mJy at 1.1 mm on the ASTE instrument, and later detected by ALMA at 1.25 mm reaching a 5σ sensitivity of 750 μJy beam^{-1}. While the initial 1.1 mm selection is a more restrictive flux limit, several sources are resolved as multiples by ALMA, indicating that the the achieved ALMA sensitivity also effects our sample selection.

Chapman et al. (2005) includes 76 SMGs selected from 850 μm SCUBA surveys which were identified with VLA radio counterparts and spectroscopically observed with Keck I to determine redshifts. Their SCUBA sample reaches a characteristic flux limit of 3 mJy, equivalent to 1 mJy at our selection wavelength of 1.25 mm. The radio observations reach a flux limit of 30 μJy. It is expected that the submm limit is most restrictive for SMGs at low redshifts, while the radio limit is most restrictive at high redshift. Directly comparing our sample with theirs is complicated by the redshift desert at z~1.5 for which few optical spectroscopic identifications were accessible, resulting in significant incompleteness in their sample over this range. After correcting for this incompleteness their calculated median redshift is $\bar{z}$=2.2. We have attempted to compensate for the redshift desert in the histogram representation of their redshift distribution in Fig. 7 in the same spirit as Smolčić et al. (2012b). In addition to the original Chapman et al. (2005) sample we augment the redshift distribution with 19 SMGs deliberately targeted in the redshift desert by Banerji et al. (2011), weighting the samples

by their survey area (721 arcmin^2 for Chapman et al. (2005) and 556 arcmin^2 for Banerji et al. (2011)) (Chapman, priv. comm.).

The sample from Simpson et al. (2014) is from an ALMA 870 μm follow up of the 870 μm LABOCA ALESS catalog (Hodge et al. 2013, Karim et al. 2013). Sources were identified with multiwavelength counterparts at wavelengths spanning UV through radio. Seventy-seven SMGs (ten with spectroscopic and 67 with photometric redshifts) were used to construct their redshift distribution, resulting in a median redshift of $\bar{z}$=2.3±0.1. The Simpson et al. (2014) redshift distribution is similar to ours. With a KS probability of 0.87, we have no evidence to indicate the two samples are drawn from different underlying populations. Much like our sample, the sources in the final redshift distribution of Simpson et al. (2014) underwent two selection criteria, $S_{870\mu m}$>4.4 mJy with LABOCA and a much fainter flux density cut with ALMA. Their ALMA selection required S/N>3.5 and RMS<0.6 mJy beam^{-1} suggesting a characteristic source flux density limit ~2.1 mJy at 870 μm. Assuming dust emission at z~2.3 and β=1.5, the corresponding flux density at 1.25 mm is a factor of 2.8 lower, implying a limit of 740 μJy, very close to the characteristic flux limit for our ALMA sources. Indeed, the overall flux distributions of our sample and Simpson et al. (2014) shown in Fig. 8 are very similar, especially at the faint end. This suggests that survey flux limits are very important in explaining redshift distributions. Danielson et al. (2017) further investigated an ALESS sample by undertaking a spectroscopic redshift survey using optical and infrared spectrographs on the VLT and Keck telescopes. Their final sample, consisting of 52 sources with spectroscopic redshifts and 37 sources with photometric redshifts, overlaps considerably with the sample from Simpson et al (2014), but the flux distribution of their sample is skewed slightly higher (Fig. 8). They also find a slightly higher median redshift of $\bar{z}$=2.4±0.1, but, comparing to our redshift distribution, still shows no evidence of being drawn from a different underlying population than ours (a KS probability of 0.23).

The sample from Strandet et al. (2016) is a complete flux density limited sample at $S_{1.4\text{mm}}$>16 mJy from the SPT Deep Field; it consists of 39 sources with spectroscopic redshifts identified primarily through ALMA spectral scans. Ambiguous sources with uncertain line identifications were followed up with targeted observations using APEX instruments FLASH, SEPIA, and Z-spec. In 35 sources, multiple line detections provide an unambiguous redshift, while in the remaining four sources a single line is detected and supporting FIR observations provide a rough redshift range and a most-likely line identification. The sources are expected to be strongly lensed due to their high flux density selection bias, so it is not surprising that their redshift distribution has a significantly higher median redshift, $\bar{z}$=3.87. Strandet et al. (2016) attempt to account for the bias introduced by lensing by dividing their redshift distribution by the probability of lensing as a function of redshift, at an assumed lensing magnification of μ ~10. This reduces their median redshift to $\bar{z}$=3.1 and effectively reduces their flux density cut to $S_{1.4\text{mm}}$>1.6 mJy. For a modified black body with dust emissivity β=1.5 at z ~3.1 the corresponding flux density at 1.25 mm is 2.23 mJy. For the 31 sources in our sample above this flux cut we find a very similar observed median redshift of $\bar{z}$=3.25.

The interferometric sample from Miettinen et al. (2015a) is based on a sample of 1.1 mm detected COSMOS SMGs observed with AzTEC on the James Clerk Maxwell Telescope (Scott et al. 2008). The fifteen brightest sources were then followed up with observations using the SMA at 890 μm (Younger et al. 2007, 2009) and the next fifteen with the Plateau de Bure Interferometer at 1.3 mm. Their selection at 1.1 mm, flux limited

to $S_{1.1mm} \geq 3.3$ mJy, is very similar to ours, although their observations at 1.3 mm are less sensitive, reaching an average RMS of 0.2 mJy and establishing a source flux density cut at 1.3 mm of ~0.9 mJy. The redshift distribution of the 1.1 mm selected JCMT/AzTEC SMGs shown in Fig. 7 was revised from Miettinen et al. (2015a, 2017a). Twelve of these JCMT/AzTEC SMGs (AzTEC 1, 2, 4, 5, 6, 8, 9, 11-N, 11-S, 12, 15, and 24b) are common with the present ALMA sample. The photometric redshifts from Miettinen et al. (2015a, 2017a, and references therein) were derived using a similar HyperZ analysis with SMG templates as in the present work. One exception is AzTEC 17a, for which Miettinen et al. (2017a) adopted a photo-z of $2.96^{+0.06}_{-0.06}$ from the COSMOS2015 catalog (Laigle et al. 2016) instead of the lower spec-z of 0.834 used earlier by Miettinen et al. (2015a). Also, the lower redshift limits for some of the JCMT/AzTEC SMGs were derived using the same Carilli-Yun redshift indicator (Carilli & Yun 1999, 2000) as employed in the present study. As described by Miettinen et al. (2017a), the sources AzTEC 24a and 24c were not detected in our ALMA 1.3 mm imaging of AzTEC 24 (=AzTEC/C48 field), and are very likely to be spurious. Hence, these sources were omitted from the redshift distribution plotted in Fig. 7. The final sample size is 37, out of which 25 sources are different from the present ALMA sample. Using the same survival analysis as in Miettinen et al. (2015a) to take the lower z limits (right-censored data) into account, we derived the mean and median redshifts of $\langle z \rangle = 3.29 \pm 0.22$ and $\tilde{z} = 3.10 \pm 0.28$ for the revised redshift distribution of the JCMT/AzTEC SMGs. The quoted uncertainties represent the standard errors of the mean and median. If we cut our sample at a flux density of 0.9 mJy we find a redshift density median of $\tilde{z}=2.48$. While this is lower than the JCMT/AzTEC SMGs, we are unable to determine if the difference is meaningful due to the small sample of sources that are not in common.

Previous works have attempted to model and predict observed redshift distributions based on underlying population distributions and models of galaxy evolution and formation (e.g., Baugh et al. 2005; Lacey et al. 2016; Cowley et al. 2015; Bethermin et al. 2012, 2015). In particular, Béthermin et al. (2015) used their updated phenomenological models of main sequence and starburst galaxy evolution to model SMG number counts and redshift distributions. Their models characterize predicted redshift distributions as a function of flux density limits and selection wavelength, and they generally show good agreement with SMG surveys and bear out the correlation between brighter and longer wavelength-selected samples lying at higher redshifts. In Fig. 9 we show the Béthermin et al. (2015) predicted median redshifts at 1.2 mm as a function of flux limit, along with the results from our sample and from Simpson et al. (2014). Above our characteristic flux limit of 750 μJy, we find a median from our redshift density distribution of 2.49±0.05, consistent with the prediction of $\tilde{z}=2.49$ from Béthermin et al. (2015). We also consider cutting our sample at the brighter flux densities used in Fig. 6, $S_{1.25mm}>1.25$ mJy and $S_{1.25mm}>1.8$ mJy (note that here we are cutting the sample based on a flux density minimum rather than a minimum and maximum as used in Fig. 6). Our median redshifts rise with the increasing flux density limit to 2.7±0.1 and 3.1±0.2, reflecting the consistent rise over this range predicted by Béthermin et al. (2015) and nearly matching the predicted median redshifts of 2.70 and 2.86, respectively. This is a striking confirmation that flux density and wavelength selection are crucial determining factors in redshift distribution. We have also included the redshift predictions from Hayward et al. (2013b) in Fig. 9. Their faint selection at 1.1 mm ($S_{1.1mm}>1.5$ mJy) is consistent with our observations. At greater flux densi-
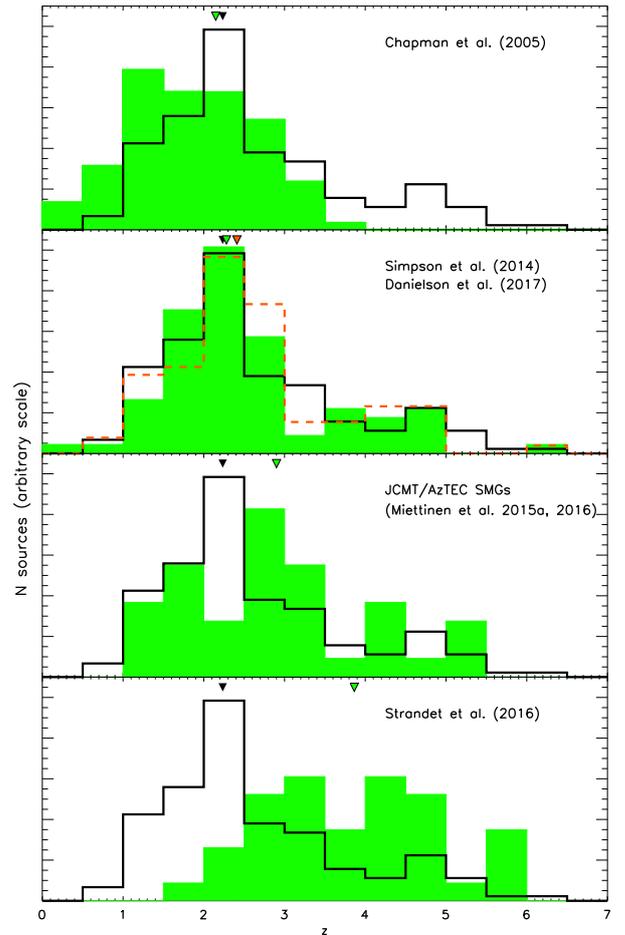
Fig. 7: Redshift distribution of our extended sample (solid black line) compared to previous SMG surveys (green filled histograms). From top to bottom: Chapman et al. (2005) (corrected for redshift desert using SMGs from Banerji et al. (2011)), Simpson et al. (2014) as well as the updated ALESS sample from Danielson et al. (2017) (orange dashed histogram), JCMT/AzTEC SMGs (revised from Miettinen et al. (2015a, 2017a)), Strandet et al. (2016). Histograms have been normalized by their sample size such that each histogram contains equal area. Median values for each distribution are indicated by triangles above the distributions. (Here we use our observed median redshift $\tilde{z}=2.3$ rather than the median calculated from the redshift density likelihood function to compare directly to the other surveys' observed medians.)

ties their prediction differs considerably from Béthermin et al. (2015), however we do not have a sufficient sample at these flux densities to test the respective models. The data from Simpson et al. (2014) follows a similar trend. Their median redshift is 2.31±0.06 for their sample above their characteristic flux limit of ~2.1 mJy. Considering only the brightest 50% of sources in their sample ($S_{870\mu m}>4.4$ mJy), the median redshift rises to 2.5±0.1. These redshift are nearly consistent with although slightly lower than the 850 μm predictions by Béthermin et al. (2015) of 2.5 and 2.7, respectively.
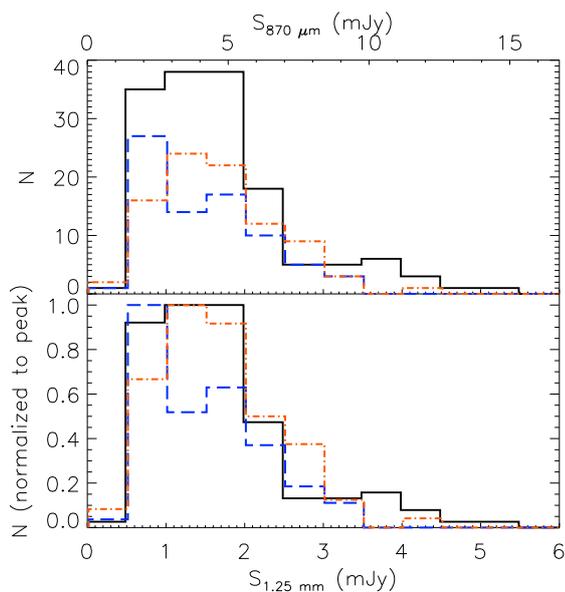
Fig. 8: (Top panel) Flux density distribution for our extended sample (solid black line), the Simpson et al. (2014) ALESS sample (blue dashed line), and the Danielson et al. (2017) ALESS sample (orange dot dashed line). The top x-axis, noting $S_{870\mu m}$ for the ALESS samples, has been scaled from $S_{1.25mm}$ by a factor of 2.8 corresponding to the ratio of continuum emission observed at 870 μm vs. 1.25 mm coming from a modified blackbody with emissivity β=1.5 at $z \sim$2.4. (Bottom panel) Same as the top panel, but the samples have been normalized to their peaks to compare relative sample sizes.

6. Summary

Our ALMA observations provide one of the deepest mm selected SMG surveys with high spatial resolution, $\sim$1". We detect a total of 152 sources within our primary beam at greater than 5σ significance, with an average RMS of 150 μJy beam^{-1}. Although SMGs are typically difficult to cross-identify at other wavelengths, the high resolution of our survey combined with the broad multiwavelength coverage in COSMOS allows us to unambiguously identify counterparts across the UV-NIR, FIR, and radio spectral regimes. This unique data set permits us to compile the spectroscopic redshifts for 30 sources, as well as photometric redshifts for 113 sources through a variety of methods including UV-NIR photometric fits, radio-mm spectral indices, and FIR dust SED fits. For the remaining nine sources, we determine lower redshift limits. While some redshift estimations have large uncertainty, (particularly those redshifts determined through radio-mm spectral indices, FIR dust SED fitting, or ambiguous UV-NIR photometric fits), these do not appear to systematically affect our redshift distribution.

Our sample has a median redshift of $\tilde{z}$=2.48±0.05, generally consistent with previous SMG distributions. Simpson et al. (2014) and Chapman et al. (2005) both find very similar median redshifts. Although recent work by Strandet et al. (2016) finds a significantly higher median redshift of $\tilde{z}$=3.87, this difference is well explained by their very bright flux limit, which largely restricts their sample to highly lensed sources. Deeper investigation into subsets of our sample, split by flux density, bear out the trend toward higher redshifts with increasing flux density limits. In particular, our 1.25 mm data, restricted to various flux limits, show redshift distributions very consistent with the models of Béthermin et al. (2015).
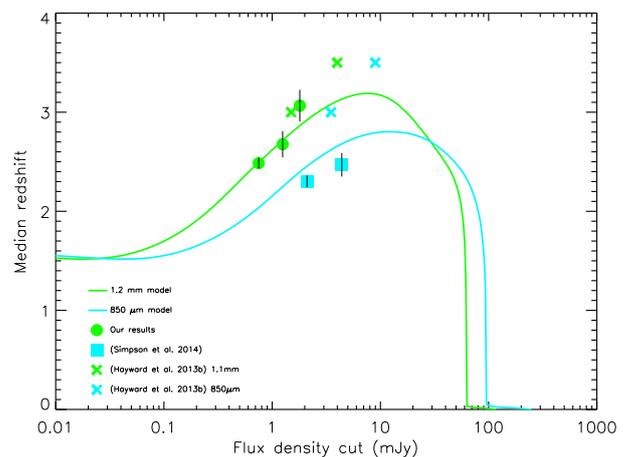
Fig. 9: Green circles denote our survey results which include the extended sample above the characteristic flux limit of 750 μJy, and also cut at $S_{1.25mm}$ >1.25 mJy and $S_{1.25mm}$ >1.8 mJy. Cyan squares denote results from Simpson et al. (2014), including the sample above their characteristic flux limit of 2.1 mJy and also cut at $S_{870\mu m}$ > 4.4 mJy such that half their sample is included. Plotted results and error bars represent the medians calculated through our Monte-Carlo trials and the extent of 68% of the median values. Median redshift as a function of survey flux density limit is also shown. The green and cyan lines give model predictions based on Béthermin et al. 2015. Models from Hayward et al. (2013b), plotted as green (blue) crosses, give mean redshift estimates for 1.1 mm (850 μm) at flux density limits of $S_{1.1mm}$ >1.5 mJy and $S_{1.1mm}$ >4.0 mJy ($S_{850\mu m}$ >3.5 mJy and $S_{850\mu m}$ >9.0 mJy). Our observed redshift distribution rises with increasing flux density limits, consistent with both the models of Béthermin et al. (2015) and Hayward et al. (2013b).

The high resolution of our survey reveals several submm sources to be multi-component systems. A thorough investigation of their physical associations is beyond the scope of this paper, however, based on the redshifts of the components within our multiple systems, we have identified nine likely and 13 possible physical associations of SMGs. An additional eleven systems either have no evidence for physical association (components with unidentified redshifts), or evidence indicating chance alignment (widely discrepant component redshift estimates).

7. Acknowledgements

Table 2: Source list and redshifts.

ALMA ID	Other names	z_{spec}	z_{phot}	$z_{1.4-240GHz}$	$z_{3-240GHz}$	z_{FIR}	z_{synth}	z_{best}	NIR ID	notes
AzTEC/C1a	COSLA89	4.7	$5.82^{+0.38}_{-1.57}$	$4.47^{+2.53}_{-0.76}$	$5.27^{+1.73}_{-0.95}$	–	–	z_{spec}	-1	
AzTEC/C1b	–	–	–	$1.62^{+5.38}_{-0.24}$	$2.50^{+4.50}_{-0.37}$	–	–	$z_{1.4-240GHz}$	-99	
AzTEC/C2a	AzTEC8 COSLA73	3.179	$4.01^{+0.25}_{-0.78}$	$3.58^{+3.42}_{-0.57}$	$2.54^{+2.01}_{-0.38}$	–	–	z_{spec}	842140	
AzTEC/C2b	–	–	$1.06^{+3.95}_{--1.65}$	$3.45^{+3.55}_{-0.54}$	$2.42^{+1.76}_{-0.36}$	2.25 ± 0.74	$1.10^{+2.60}_{--1.20}$	z_{synth}	-1	z_{synth} PDF ambiguous.
AzTEC/C3a	AzTEC2 COSLA4 SCUBA2 450.03 850.00	1.125	–	$2.81^{+0.93}_{-0.90}$	$3.89^{+3.11}_{-0.67}$	–	–	z_{spec}	-99	
AzTEC/C3b	–	–	–	$2.64^{+4.36}_{-0.38}$	$4.03^{+2.97}_{-0.68}$	–	–	$z_{1.4-240GHz}$	-99	
AzTEC/C3c	–	–	–	$2.28^{+4.72}_{-0.34}$	$2.03^{+1.19}_{-0.31}$	–	–	$z_{3-240GHz}$	-99	
AzTEC/C4	AzTEC4	–	$1.91^{+3.52}_{-0.12}$	$3.50^{+3.50}_{-0.55}$	$2.95^{+4.05}_{-0.44}$	5.70 ± 1.16	$5.30^{+0.70}_{-1.10}$	z_{synth}	797542	
AzTEC/C5	AzTEC1 COSLA60	4.341	$4.39^{+0.06}_{-0.63}$	$3.68^{+3.32}_{-0.59}$	$3.22^{+3.78}_{-0.48}$	4.18 ± 0.95	–	z_{spec}	786213	
AzTEC/C6a	Cosbo3	2.490	$2.01^{+0.26}_{-0.71}$	$2.10^{+0.44}_{-0.32}$	$2.10^{+1.28}_{-0.32}$	–	–	z_{spec}	-1	
AzTEC/C6b	–	2.513	$2.10^{+0.89}_{-0.52}$	$1.99^{+5.01}_{-0.30}$	$3.02^{+3.98}_{-0.45}$	–	–	z_{spec}	683281	
AzTEC/C7	Cosbo1 COSLA1 SCUBA2 850.04	–	$3.06^{+1.88}_{-1.76}$	$3.62^{+3.38}_{-0.57}$	$3.70^{+3.30}_{-0.62}$	4.35 ± 0.99	–	z_{phot}	634466	
AzTEC/C8a	–	3.620	$1.82^{+3.13}_{-0.66}$	$2.06^{+4.94}_{-0.31}$	$3.12^{+3.88}_{-0.46}$	–	–	z_{spec}	427059	
AzTEC/C8b	COSLA9S	–	$1.80^{+0.20}_{-0.70}$	$1.73^{+5.27}_{-0.25}$	$1.24^{+0.64}_{-0.21}$	–	$1.80^{+0.20}_{-0.70}$	z_{synth}	428021	z_{synth} PDF ambiguous.
AzTEC/C9a	–	–	$2.68^{+0.24}_{-0.51}$	$3.10^{+3.90}_{-0.46}$	$2.41^{+1.74}_{-0.36}$	–	–	z_{phot}	682558	
AzTEC/C9b	–	2.884	$3.15^{+0.08}_{-0.50}$	$1.30^{+0.18}_{-0.50}$	$1.27^{+0.66}_{-0.20}$	–	–	z_{spec}	681603	
AzTEC/C9c	–	2.922	$3.82^{+0.08}_{-1.05}$	$2.07^{+4.93}_{-0.31}$	$1.54^{+0.83}_{-0.23}$	–	–	z_{spec}	681834	
AzTEC/C10a	–	–	–	$2.73^{+4.27}_{-0.40}$	$3.40^{+3.60}_{-0.59}$	–	–	$z_{3-240GHz}$	-1	
AzTEC/C10b	AzTEC15	–	$2.87^{+1.72}_{-0.92}$	$2.57^{+4.43}_{-0.37}$	$2.26^{+1.52}_{-0.34}$	–	$2.90^{+0.30}_{-0.90}$	z_{synth}	841273	
AzTEC/C10c	–	–	–	$2.22^{+4.78}_{-0.33}$	$3.37^{+3.63}_{-0.53}$	–	–	$z_{1.4-240GHz}$	-99	
AzTEC/C11	–	–	$4.30^{+0.07}_{-3.33}$	$3.54^{+3.46}_{-0.56}$	$2.79^{+4.21}_{-0.42}$	3.76 ± 0.88	–	z_{phot}	505526	
AzTEC/C12	COSLA17N	–	$3.25^{+0.16}_{-0.51}$	$3.11^{+3.89}_{-0.47}$	$2.74^{+2.62}_{-0.41}$	5.79 ± 1.52	–	z_{phot}	582130	
AzTEC/C13a	COSLA54	–	$2.01^{+0.15}_{-0.49}$	$1.93^{+0.38}_{-0.65}$	$1.90^{+1.09}_{-0.29}$	–	–	z_{phot}	616280	
AzTEC/C13b	–	–	$2.01^{+0.30}_{-0.50}$	$2.24^{+4.76}_{-0.34}$	$3.39^{+3.61}_{-0.53}$	–	–	z_{phot}	614777	
AzTEC/C14	AzTEC9 COSLA3 SCUBA2 850.01	–	$4.58^{+0.25}_{-0.68}$	$3.02^{+1.18}_{-0.96}$	$3.18^{+3.82}_{-0.47}$	4.90 ± 1.39	–	z_{phot}	763214	
AzTEC/C15	–	–	$3.91^{+0.28}_{-2.35}$	$3.26^{+3.74}_{-0.49}$	$3.24^{+3.76}_{-0.49}$	–	–	z_{phot}	-1	
AzTEC/C16a	–	–	$3.15^{+0.62}_{-1.54}$	$2.47^{+4.53}_{-0.36}$	$2.32^{+1.60}_{-0.35}$	–	–	z_{phot}	646184	
AzTEC/C16b	–	–	$2.39^{+0.27}_{-0.56}$	$1.69^{+0.30}_{-0.59}$	$1.81^{+1.03}_{-0.27}$	–	–	z_{phot}	645724	
AzTEC/C17	J1000+0234	4.542	$4.58^{+-0.04}_{-0.50}$	$3.21^{+3.79}_{-0.48}$	$3.12^{+3.88}_{-0.46}$	5.19 ± 1.57	–	z_{spec}	842313	
AzTEC/C18	AzTEC12	–	$3.15^{+0.13}_{-0.44}$	$2.34^{+0.55}_{-0.78}$	$2.38^{+1.69}_{-0.35}$	2.66 ± 0.79	–	z_{phot}	942076	
AzTEC/C19	–	–	$2.87^{+0.11}_{-0.41}$	$2.95^{+4.05}_{-0.44}$	$2.13^{+1.32}_{-0.32}$	2.82 ± 1.39	–	z_{phot}	395780	
AzTEC/C20	–	–	$3.06^{+0.13}_{-0.54}$	$2.51^{+4.49}_{-0.37}$	$2.22^{+1.45}_{-0.33}$	2.90 ± 0.85	–	z_{phot}	759562	
AzTEC/C21	–	–	$2.68^{+3.37}_{-0.30}$	$2.82^{+4.18}_{-0.41}$	$2.37^{+1.67}_{-0.35}$	3.36 ± 0.97	$2.70^{+1.30}_{-0.40}$	z_{synth}	-1	
AzTEC/C22a	AzTEC11S	1.598	$2.01^{+0.15}_{-0.45}$	$1.17^{+0.16}_{-0.47}$	$1.47^{+0.79}_{-0.22}$	–	–	z_{spec}	902320	
AzTEC/C22b	AzTEC11N	1.598	–	$0.68^{+0.08}_{-0.36}$	$1.11^{+0.57}_{-0.18}$	–	–	z_{spec}	-1	
AzTEC/C23	–	–	$2.10^{+0.46}_{-0.41}$	$1.34^{+0.19}_{-0.50}$	$1.31^{+0.68}_{-0.21}$	2.17 ± 0.71	–	z_{phot}	-1	
AzTEC/C24a	SCUBA 2 450.38 850.14	–	$2.01^{+0.18}_{-0.46}$	$1.61^{+0.27}_{-0.57}$	$1.78^{+1.00}_{-0.27}$	–	–	z_{phot}	709365	
AzTEC/C24b	–	–	$2.10^{+0.08}_{-0.63}$	$0.83^{+0.10}_{-0.39}$	$0.96^{+0.50}_{-0.17}$	–	–	z_{phot}	709850	
AzTEC/C25	–	2.510	$2.30^{+0.08}_{-0.48}$	$1.78^{+0.33}_{-0.61}$	$1.64^{+0.91}_{-0.24}$	2.22 ± 0.81	–	z_{spec}	427827	
AzTEC/C26	–	–	$5.06^{+0.08}_{-0.90}$	$2.69^{+4.31}_{-0.39}$	$2.88^{+4.12}_{-0.43}$	3.14 ± 0.87	–	z_{phot}	813955	
AzTEC/C27	–	–	$2.77^{+0.88}_{-0.47}$	$2.80^{+4.20}_{-0.41}$	$2.51^{+1.94}_{-0.37}$	4.10 ± 1.15	–	z_{phot}	534452	
AzTEC/C28a	–	2.319	$2.20^{+0.14}_{-0.49}$	$0.92^{+0.11}_{-0.41}$	$1.17^{+0.60}_{-0.19}$	–	–	z_{spec}	604304	
AzTEC/C28b	–	–	$2.30^{+0.31}_{-0.48}$	$1.91^{+5.09}_{-0.28}$	$2.92^{+4.08}_{-0.44}$	–	–	z_{phot}	602117	
AzTEC/C29	–	–	$1.82^{+0.35}_{-0.54}$	$1.35^{+0.20}_{-0.51}$	$1.47^{+0.78}_{-0.22}$	3.36 ± 1.27	–	z_{phot}	473780	
AzTEC/C30a	AzTEC51 SCUBA2 850.15	–	–	$2.20^{+4.80}_{-0.33}$	$2.01^{+1.17}_{-0.31}$	–	–	$z_{3-240GHz}$	-99	
AzTEC/C30b	–	–	–	$1.86^{+5.14}_{-0.27}$	$2.85^{+4.15}_{-0.43}$	–	–	$z_{1.4-240GHz}$	-99	
AzTEC/C31a	–	–	$6.10^{+0.21}_{-3.60}$	$2.30^{+4.70}_{-0.34}$	$2.50^{+1.93}_{-0.37}$	–	$2.10^{+3.20}_{-0.10}$	z_{synth}	-1	z_{synth} PDF ambiguous.
AzTEC/C31b	–	–	$2.49^{+2.79}_{-0.51}$	$2.03^{+4.97}_{-0.31}$	$3.08^{+3.92}_{-0.46}$	–	–	z_{phot}	-1	z_{phot} PDF ambiguous.
AzTEC/C32	Cosbo33	–	$1.63^{+0.20}_{-0.47}$	$2.27^{+0.52}_{-0.76}$	$1.96^{+1.13}_{-0.30}$	2.26 ± 0.85	–	z_{phot}	-1	
AzTEC/C33a	AzTEC35 COSLA50 SCUBA2 850.22	–	$2.30^{+0.16}_{-0.46}$	$1.86^{+0.36}_{-0.63}$	$1.69^{+0.95}_{-0.25}$	0.99 ± 0.66	–	z_{phot}	810228	
AzTEC/C33b	–	–	–	$2.25^{+4.75}_{-0.34}$	$2.38^{+1.68}_{-0.35}$	–	–	$z_{3-240GHz}$	-99	

Table 2: continued.

ALMA ID	Other names	z_{spec}	z_{phot}	$z_{1.4-240GHz}$	$z_{3-240GHz}$	z_{FIR}	z_{synth}	z_{best}	NIR ID	notes
AzTEC/C34a	COSLA19 Cosbo4	–	$3.53^{+0.02}_{-0.52}$	$2.62^{+4.38}_{-0.38}$	$4.00^{+3.00}_{-0.68}$	3.48 ± 2.24	–	z_{phot}	589074	
AzTEC/C34b	–	–	$2.49^{+0.26}_{-0.50}$	$2.55^{+4.45}_{-0.37}$	$3.89^{+3.11}_{-0.67}$	–	–	z_{phot}	590368	
AzTEC/C35	SCUBA2 850.50	–	$3.91^{+0.18}_{-0.50}$	$1.96^{+0.39}_{-0.66}$	$2.07^{+1.24}_{-0.31}$	4.58 ± 0.99	–	z_{phot}	686297	
AzTEC/C36	–	2.415	$2.68^{+0.10}_{-0.55}$	$1.78^{+0.33}_{-0.61}$	$1.91^{+1.10}_{-0.29}$	2.65 ± 0.75	–	z_{spec}	518177	
AzTEC/C37	–	–	$1.63^{+1.29}_{-0.42}$	$2.96^{+1.09}_{-0.94}$	$2.56^{+2.07}_{-0.38}$	5.04 ± 3.82	$1.70^{+0.70}_{-0.30}$	z_{synth}	-1	
AzTEC/C38	COSLA35 SCUBA2 450.05 850.08	–	$1.91^{+0.53}_{-0.46}$	$2.82^{+4.18}_{-0.41}$	$3.10^{+3.90}_{-0.46}$	2.22 ± 0.85	–	z_{phot}	702910	
AzTEC/C39	–	–	$1.72^{+4.61}_{--0.00}$	$2.54^{+4.46}_{-0.37}$	$1.83^{+1.04}_{-0.28}$	1.95 ± 0.78	$2.00^{+0.20}_{-0.40}$	z_{synth}	462117	
AzTEC/C40	–	–	–	$2.07^{+0.43}_{-0.70}$	$2.27^{+1.52}_{-0.34}$	5.25 ± 1.11	–	z_{FIR}	-99	
AzTEC/C41	–	–	$1.25^{+0.18}_{-0.34}$	$2.63^{+4.37}_{-0.38}$	$2.33^{+1.60}_{-0.35}$	3.14 ± 1.12	–	z_{phot}	700004	
AzTEC/C42	AzTEC5 SCUBA2 450.04 850.03	–	$3.63^{+0.37}_{-0.56}$	$1.77^{+0.33}_{-0.61}$	$1.62^{+0.89}_{-0.24}$	2.01 ± 0.76	–	z_{phot}	815840	
AzTEC/C43a	–	–	$2.01^{+0.23}_{-0.47}$	$2.05^{+4.95}_{-0.31}$	$1.58^{+0.86}_{-0.24}$	–	–	z_{phot}	-1	
AzTEC/C43b	–	–	$1.82^{+0.29}_{-0.36}$	$1.78^{+5.22}_{-0.26}$	$1.75^{+0.99}_{-0.26}$	–	–	z_{phot}	484892	
AzTEC/C44a	–	–	$2.01^{+0.29}_{-0.44}$	$2.33^{+4.67}_{-0.35}$	$1.90^{+1.09}_{-0.29}$	–	–	z_{phot}	346234	
AzTEC/C44b	–	1.192	$0.96^{+0.14}_{-0.36}$	$2.09^{+4.91}_{-0.32}$	$2.01^{+1.17}_{-0.31}$	–	–	z_{spec}	350733	$z_{Marchesi}$=2.2
AzTEC/C45	SCUBA2 850.57	2.330	$1.91^{+0.34}_{-0.40}$	$1.63^{+5.37}_{-0.24}$	$1.43^{+0.76}_{-0.22}$	4.54 ± 1.02	–	z_{spec}	826154	$z_{Marchesi}$=2.1
AzTEC/C46	–	–	$1.06^{+1.07}_{-0.41}$	$1.55^{+0.25}_{-0.56}$	$1.66^{+0.92}_{-0.25}$	2.97 ± 0.88	–	z_{phot}	849028	
AzTEC/C47	–	2.047	$1.91^{+0.32}_{-0.38}$	$0.79^{+0.10}_{-0.38}$	$1.05^{+0.55}_{-0.18}$	1.42 ± 0.80	–	z_{spec}	475050	
AzTEC/C48a	AzTEC24b	–	$1.91^{+0.18}_{-0.42}$	$2.36^{+4.64}_{-0.35}$	$1.83^{+1.04}_{-0.28}$	–	–	z_{phot}	887050	
AzTEC/C48b	–	–	$1.82^{+0.21}_{-0.46}$	$1.62^{+5.38}_{-0.24}$	$2.51^{+4.49}_{-0.37}$	–	–	z_{phot}	887401	
AzTEC/C49	–	–	$0.87^{+0.23}_{-0.33}$	$2.70^{+4.30}_{-0.39}$	$4.13^{+2.87}_{-0.70}$	4.76 ± 1.03	–	z_{phot}	-1	
AzTEC/C50	–	–	$3.15^{+0.78}_{-1.32}$	$2.22^{+0.50}_{-0.74}$	$2.43^{+1.78}_{-0.36}$	2.49 ± 1.23	–	z_{phot}	552644	
AzTEC/C51a	–	–	–	$2.33^{+4.67}_{-0.35}$	$3.54^{+3.46}_{-0.57}$	–	–	$z_{1.4-240GHz}$	-1	
AzTEC/C51b	–	–	$1.34^{+0.20}_{-0.34}$	$1.65^{+5.35}_{-0.24}$	$2.54^{+4.46}_{-0.38}$	–	–	z_{phot}	456882	
AzTEC/C52	–	1.148	$1.34^{+0.12}_{-0.38}$	$1.34^{+0.19}_{-0.51}$	$1.40^{+0.74}_{-0.22}$	1.07 ± 0.64	–	z_{spec}	694031	
AzTEC/C53	–	–	$1.63^{+4.53}_{-0.48}$	$1.65^{+5.35}_{-0.24}$	$1.82^{+1.03}_{-0.31}$	3.20 ± 0.92	$2.20^{+0.60}_{-0.70}$	z_{synth}	593993	
AzTEC/C54	–	–	$3.25^{+0.04}_{-0.52}$	$2.78^{+4.22}_{-0.41}$	$2.39^{+1.71}_{-0.36}$	4.65 ± 0.96	–	z_{phot}	439437	
AzTEC/C55a	–	–	$2.49^{+0.33}_{-0.45}$	$2.56^{+4.44}_{-0.37}$	$2.16^{+1.37}_{-0.32}$	–	–	z_{phot}	413145	
AzTEC/C55b	–	–	$2.77^{+0.32}_{-0.41}$	$1.69^{+0.31}_{-0.59}$	$1.91^{+1.10}_{-0.29}$	–	–	z_{phot}	412615	
AzTEC/C55c	–	–	–	$1.70^{+5.30}_{-0.25}$	$2.63^{+4.37}_{-0.40}$	–	–	$z_{1.4-240GHz}$	-99	
AzTEC/C56	–	–	$3.82^{+0.11}_{-0.54}$	$3.30^{+3.70}_{-0.50}$	$2.56^{+2.06}_{-0.38}$	2.42 ± 0.85	–	$z_{Marchesi}$	703515	$z_{Marchesi}$=3.4
AzTEC/C57	–	–	–	$1.52^{+5.48}_{-0.23}$	$2.36^{+4.64}_{-0.35}$	–	–	$z_{1.4-240GHz}$	-99	
AzTEC/C58	–	–	$4.10^{+0.32}_{-0.79}$	$2.87^{+4.13}_{-0.42}$	$2.35^{+1.63}_{-0.35}$	4.35 ± 2.27	–	z_{phot}	304628	
AzTEC/C59	–	1.280	$1.34^{+0.18}_{-0.34}$	$1.11^{+0.15}_{-0.45}$	$1.28^{+0.67}_{-0.20}$	1.18 ± 0.63	–	z_{spec}	872523	
AzTEC/C60a	–	–	$0.96^{+0.14}_{-0.40}$	$2.11^{+4.89}_{-0.32}$	$1.85^{+1.05}_{-0.28}$	–	–	z_{phot}	-1	
AzTEC/C60b	–	–	$4.77^{+0.14}_{-0.75}$	$1.70^{+5.30}_{-0.25}$	$2.63^{+4.37}_{-0.39}$	–	–	z_{phot}	697712	
AzTEC/C61	–	3.267	$7.00^{+0.00}_{-5.14}$	–	–	3.57 ± 0.97	$2.60^{+1.60}_{-0.20}$	z_{spec}	842703	
AzTEC/C62	–	–	–	$1.86^{+5.14}_{-0.27}$	$1.55^{+0.84}_{-0.24}$	3.36 ± 0.97	–	z_{FIR}	-1	
AzTEC/C63	–	–	–	$2.90^{+4.10}_{-0.43}$	$4.45^{+2.55}_{-0.77}$	4.90 ± 3.21	–	z_{FIR}	-99	
AzTEC/C64	–	–	$2.58^{+0.79}_{-0.63}$	$2.80^{+4.20}_{-0.41}$	$2.15^{+1.36}_{-0.32}$	2.35 ± 0.87	–	z_{phot}	-1	
AzTEC/C65	SCUBA2 450.27 850.115	1.798	$1.72^{+0.18}_{-0.36}$	$1.25^{+0.17}_{-0.49}$	$1.30^{+0.68}_{-0.21}$	1.95 ± 0.69	–	z_{spec}	702734	
AzTEC/C66	SCUBA2 450.66 850.146	–	$2.01^{+0.27}_{-0.50}$	$1.50^{+0.23}_{-0.54}$	$1.44^{+0.76}_{-0.22}$	1.51 ± 0.70	–	z_{phot}	-1	
AzTEC/C67	–	2.934	$3.06^{+0.09}_{-0.42}$	$1.91^{+0.38}_{-0.65}$	$2.01^{+1.17}_{-0.31}$	2.07 ± 0.84	–	z_{spec}	567572	
AzTEC/C69	–	–	$3.91^{+0.09}_{-0.50}$	$1.70^{+5.30}_{-0.25}$	$2.63^{+4.37}_{-0.40}$	–	–	z_{phot}	560381	
AzTEC/C70	–	–	$4.01^{+0.09}_{-0.66}$	$2.49^{+4.51}_{-0.36}$	$2.42^{+1.76}_{-0.36}$	2.27 ± 0.87	–	z_{phot}	494956	
AzTEC/C71a	–	–	–	$2.65^{+4.35}_{-0.39}$	$4.06^{+2.94}_{-0.69}$	2.42 ± 1.30	–	z_{FIR}	-99	
AzTEC/C71b	Cosbo36 SCUBA2 850.63	0.829	–	$1.46^{+0.22}_{-0.53}$	$1.65^{+0.92}_{-0.24}$	–	–	z_{spec}	-99	$z_{Marchesi}$=0.9
AzTEC/C72	–	–	$1.72^{+0.38}_{-0.45}$	$1.83^{+0.35}_{-0.63}$	$1.88^{+1.08}_{-0.29}$	2.29 ± 0.84	–	z_{phot}	515355	
AzTEC/C73	–	–	$1.72^{+4.74}_{-0.17}$	$2.07^{+4.93}_{-0.32}$	$3.13^{+3.87}_{-0.46}$	5.48 ± 1.21	$6.40^{+0.60}_{-1.10}$	z_{synth}	-1	z_{synth} PDF ambiguous.
AzTEC/C74a	SCUBA2 850.35	–	$2.10^{+0.20}_{-0.67}$	$2.53^{+4.47}_{-0.37}$	$2.58^{+2.12}_{-0.39}$	–	–	z_{phot}	701870	
AzTEC/C74b	–	–	–	$1.93^{+5.07}_{-0.29}$	$2.94^{+4.06}_{-0.44}$	–	–	$z_{1.4-240GHz}$	-99	
AzTEC/C76	–	–	$4.01^{+0.07}_{-0.57}$	$2.52^{+4.48}_{-0.37}$	$2.08^{+1.26}_{-0.32}$	5.13 ± 1.06	–	z_{phot}	593906	

Table 2: continued.

ALMA ID	Other names	z_{spec}	z_{phot}	$z_{1.4-240GHz}$	$z_{3-240GHz}$	z_{FIR}	z_{synth}	z_{best}	NIR ID	notes
AzTEC/C77a	–	–	$3.53^{+0.58}_{-1.29}$	$0.64^{+0.07}_{-0.35}$	$0.69^{+0.41}_{-0.14}$	–	–	z_{phot}	441615	
AzTEC/C77b	–	–	$3.06^{+0.58}_{-1.19}$	$1.69^{+0.30}_{-0.59}$	$1.96^{+1.14}_{-0.30}$	–	–	z_{phot}	-1	
AzTEC/C78	–	–	$4.77^{+0.09}_{-3.89}$	$2.61^{+4.39}_{-0.38}$	$3.99^{+3.01}_{-0.68}$	–	–	z_{phot}	457720	z_{phot} PDF ambiguous.
AzTEC/C79	–	–	$2.20^{+0.33}_{-0.96}$	$2.58^{+4.42}_{-0.38}$	$2.21^{+1.43}_{-0.33}$	2.82 ± 1.97	–	z_{phot}	610723	
AzTEC/C80a	COSLA47 SCUBA2 450.01 850.02	–	$2.10^{+0.66}_{-0.43}$	$2.59^{+4.41}_{-0.38}$	$1.97^{+1.15}_{-0.30}$	–	–	z_{phot}	747545	
AzTEC/C80b	–	–	$2.01^{+0.68}_{-0.52}$	$2.01^{+4.99}_{-0.30}$	$3.05^{+3.95}_{-0.46}$	–	–	z_{phot}	746328	
AzTEC/C81	–	–	–	$2.15^{+4.85}_{-0.32}$	$2.02^{+1.18}_{-0.31}$	4.62 ± 1.48	–	z_{FIR}	-1	
AzTEC/C84a	–	–	$1.63^{+2.73}_{-0.34}$	$2.86^{+4.14}_{-0.42}$	$4.38^{+2.62}_{-0.75}$	–	–	z_{phot}	414489	z_{phot} PDF ambiguous.
AzTEC/C84b	–	1.959	$2.20^{+0.05}_{-0.63}$	$1.92^{+0.38}_{-0.65}$	$1.85^{+1.05}_{-0.28}$	2.60 ± 0.91	–	z_{spec}	410945	
AzTEC/C86	–	–	$0.77^{+0.15}_{-0.31}$	$2.29^{+4.71}_{-0.34}$	$2.08^{+1.26}_{-0.32}$	3.14 ± 1.60	–	$z_{Marchesi}$	652663	$z_{Marchesi}=1.7$
AzTEC/C87	–	–	$2.39^{+0.20}_{-0.45}$	$2.41^{+4.59}_{-0.35}$	$1.79^{+1.01}_{-0.27}$	3.31 ± 0.82	–	z_{phot}	-1	
AzTEC/C88	–	–	$1.82^{+0.38}_{-0.47}$	$1.73^{+5.27}_{-0.25}$	$1.37^{+0.72}_{-0.21}$	3.25 ± 1.15	–	z_{phot}	-1	
AzTEC/C90a	–	–	$2.20^{+2.83}_{-0.46}$	$1.94^{+5.06}_{-0.29}$	$2.96^{+4.04}_{-0.44}$	–	–	z_{phot}	-1	
AzTEC/C90b	–	–	$2.77^{+0.33}_{-1.67}$	$1.91^{+5.09}_{-0.28}$	$2.92^{+4.08}_{-0.44}$	–	–	z_{phot}	-1	z_{phot} PDF ambiguous.
AzTEC/C90c	–	–	$2.20^{+0.23}_{-0.42}$	$1.81^{+5.19}_{-0.26}$	$1.56^{+0.84}_{-0.23}$	–	–	z_{phot}	645708	
AzTEC/C91	–	–	$1.63^{+0.29}_{-0.41}$	$2.20^{+4.80}_{-0.33}$	$1.70^{+0.95}_{-0.25}$	2.09 ± 0.75	–	z_{phot}	722424	
AzTEC/C92a	–	–	$2.58^{+2.67}_{-0.46}$	$2.89^{+4.11}_{-0.43}$	$3.14^{+3.86}_{-0.47}$	–	–	z_{phot}	-1	
AzTEC/C92b	–	–	$4.87^{+0.22}_{-0.98}$	$2.36^{+4.64}_{-0.35}$	$2.13^{+1.33}_{-0.32}$	–	–	z_{phot}	793275	
AzTEC/C93	–	–	$1.63^{+1.10}_{-0.53}$	$2.17^{+0.47}_{-0.73}$	$2.04^{+1.20}_{-0.31}$	2.32 ± 0.95	–	z_{phot}	587450	
AzTEC/C95	–	2.102	$1.63^{+0.44}_{-0.43}$	$2.13^{+4.87}_{-0.32}$	$1.60^{+0.87}_{-0.24}$	1.94 ± 0.78	–	z_{spec}	600465	
AzTEC/C97a	–	–	$3.06^{+0.04}_{-0.52}$	$1.70^{+0.31}_{-0.59}$	$3.96^{+3.04}_{-0.68}$	–	–	z_{phot}	679317	
AzTEC/C97b	–	–	$2.01^{+0.08}_{-0.48}$	$1.79^{+5.21}_{-0.26}$	$1.64^{+0.91}_{-0.24}$	0.80 ± 0.73	–	z_{phot}	678384	
AzTEC/C98	COSLA18	–	$1.82^{+0.60}_{-0.46}$	$2.01^{+0.41}_{-0.68}$	$2.05^{+1.22}_{-0.31}$	1.91 ± 0.71	–	z_{phot}	518250	
AzTEC/C99	–	–	$2.68^{+1.37}_{-0.97}$	$2.31^{+4.69}_{-0.34}$	$2.20^{+1.43}_{-0.33}$	–	–	z_{phot}	-1	
AzTEC/C100a	–	–	$1.63^{+0.17}_{-0.33}$	$1.82^{+0.35}_{-0.62}$	$3.53^{+3.47}_{-0.57}$	1.93 ± 1.22	–	z_{phot}	575024	
AzTEC/C100b	–	–	$2.68^{+0.44}_{-0.63}$	$1.92^{+5.08}_{-0.28}$	$2.93^{+4.07}_{-0.44}$	–	–	z_{phot}	576755	
AzTEC/C101a	–	–	$1.53^{+0.31}_{-0.51}$	$2.35^{+4.65}_{-0.35}$	$2.14^{+1.34}_{-0.32}$	–	–	z_{phot}	-1	
AzTEC/C101b	–	–	–	$1.87^{+5.13}_{-0.27}$	$1.74^{+0.98}_{-0.27}$	–	–	$z_{3-240GHz}$	794601	
AzTEC/C103	–	–	$2.10^{+0.33}_{-0.57}$	$2.55^{+4.45}_{-0.37}$	$2.14^{+1.35}_{-0.32}$	4.55 ± 1.00	–	z_{phot}	423273	
AzTEC/C105	–	–	$2.20^{+0.08}_{-0.54}$	$2.63^{+4.37}_{-0.38}$	$2.00^{+1.17}_{-0.31}$	3.27 ± 0.85	–	z_{phot}	623091	
AzTEC/C106	AzTEC6	–	–	$3.43^{+3.57}_{-0.53}$	$3.30^{+3.70}_{-0.50}$	5.63 ± 2.77	–	z_{FIR}	-99	
AzTEC/C107	–	–	$5.15^{+0.93}_{-1.40}$	$2.53^{+4.47}_{-0.37}$	$2.60^{+2.16}_{-0.39}$	4.76 ± 1.90	–	z_{phot}	-1	
AzTEC/C108	–	–	$2.30^{+1.26}_{-0.47}$	$2.90^{+4.10}_{-0.43}$	$4.44^{+2.56}_{-0.76}$	3.97 ± 1.14	–	z_{phot}	-1	
AzTEC/C109	–	–	$2.20^{+0.28}_{-0.41}$	$2.28^{+0.52}_{-0.76}$	$2.78^{+4.22}_{-0.42}$	2.17 ± 0.77	–	z_{phot}	776550	
AzTEC/C111	–	–	$2.10^{+0.54}_{-0.59}$	$1.88^{+0.36}_{-0.64}$	$1.91^{+1.10}_{-0.29}$	1.80 ± 0.85	–	z_{phot}	599375	
AzTEC/C112	–	1.894	$1.82^{+0.21}_{-0.37}$	$1.55^{+0.25}_{-0.56}$	$1.56^{+0.85}_{-0.23}$	2.29 ± 0.94	–	z_{spec}	394010	
AzTEC/C113	–	2.090	$2.10^{+0.09}_{-0.47}$	$1.10^{+0.14}_{-0.45}$	$1.03^{+0.54}_{-0.17}$	0.07 ± 0.55	–	z_{spec}	791065	
AzTEC/C114	SCUBA2 850.13	–	–	$2.85^{+4.15}_{-0.42}$	$1.92^{+1.11}_{-0.29}$	5.33 ± 3.22	–	z_{FIR}	-99	
AzTEC/C115	–	–	$2.77^{+3.00}_{-0.51}$	$2.48^{+4.52}_{-0.36}$	$2.48^{+1.89}_{-0.37}$	–	$2.80^{+1.30}_{-0.60}$	z_{synth}	-1	
AzTEC/C116	Cosbo27	–	$2.20^{+1.75}_{-0.43}$	$1.68^{+0.30}_{-0.59}$	$1.62^{+0.88}_{-0.24}$	1.46 ± 0.75	–	z_{phot}	501111	
AzTEC/C117	COSLA40	–	$1.72^{+0.20}_{-0.68}$	$2.01^{+4.99}_{-0.31}$	$3.06^{+3.94}_{-0.46}$	4.73 ± 0.99	–	z_{phot}	685079	
AzTEC/C118	Cosbo8	2.234	–	$2.01^{+0.41}_{-0.68}$	$2.14^{+1.34}_{-0.32}$	2.77 ± 0.99	–	z_{spec}	-1	$z_{Marchesi}=0.8$
AzTEC/C119	–	–	$3.25^{+0.82}_{-0.62}$	$2.98^{+4.02}_{-0.45}$	$2.76^{+4.27}_{-0.41}$	3.36 ± 1.17	–	z_{phot}	-1	
AzTEC/C122a	–	–	$1.06^{+0.12}_{-0.40}$	$2.26^{+4.74}_{-0.34}$	$2.47^{+1.86}_{-0.37}$	–	–	z_{phot}	644904	
AzTEC/C122b	–	–	–	$1.95^{+5.05}_{-0.29}$	$2.98^{+4.02}_{-0.45}$	–	–	$z_{1.4-240GHz}$	-1	
AzTEC/C123	–	–	$1.82^{+0.20}_{-0.61}$	$2.49^{+4.51}_{-0.36}$	$1.97^{+1.14}_{-0.30}$	1.58 ± 0.76	–	z_{phot}	375061	
AzTEC/C124	AzTEC34	1.880	$1.63^{+0.21}_{-0.38}$	$1.82^{+5.18}_{-0.26}$	$2.80^{+4.20}_{-0.42}$	1.48 ± 0.76	–	z_{spec}	854544	
AzTEC/C126	–	–	$4.68^{+0.31}_{-0.64}$	$2.51^{+4.49}_{-0.37}$	$3.83^{+3.17}_{-0.65}$	0.49 ± 0.79	–	z_{phot}	-1	
AzTEC/C127	–	–	$2.01^{+0.17}_{-0.51}$	$1.15^{+0.15}_{-0.47}$	$1.23^{+0.64}_{-0.20}$	0.72 ± 0.62	–	z_{phot}	851363	
AzTEC/C129	–	–	$4.87^{+0.73}_{-0.97}$	$3.02^{+3.98}_{-0.45}$	$4.64^{+2.36}_{-0.81}$	–	–	z_{phot}	-1	

References

Aihara, H., Allende Prieto, C., An, D., et al. 2011, ApJS, 193, 29
Aravena, M., Younger, J. D., Fazio, G. G., et al. 2010, ApJ, 719, L15
Aretxaga, I., Wilson, G. W., Aguilar, E., et al. 2011, MNRAS, 415, 3831
Asboth, V., Conley, A., Sayers, J., et al. 2016, MNRAS, 462, 1989
Banerji, M., Chapman, S. C., Smail, I., et al. 2011, MNRAS, 418, 1071
Barger, A. J., Cowie, L. L., Sanders, D. B., et al. 1998, Nature, 394, 248
Barger, A. J., Wang, W.-H., Cowie, L. L., et al. 2012, ApJ, 761, 89
Baugh, C. M., Lacey, C. G., Frenk, C. S., et al. 2005, MNRAS, 356, 1191
Bertoldi, F., Carilli, C., Aravena, M., et al. 2007, ApJS, 172, 132
Béthermin, M., Daddi, E., Magdis, G., et al. 2012, ApJ, 757, L23
Béthermin, M., De Breuck, C., Sargent, M., & Daddi, E. 2015, A&A, 576, L9
Biggs, A. D., Ivison, R. J., Ibar, E., et al. 2011, MNRAS, 413, 2314
Blain, A. W., Smail, I., Ivison, R. J., Kneib, J.-P., & Frayer, D. T. 2002, Phys. Rep., 369, 111
Bolzonella, M., Miralles, J.-M., & Pelló, R. 2000, A&A, 363, 476
Bussmann, R. S., Riechers, D., Fialkov, A., et al. 2015, ApJ, 812, 43
Calzetti, D., Armus, L., Bohlin, R. C., et al. 2000, ApJ, 533, 682
Capak, P., Aussel, H., Ajiki, M., et al. 2007, ApJS, 172, 99
Capak, P., Carilli, C. L., Lee, N., et al. 2008, ApJ, 681, L53
Capak, P., Mobasher, B., Scoville, N. Z., et al. 2011, ApJ, 730, 68
Carilli, C. L. & Yun, M. S. 1999, ApJ, 513, L13
Carilli, C. L. & Yun, M. S. 2000, ApJ, 539, 1024
Casey, C. M., Chen, C.-C., Cowie, L. L., et al. 2013, MNRAS, 436, 1919
Casey, C. M., Cooray, A., Capak, P., et al. 2015, ApJ, 808, L33
Casey, C. M., Narayanan, D., & Cooray, A. 2014, Phys. Rep., 541, 45
Chapman, S. C., Blain, A. W., Smail, I., & Ivison, R. J. 2005, ApJ, 622, 772
Chen, C.-C., Smail, I., Swinbank, A. M., et al. 2016, ApJ, 831, 91
Civano, F., Elvis, M., Brusa, M., et al. 2012, ApJS, 201, 30
Civano, F., Marchesi, S., Comastri, A., et al. 2016, ApJ, 819, 62
Combes, F., Rex, M., Rawle, T. D., et al. 2012, A&A, 538, L4
Coppin, K., Chapin, E. L., Mortier, A. M. J., et al. 2006, MNRAS, 372, 1621
Coppin, K. E. K., Smail, I., Alexander, D. M., et al. 2009, MNRAS, 395, 1905
Cowley, W. I., Lacey, C. G., Baugh, C. M., & Cole, S. 2015, MNRAS, 446, 1784
Cox, P., Krips, M., Neri, R., et al. 2011, ApJ, 740, 63
Daddi, E., Dannerbauer, H., Krips, M., et al. 2009a, ApJ, 695, L176
Daddi, E., Dannerbauer, H., Stern, D., et al. 2009b, ApJ, 694, 1517
Danielson, A. L. R., Swinbank, A. M., Smail, I., et al. 2017, ApJ, 840, 78
Dowell, C. D., Conley, A., Glenn, J., et al. 2014, ApJ, 780, 75
Downes, D., Neri, R., Greve, A., et al. 1999, A&A, 347, 809
Dwek, E., Staguhn, J. G., Arendt, R. G., et al. 2011, ApJ, 738, 36
Elvis, M., Civano, F., Vignali, C., et al. 2009, ApJS, 184, 158
Ferrara, A., Viti, S., & Ceccarelli, C. 2016, MNRAS, 463, L112
Greve, T. R., Pope, A., Scott, D., et al. 2008, MNRAS, 389, 1489
Harris, A. I., Baker, A. J., Frayer, D. T., et al. 2012, ApJ, 752, 152
Hayward, C. C., Behroozi, P. S., Somerville, R. S., et al. 2013a, MNRAS, 434, 2572
Hayward, C. C., Kereš, D., Jonsson, P., et al. 2011, ApJ, 743, 159
Hayward, C. C., Narayanan, D., Kereš, D., et al. 2013b, MNRAS, 428, 2529
Helou, G., Soifer, B. T., & Rowan-Robinson, M. 1985, ApJ, 298, L7
Hodge, J. A., Karim, A., Smail, I., et al. 2013, ApJ, 768, 91
Hodge, J. A., Riechers, D., Decarli, R., et al. 2015, ApJ, 798, L18
Hodge, J. A., Swinbank, A. M., Simpson, J. M., et al. 2016, ApJ, 833, 103
Hogg, D. W. & Turner, E. L. 1998, PASP, 110, 727
Hughes, D. H., Serjeant, S., Dunlop, J., et al. 1998, Nature, 394, 241
Iglesias-Páramo, J., Buat, V., Hernández-Fernández, J., et al. 2007, ApJ, 670, 279
Ilbert, O., Capak, P., Salvato, M., et al. 2009, ApJ, 690, 1236
Ilbert, O., McCracken, H. J., Le Fevre, O., et al. 2013, VizieR Online Data Catalog, 355
Iono, D., Peck, A. B., Pope, A., et al. 2006, ApJ, 640, L1
Ivison, R. J., Greve, T. R., Dunlop, J. S., et al. 2007, MNRAS, 380, 199
Ivison, R. J., Greve, T. R., Smail, I., et al. 2002, MNRAS, 337, 1
Ivison, R. J., Swinbank, A. M., Swinyard, B., et al. 2010, A&A, 518, L35
Johansson, D., Horellou, C., Lopez-Cruz, O., et al. 2012, A&A, 543, A62
Karim, A., Swinbank, A. M., Hodge, J. A., et al. 2013, MNRAS, 432, 2
Knudsen, K. K., Kneib, J.-P., Richard, J., Petitpas, G., & Egami, E. 2010, ApJ, 709, 210
Laigle, C., McCracken, H. J., Ilbert, O., et al. 2016, ApJS, 224, 24
Le Fèvre, O., Tasca, L. A. M., Cassata, P., et al. 2015, A&A, 576, A79
Lilly, S. J., Le Brun, V., Maier, C., et al. 2009, ApJS, 184, 218
Lilly, S. J., Le Fèvre, O., Renzini, A., et al. 2007, ApJS, 172, 70
Lutz, D., Poglitsch, A., Altieri, B., et al. 2011, A&A, 532, A90
Magnelli, B., Elbaz, D., Chary, R. R., et al. 2011, A&A, 528, A35
Magnelli, B., Popesso, P., Berta, S., et al. 2013, A&A, 553, A132
Marchesi, S., Civano, F., Elvis, M., et al. 2016, ApJ, 817, 34
McCracken, H. J., Milvang-Jensen, B., Dunlop, J., et al. 2012, A&A, 544, A156
Menéndez-Delmestre, K., Blain, A. W., Smail, I., et al. 2009, ApJ, 699, 667
Michałowski, M. J., Watson, D., & Hjorth, J. 2010, ApJ, 712, 942
Miettinen, O., Delvecchio, I., Smolčić, V., et al. 2017a, A&A, 597, A5

Miettinen, O., Novak, M., Smolčić, V., et al. 2017b, A&A, 602, A54
Miettinen, O., Novak, M., Smolčić, V., et al. 2015a, A&A, 584, A32
Miettinen, O., Smolčić, V., Novak, M., et al. 2015b, A&A, 577, A29
Oliver, S. J., Bock, J., Altieri, B., et al. 2012, MNRAS, 424, 1614
Pope, A., Borys, C., Scott, D., et al. 2005, MNRAS, 358, 149
Pope, A., Bussmann, R. S., Dey, A., et al. 2008, ApJ, 689, 127
Prescott, M. K. M., Impey, C. D., Cool, R. J., & Scoville, N. Z. 2006, ApJ, 644, 100
Puccetti, S., Vignali, C., Cappelluti, N., et al. 2009, ApJS, 185, 586
Riechers, D. A., Bradford, C. M., Clements, D. L., et al. 2013, Nature, 496, 329
Riechers, D. A., Capak, P. L., Carilli, C. L., et al. 2010, ApJ, 720, L131
Riechers, D. A., Carilli, C. L., Capak, P. L., et al. 2014, ApJ, 796, 84
Salvato, M., Hasinger, G., Ilbert, O., et al. 2009, ApJ, 690, 1250
Salvato, M., Ilbert, O., Hasinger, G., et al. 2011, ApJ, 742, 61
Sanders, D. B., Salvato, M., Aussel, H., et al. 2007, ApJS, 172, 86
Schinnerer, E., Carilli, C. L., Capak, P., et al. 2008, ApJ, 689, L5
Schinnerer, E., Smolčić, V., Carilli, C. L., et al. 2007, ApJS, 172, 46
Scott, K. S., Austermann, J. E., Perera, T. A., et al. 2008, MNRAS, 385, 2225
Scott, S. E., Dunlop, J. S., & Serjeant, S. 2006, MNRAS, 370, 1057
Silva, L., Granato, G. L., Bressan, A., & Danese, L. 1998, ApJ, 509, 103
Simpson, J. M., Smail, I., Swinbank, A. M., et al. 2015, ApJ, 799, 81
Simpson, J. M., Swinbank, A. M., Smail, I., et al. 2014, ApJ, 788, 125
Smail, I., Ivison, R. J., & Blain, A. W. 1997, ApJ, 490, L5
Smolčić, V., Aravena, M., Navarrete, F., et al. 2012a, A&A, 548, A4
Smolčić, V., Capak, P., Ilbert, O., et al. 2011, ApJ, 731, L27
Smolčić, V., Karim, A., Miettinen, O., et al. 2015, A&A, 576, A127
Smolčić, V., Navarrete, F., Aravena, M., et al. 2012b, ApJS, 200, 10
Smolčić, V., Novak, M., Bondi, M., et al. 2017, A&A, 602, A1
Strandet, M. L., Weiss, A., Vieira, J. D., et al. 2016, ApJ, 822, 80
Su, T., Marriage, T. A., Asboth, V., et al. 2016, MNRAS[arXiv:1511.06770]
Swinbank, A. M., Smail, I., Longmore, S., et al. 2010, Nature, 464, 733
Tan, Q., Daddi, E., Magdis, G., et al. 2014, A&A, 569, A98
Tasca, L. A. M., Le Fèvre, O., Ribeiro, B., et al. 2017, A&A, 600, A110
Trump, J. R., Impey, C. D., McCarthy, P. J., et al. 2007, ApJS, 172, 383
Vieira, J. D., Marrone, D. P., Chapman, S. C., et al. 2013, Nature, 495, 344
Walter, F., Decarli, R., Carilli, C., et al. 2012, Nature, 486, 233
Wang, T., Elbaz, D., Daddi, E., et al. 2016, ApJ, 828, 56
Wang, W.-H., Cowie, L. L., Barger, A. J., & Williams, J. P. 2011, ApJ, 726, L18
Wardlow, J. L., Smail, I., Coppin, K. E. K., et al. 2011, MNRAS, 415, 1479
Weiß, A., De Breuck, C., Marrone, D. P., et al. 2013, ApJ, 767, 88
Weiß, A., Kovács, A., Coppin, K., et al. 2009, ApJ, 707, 1201
Younger, J. D., Fazio, G. G., Huang, J.-S., et al. 2007, ApJ, 671, 1531
Younger, J. D., Fazio, G. G., Huang, J.-S., et al. 2009, ApJ, 704, 803
Yun, M. S., Aretxaga, I., Gurwell, M. A., et al. 2015, MNRAS, 454, 3485
Yun, M. S., Reddy, N. A., & Condon, J. J. 2001, ApJ, 554, 803
Zavala, J. A., Aretxaga, I., & Hughes, D. H. 2014, MNRAS, 443, 2384

8. Appendix

Table 3: UV-NIR photometry for sources drawn from COSMOS2015. Data is in AB magnitudes with photometric offsets applied according to Ilbert et al. (2009) and Salvato et al. (2011).

Source AzTEC	UVISTA ID	u+	B	V	g+	r+	i+	z++	Y	J	H	Ks	IRAC1	IRAC2	IRAC3	IRAC4
C2a	842140	–	27.3±0.4	26.2±0.3	26.1±0.1	25.9±0.2	25.6±0.1	25.7±0.3	25.4±1.0	24.5±0.4	23.8±0.3	23.1±0.2	21.6±0.1	20.9±0.1	20.8±0.1	20.1±0.1
C4	797542	–	–	–	29.5±0.8	28.1±0.3	27.2±0.2	26.4±0.4	–	–	24.8±0.4	23.9±0.3	22.1±0.1	21.6±0.1	21.1±0.1	20.7±0.1
C5	786213	28.5±0.8	–	–	27.8±0.2	26.0±0.2	25.1±0.1	24.9±0.1	25.0±0.4	25.1±0.6	24.5±0.4	23.4±0.2	22.2±0.1	21.9±0.1	21.1±0.2	21.0±0.1
C6b	683281	26.6±0.4	27.2±0.3	26.3±0.3	26.3±0.1	25.8±0.2	25.2±0.1	25.6±0.3	25.5±0.6	24.1±0.2	22.9±0.1	22.4±0.1	21.1±0.1	20.5±0.1	20.3±0.1	20.6±0.1
C7	634466	27.3±0.3	–	–	27.4±0.3	26.8±0.2	26.4±0.3	24.9±0.7	25.5±0.6	25.2±0.8	–	23.8±0.3	23.0±0.1	22.7±0.1	21.9±0.2	21.3±0.2
C8a	427059	–	–	–	28.4±0.5	28.3±0.6	27.1±0.4	26.6±0.5	25.9±0.5	24.5±0.3	24.6±0.3	23.8±0.1	22.9±0.1	22.3±0.1	22.5±0.3	–
C8b	428021	27.1±0.3	26.7±0.2	25.3±0.2	25.9±0.1	25.2±0.1	24.8±0.1	24.0±0.1	23.6±0.1	22.2±0.1	21.6±0.1	20.9±0.1	20.1±0.1	19.8±0.1	19.8±0.1	20.1±0.2
C9a	682558	–	27.1±0.4	25.9±0.3	25.9±0.1	25.2±0.1	24.6±0.1	24.9±0.2	24.7±0.5	23.6±0.2	22.2±0.1	21.7±0.1	20.9±0.1	20.5±0.1	20.4±0.1	20.2±0.1
C9b	681603	–	26.5±0.2	25.3±0.1	25.8±0.1	25.0±0.1	24.5±0.1	24.3±0.1	24.5±0.3	23.3±0.1	22.1±0.1	21.6±0.1	20.6±0.1	20.2±0.1	19.9±0.1	19.9±0.1
C9c	681834	28.7±0.9	26.7±0.3	26.4±0.4	26.2±0.1	25.6±0.2	25.4±0.1	25.5±0.3	25.4±0.9	24.2±0.4	23.2±0.2	22.4±0.1	21.2±0.1	20.7±0.1	20.5±0.1	20.5±0.1
C10b	841273	27.8±0.4	–	26.9±0.5	27.9±0.3	26.6±0.3	26.0±0.1	25.5±0.3	26.0±0.6	25.0±0.4	23.7±0.2	22.9±0.1	21.4±0.1	20.8±0.1	20.7±0.1	20.3±0.1
C11	505526	25.7±0.5	25.9±0.3	25.8±0.5	25.7±0.1	25.0±0.3	24.8±0.1	24.1±0.1	24.3±0.4	23.1±0.2	22.3±0.1	21.7±0.1	21.5±0.1	20.7±0.1	20.4±0.1	19.7±0.1
C12	582130	26.9±0.5	26.4±0.2	25.3±0.1	25.7±0.1	24.9±0.1	24.7±0.1	24.6±0.1	24.7±0.2	24.0±0.2	23.8±0.2	23.0±0.1	22.0±0.1	21.5±0.1	21.7±0.3	21.5±0.3
C13a	616280	25.4±0.2	25.7±0.2	24.8±0.2	25.9±0.1	25.0±0.1	25.1±0.1	24.7±0.2	24.2±0.3	23.1±0.2	22.9±0.2	21.7±0.1	21.1±0.1	20.4±0.1	20.3±0.1	20.6±0.1
C13b	614777	26.6±0.3	26.5±0.2	25.6±0.2	26.0±0.1	25.6±0.1	25.0±0.1	25.0±0.1	25.6±0.7	24.2±0.2	24.2±0.3	24.5±0.5	22.4±0.1	21.6±0.1	21.5±0.2	21.3±0.2
C14	763214	28.1±0.4	27.5±0.2	26.8±0.3	27.2±0.1	26.8±0.2	26.0±0.1	25.6±0.1	25.1±0.3	25.5±0.6	25.3±0.6	24.7±0.5	22.7±0.1	22.5±0.1	–	21.9±0.3
C16a	646184	–	–	–	–	27.1±0.2	25.9±0.1	27.5±0.8	–	24.9±0.5	24.0±0.3	22.9±0.1	21.5±0.1	20.8±0.1	20.7±0.1	20.6±0.1
C16b	645724	26.8±0.2	26.4±0.2	25.8±0.2	25.7±0.1	25.0±0.1	25.4±0.1	25.0±0.1	24.8±0.2	23.6±0.1	22.9±0.1	22.2±0.1	20.9±0.1	20.4±0.1	20.2±0.1	20.6±0.1
C18	942076	–	26.3±0.2	25.4±0.2	–	24.6±0.1	24.2±0.1	23.9±0.1	23.5±0.1	22.8±0.1	21.9±0.1	21.4±0.1	20.0±0.1	19.5±0.1	19.7±0.1	19.6±0.1
C19	395780	24.1±0.1	23.8±0.1	22.9±0.1	23.1±0.1	22.8±0.1	22.6±0.1	22.5±0.1	22.4±0.1	22.1±0.1	21.7±0.1	21.6±0.1	20.9±0.1	20.5±0.1	20.5±0.1	20.3±0.1
C20	759562	–	25.9±0.2	25.0±0.2	25.0±0.1	24.7±0.1	24.3±0.1	24.6±0.2	24.1±0.3	23.6±0.2	22.7±0.1	22.4±0.2	21.9±0.1	21.5±0.1	21.2±0.2	21.2±0.3
C22a	902320	23.8±0.1	24.1±0.1	23.5±0.1	23.5±0.1	23.4±0.1	23.1±0.1	22.7±0.1	22.3±0.1	21.6±0.1	21.4±0.1	21.1±0.1	19.9±0.1	19.4±0.1	19.5±0.1	–
C24a	709365	27.5±0.4	26.7±0.3	25.4±0.2	28.3±0.4	26.6±0.4	25.7±0.1	25.1±0.2	24.5±0.3	23.1±0.1	22.5±0.1	21.7±0.1	20.4±0.1	19.9±0.1	20.2±0.1	20.6±0.2
C24b	709850	25.5±0.2	25.4±0.1	24.3±0.1	24.5±0.1	24.1±0.1	23.7±0.1	23.3±0.1	22.9±0.1	21.6±0.1	21.3±0.1	20.9±0.1	19.9±0.1	19.6±0.1	19.6±0.1	20.1±0.2
C25	427827	26.2±0.3	26.0±0.1	25.2±0.1	25.3±0.1	25.0±0.1	24.9±0.1	24.4±0.1	24.3±0.3	23.2±0.1	22.5±0.1	21.9±0.1	20.5±0.1	19.7±0.1	20.0±0.1	20.1±0.1
C26	813955	27.3±0.3	–	–	–	26.6±0.4	25.5±0.1	25.4±0.2	25.2±0.6	–	25.1±0.8	23.6±0.4	22.9±0.1	23.2±0.1	–	22.5±0.5
C27	534452	27.2±0.3	26.8±0.3	26.2±0.3	26.5±0.1	25.8±0.2	25.6±0.1	25.4±0.3	24.9±1.0	24.5±0.5	23.4±0.2	22.6±0.2	21.2±0.1	20.6±0.1	20.4±0.1	20.3±0.1
C28a	604304	24.1±0.1	24.1±0.1	23.6±0.1	23.6±0.1	23.5±0.1	23.4±0.1	23.2±0.1	23.0±0.1	22.3±0.1	21.9±0.1	21.3±0.1	20.6±0.1	20.2±0.1	20.4±0.1	20.5±0.2
C28b	602117	27.7±0.3	26.8±0.2	26.0±0.2	26.1±0.1	25.7±0.1	25.4±0.1	25.1±0.1	24.8±0.2	23.9±0.1	23.2±0.1	22.4±0.1	21.0±0.1	20.6±0.1	20.4±0.1	21.0±0.3
C29	473780	27.4±0.3	26.4±0.2	25.9±0.2	26.1±0.1	25.5±0.1	25.1±0.1	24.6±0.1	24.4±0.2	23.5±0.1	23.1±0.1	22.2±0.1	21.4±0.1	21.1±0.1	21.0±0.2	–
C33a	810228	24.5±0.1	24.5±0.1	23.7±0.1	24.0±0.1	23.4±0.1	23.3±0.1	22.9±0.1	22.6±0.1	21.9±0.1	21.4±0.1	21.0±0.1	20.3±0.1	19.8±0.1	19.8±0.1	20.0±0.1
C34a	589074	–	27.1±0.3	25.1±0.1	25.9±0.1	24.7±0.1	24.4±0.1	24.2±0.1	24.2±0.2	23.7±0.1	23.4±0.1	23.1±0.1	22.2±0.1	21.6±0.1	21.2±0.2	20.9±0.2
C34b	590368	<25.5	26.3±0.2	25.7±0.2	26.01±0.05	25.8±0.2	25.8±0.2	25.2±0.3	<24.8	24.3±0.2	23.6±0.2	22.66±0.07	21.62±0.02	21.074±0.007	20.8±0.1	21.2±0.4
C35	686297	28.8±1.0	27.3±0.4	26.4±0.4	26.2±0.1	25.8±0.2	25.1±0.1	25.3±0.2	24.7±0.2	24.0±0.2	22.8±0.1	22.5±0.1	21.5±0.1	21.2±0.1	20.8±0.2	21.3±0.4
C36	518177	25.0±0.1	24.7±0.1	23.7±0.1	23.9±0.1	23.4±0.1	23.2±0.1	22.9±0.1	22.7±0.1	22.0±0.1	21.4±0.1	20.8±0.1	19.8±0.1	19.5±0.1	19.6±0.2	19.7±0.1
C38	702910	–	–	–	28.0±0.3	27.1±0.4	26.5±0.1	25.9±0.3	25.7±0.5	24.4±0.2	23.3±0.1	22.5±0.1	20.8±0.1	20.2±0.1	20.2±0.1	20.3±0.2
C39	462117	28.7±0.6	–	–	28.3±0.2	28.3±0.3	28.2±0.5	26.8±0.5	–	25.5±0.7	24.9±0.5	24.2±0.4	22.0±0.1	21.3±0.1	21.1±0.1	20.6±0.1
C41	700004	23.8±0.1	24.2±0.1	23.5±0.1	23.7±0.1	23.2±0.1	22.8±0.1	22.1±0.1	21.9±0.1	21.5±0.1	21.2±0.1	20.7±0.1	19.6±0.1	19.5±0.1	19.6±0.1	–
C42	815840	–	–	25.3±0.4	26.6±0.3	25.1±0.3	24.2±0.1	24.0±0.2	25.2±0.3	23.4±0.3	22.3±0.2	21.6±0.1	22.0±0.1	21.2±0.1	21.1±0.1	–
C43b	484892	24.3±0.2	24.8±0.2	23.8±0.2	23.8±0.1	23.6±0.1	23.0±0.1	22.9±0.1	22.4±0.3	21.2±0.1	20.9±0.1	20.2±0.1	20.9±0.1	20.5±0.1	20.0±0.1	21.2±0.5
C44a	346234	–	–	–	–	26.9±0.5	27.6±0.4	–	26.2±0.8	24.4±0.3	23.6±0.2	22.8±0.1	21.5±0.1	20.7±0.1	20.6±0.1	21.0±0.3
C44b	350733	23.2±0.1	23.5±0.1	22.5±0.1	22.6±0.1	22.1±0.1	21.6±0.1	20.9±0.1	20.8±0.1	20.5±0.1	20.4±0.1	19.9±0.1	22.0±0.8	20.1±0.1	19.2±0.1	19.0±0.1
C45	826154	23.8±0.1	24.1±0.1	22.8±0.1	23.0±0.1	22.5±0.1	22.2±0.1	22.0±0.1	21.8±0.1	21.2±0.1	20.3±0.1	19.9±0.1	19.8±0.1	19.5±0.1	19.3±0.1	17.9±0.1
C46	849028	–	26.9±0.4	26.1±0.4	26.0±0.1	25.3±0.2	25.2±0.1	25.8±0.6	23.9±0.3	23.6±0.3	22.8±0.2	22.4±0.2	21.8±0.1	21.2±0.1	20.6±0.1	20.8±0.1
C47	475050	24.6±0.1	24.7±0.1	23.8±0.1	24.0±0.1	23.6±0.1	23.4±0.1	23.0±0.1	22.7±0.1	21.5±0.1	21.1±0.1	20.7±0.1	20.0±0.1	19.7±0.1	19.8±0.1	20.2±0.1
C48a	887050	26.0±0.2	25.9±0.1	25.0±0.1	25.4±0.1	24.6±0.1	24.3±0.1	23.7±0.1	23.5±0.1	22.3±0.1	21.8±0.1	21.3±0.1	20.2±0.1	19.9±0.1	20.1±0.1	20.0±0.1
C48b	887401	<25.5	<27.0	<26.2	26.18±0.07	25.7±0.2	25.4±0.2	25.2±0.3	24.4±0.2	23.08±0.08	22.25±0.05	21.67±0.03	20.97±0.01	20.757±0.007	20.9±0.1	21.3±0.4
C50	552644	–	–	–	27.9±0.2	27.4±0.2	27.1±0.2	27.8±0.8	–	–	25.3±0.8	23.3±0.2	22.0±0.1	21.3±0.1	21.0±0.1	20.9±0.1

Table 3: continued.

Source AzTEC	UVISTA ID	u+	B	V	g+	r+	i+	z++	Y	J	H	Ks	IRAC1	IRAC2	IRAC3	IRAC4
C51b	456882	25.5±0.1	25.5±0.1	25.0±0.1	25.0±0.1	24.4±0.1	24.0±0.1	23.0±0.1	22.5±0.1	22.1±0.1	21.8±0.1	21.3±0.1	20.5±0.1	20.6±0.1	20.3±0.2	–
C52	694031	25.3±0.1	25.1±0.1	24.3±0.1	24.4±0.1	23.5±0.1	22.7±0.1	21.8±0.1	21.2±0.1	20.6±0.1	20.1±0.1	19.7±0.1	18.6±0.1	18.4±0.1	18.9±0.1	–
C53	593993	28.1±0.5	27.8±0.4	26.9±0.4	27.1±0.1	26.7±0.3	26.4±0.1	26.0±0.3	–	24.2±0.3	24.2±0.3	23.3±0.2	21.7±0.1	21.3±0.1	21.4±0.2	22.7±0.8
C54	439437	28.3±0.9	26.7±0.3	25.4±0.2	26.0±0.1	25.1±0.1	25.1±0.1	24.7±0.2	24.7±0.5	24.2±0.3	23.5±0.2	23.0±0.2	22.5±0.1	21.7±0.1	21.6±0.2	21.6±0.3
C55a	413145	27.9±0.4	26.9±0.2	25.5±0.2	26.0±0.1	25.4±0.1	25.1±0.1	24.8±0.1	24.4±0.3	23.9±0.2	22.6±0.1	22.2±0.1	20.5±0.1	20.1±0.1	20.0±0.1	20.0±0.1
C55b	412615	27.5±0.2	26.7±0.2	25.6±0.1	25.8±0.1	25.3±0.1	25.2±0.1	24.8±0.1	24.5±0.3	24.3±0.3	23.2±0.1	22.5±0.1	21.3±0.1	20.8±0.1	20.7±0.1	20.6±0.1
C56	703515	28.1±0.6	27.7±0.5	25.5±0.2	27.7±0.2	25.1±0.1	24.9±0.1	24.4±0.1	24.1±0.1	23.5±0.1	23.2±0.1	22.5±0.1	21.4±0.1	20.8±0.1	21.1±0.3	20.8±0.2
C58	304628	26.5±0.3	27.1±0.3	26.4±0.3	26.7±0.1	26.2±0.2	25.4±0.1	25.3±0.2	25.4±0.4	24.8±0.3	25.5±0.9	24.0±0.2	22.9±0.1	22.3±0.1	21.3±0.3	21.3±0.3
C59	872523	24.2±0.1	24.2±0.1	23.4±0.1	23.6±0.1	23.0±0.1	22.4±0.1	21.7±0.1	21.1±0.1	20.6±0.1	20.2±0.1	19.8±0.1	18.7±0.1	18.5±0.1	19.1±0.1	18.9±0.5
C60b	697712	27.6±0.3	–	27.2±0.5	27.2±0.1	26.4±0.2	25.3±0.1	25.1±0.1	24.9±0.4	24.5±0.3	24.6±0.5	24.3±0.5	23.2±0.1	23.1±0.2	–	22.8±0.9
C61	842703	–	–	27.2±0.6	27.9±0.2	27.1±0.1	26.5±0.1	26.0±0.4	25.7±0.9	24.5±0.4	25.4±1.0	24.0±0.4	22.0±0.1	21.2±0.1	20.6±0.1	19.9±0.1
C65	702734	24.6±0.1	24.7±0.1	24.1±0.1	24.2±0.1	23.8±0.1	23.4±0.1	22.8±0.1	22.1±0.1	21.4±0.1	20.9±0.1	20.4±0.1	19.0±0.1	18.6±0.1	18.9±0.1	19.6±0.1
C67	567572	25.7±0.2	25.1±0.1	23.7±0.1	24.2±0.1	23.6±0.1	23.5±0.1	23.5±0.1	23.4±0.1	23.1±0.1	22.7±0.1	22.5±0.1	21.2±0.1	20.9±0.1	21.0±0.2	20.7±0.2
C69b	560381	–	–	25.7±0.2	26.3±0.1	24.8±0.1	24.3±0.1	24.2±0.1	24.4±0.2	23.4±0.1	23.1±0.1	22.6±0.1	21.7±0.1	21.3±0.1	21.3±0.3	21.0±0.3
C70	494956	28.6±0.5	27.7±0.3	26.3±0.2	26.7±0.1	26.0±0.2	25.8±0.1	25.7±0.2	25.5±0.3	24.8±0.3	24.7±0.4	23.9±0.2	22.5±0.1	21.9±0.1	21.0±0.2	–
C72	515355	25.3±0.1	25.7±0.1	24.9±0.1	25.3±0.1	24.8±0.1	24.8±0.1	24.5±0.1	23.8±0.1	23.4±0.1	23.0±0.1	22.3±0.1	21.3±0.1	21.0±0.1	20.5±0.2	20.9±0.3
C74a	701870	26.26±0.09	26.0±0.1	25.9±0.2	26.02±0.04	25.5±0.1	25.6±0.2	25.1±0.2	<24.8	<24.7	<24.3	23.2±0.4	22.96±0.03	22.52±0.02	22.1±0.4	22.5±0.6
C76	593906	27.5±0.2	–	26.2±0.3	26.8±0.1	25.9±0.2	25.0±0.1	24.5±0.1	24.5±0.1	23.6±0.1	22.6±0.1	22.0±0.1	21.2±0.1	20.4±0.1	20.3±0.1	20.2±0.1
C77a	441615	–	–	–	–	26.4±0.3	27.1±0.3	25.9±0.3	–	25.4±0.8	24.0±0.3	23.1±0.2	21.8±0.1	21.1±0.1	21.0±0.1	20.5±0.1
C78b	457720	–	–	–	–	26.9±0.4	25.7±0.1	26.2±0.4	25.8±0.5	25.1±0.4	24.6±0.3	24.3±0.2	–	–	–	–
C79	610723	27.1±0.3	27.4±0.4	27.0±0.6	26.7±0.1	26.1±0.1	25.4±0.1	24.9±0.2	24.8±0.5	23.4±0.2	22.1±0.1	21.4±0.1	20.3±0.1	19.9±0.1	19.8±0.1	20.0±0.1
C80a	747545	27.5±0.3	27.1±0.2	26.5±0.3	26.5±0.1	25.9±0.1	25.4±0.1	25.3±0.2	25.0±0.2	24.4±0.2	23.4±0.1	22.7±0.1	20.9±0.1	20.4±0.1	20.2±0.1	20.6±0.1
C80b	746328	–	27.4±0.3	26.8±0.4	27.8±0.3	26.4±0.3	27.6±0.6	26.1±0.4	26.0±0.7	24.6±0.3	23.6±0.2	22.7±0.1	21.1±0.1	20.6±0.1	20.4±0.1	20.9±0.2
C84a	414489	28.1±0.9	27.6±0.6	–	27.1±0.2	26.1±0.3	25.6±0.1	25.4±0.3	24.9±0.9	–	23.7±0.3	22.8±0.2	22.0±0.1	21.3±0.1	21.8±0.3	20.7±0.1
C84b	410945	24.9±0.1	25.0±0.1	24.2±0.1	24.3±0.1	23.9±0.1	23.4±0.1	22.8±0.1	22.4±0.1	21.1±0.1	20.6±0.1	20.0±0.1	18.8±0.1	18.5±0.1	18.7±0.1	19.1±0.1
C86	652663	26.3±0.2	25.6±0.1	24.2±0.1	24.8±0.1	23.7±0.1	23.2±0.1	22.5±0.1	22.3±0.1	21.7±0.1	21.6±0.1	21.4±0.1	20.4±0.1	20.0±0.1	19.8±0.1	19.4±0.1
C90c	645708	25.5±0.1	25.5±0.1	24.6±0.1	24.9±0.1	24.3±0.1	24.1±0.1	23.9±0.1	23.6±0.1	23.0±0.1	22.3±0.1	21.9±0.1	20.8±0.1	20.5±0.1	20.8±0.2	21.1±0.3
C91	722424	–	–	–	–	28.6±0.6	–	26.9±0.3	–	–	24.8±0.5	24.2±0.5	22.2±0.1	21.5±0.1	21.6±0.1	21.9±0.2
C92b	793275	27.1±0.2	27.1±0.3	26.3±0.3	26.8±0.1	26.3±0.2	25.7±0.1	25.2±0.2	26.5±1.0	25.3±0.5	25.4±0.7	24.4±0.3	22.7±0.1	21.9±0.1	21.7±0.2	21.1±0.2
C93	587450	–	27.8±0.5	26.0±0.2	26.8±0.1	25.7±0.1	25.9±0.1	25.2±0.2	24.7±0.3	23.8±0.2	22.6±0.1	22.1±0.1	20.7±0.1	20.3±0.1	20.2±0.1	19.5±0.1
C95	600465	24.0±0.1	24.4±0.1	23.7±0.1	23.8±0.1	23.5±0.1	23.0±0.1	22.4±0.1	22.2±0.1	21.6±0.1	21.3±0.1	20.7±0.1	19.5±0.1	19.2±0.1	19.2±0.1	19.7±0.1
C97a	679317	25.0±0.1	25.1±0.1	24.1±0.1	24.3±0.1	24.0±0.1	23.8±0.1	23.6±0.1	23.5±0.1	23.2±0.1	23.0±0.1	22.7±0.1	21.9±0.1	21.5±0.1	20.7±0.1	–
C97b	678384	25.6±0.2	26.0±0.1	25.2±0.1	25.3±0.1	25.2±0.1	24.6±0.1	24.1±0.1	23.5±0.1	22.5±0.1	21.9±0.1	21.2±0.1	19.8±0.1	19.6±0.1	19.5±0.1	19.9±0.1
C98	518250	–	27.9±0.5	–	29.1±0.8	27.8±0.3	27.0±0.2	26.2±0.5	25.2±0.3	23.9±0.2	23.0±0.1	22.1±0.1	20.5±0.1	20.0±0.1	20.2±0.1	–
C100a	575024	26.7±0.4	26.8±0.2	26.4±0.3	26.4±0.1	26.4±0.4	25.5±0.1	24.9±0.1	23.9±0.1	22.9±0.1	22.4±0.1	21.8±0.1	20.5±0.1	20.2±0.1	20.3±0.1	20.7±0.2
C100b	576755	28.0±0.4	27.0±0.2	27.4±0.6	27.2±0.1	26.4±0.2	26.9±0.2	26.1±0.3	25.6±0.4	25.2±0.4	24.4±0.2	23.9±0.1	22.1±0.1	21.6±0.1	21.0±0.2	21.0±0.1
C101b	794601	26.1±0.3	25.8±0.1	24.6±0.1	25.0±0.1	24.4±0.1	24.3±0.1	24.1±0.1	23.7±0.2	23.4±0.1	23.4±0.2	23.1±0.2	22.6±0.1	22.5±0.1	–	–
C103	423273	27.6±0.5	27.3±0.5	–	26.4±0.1	26.1±0.3	25.5±0.1	25.3±0.2	24.9±0.6	23.6±0.2	22.4±0.1	21.8±0.1	20.4±0.1	19.6±0.1	19.9±0.1	20.2±0.1
C105	623091	26.0±0.2	25.7±0.1	24.9±0.1	25.1±0.1	24.6±0.1	24.4±0.1	23.8±0.1	23.4±0.1	22.4±0.1	21.8±0.1	21.1±0.1	19.9±0.1	19.5±0.1	19.3±0.1	20.0±0.1
C109	776550	–	26.6±0.2	25.7±0.2	26.1±0.1	25.4±0.1	24.9±0.1	24.5±0.1	24.4±0.3	23.2±0.1	22.3±0.1	21.5±0.1	20.3±0.1	19.9±0.1	19.8±0.1	20.0±0.1
C111	599375	–	–	–	28.6±0.4	27.3±0.4	27.1±0.2	26.6±0.5	26.1±0.8	25.2±0.5	24.3±0.3	23.7±0.2	21.5±0.1	20.9±0.1	20.6±0.1	20.9±0.2
C112	394010	25.5±0.2	25.3±0.1	24.4±0.1	24.8±0.1	24.2±0.1	23.8±0.1	23.2±0.1	22.8±0.1	21.5±0.1	21.3±0.1	20.8±0.1	19.8±0.1	19.5±0.1	19.7±0.1	20.4±0.3
C113	791065	23.5±0.1	23.7±0.1	23.2±0.1	23.2±0.1	23.1±0.1	22.9±0.1	22.7±0.1	22.5±0.1	21.7±0.1	21.7±0.1	21.3±0.1	20.3±0.1	19.9±0.1	20.0±0.1	20.2±0.2
C116	501111	–	–	27.2±0.5	26.9±0.1	26.5±0.2	26.5±0.1	26.1±0.3	25.1±0.5	24.3±0.2	23.5±0.2	22.9±0.1	21.1±0.1	20.6±0.1	20.6±0.1	20.8±0.1
C117	685079	28.2±0.5	27.6±0.4	26.8±0.3	27.1±0.1	26.1±0.2	25.6±0.1	25.0±0.1	24.8±0.2	23.7±0.1	22.7±0.1	22.1±0.1	20.5±0.1	20.2±0.1	20.2±0.1	20.5±0.1
C122a	644904	24.3±0.1	24.5±0.1	23.8±0.1	24.0±0.1	23.4±0.1	23.0±0.1	22.5±0.1	22.3±0.1	21.8±0.1	21.7±0.1	21.2±0.1	21.3±0.1	21.4±0.1	21.1±0.4	21.5±0.5
C123	375061	27.6±0.3	27.3±0.3	26.2±0.2	26.4±0.1	25.8±0.2	25.3±0.1	24.7±0.1	24.4±0.1	22.9±0.1	22.3±0.1	21.7±0.1	20.3±0.1	19.9±0.1	20.0±0.1	20.5±0.2
C124	854544	<25.5	26.6±0.3	26.1±0.3	<26.1	25.8±0.2	25.2±0.2	24.5±0.1	23.7±0.1	22.80±0.08	21.98±0.05	21.34±0.04	20.21±0.01	19.860±0.007	19.90±0.07	20.5±0.2
C127	851363	24.9±0.1	25.1±0.1	24.4±0.1	24.5±0.1	24.2±0.1	23.8±0.1	23.4±0.1	22.9±0.1	22.0±0.1	21.8±0.1	21.3±0.1	20.1±0.1	19.7±0.1	19.6±0.1	19.7±0.1

Table 4: UV-NIR photometry for sources with manually extracted photometry. Data is in AB magnitudes with photometric offsets applied according to Ilbert et al. (2009) and Salvato et al. (2011).

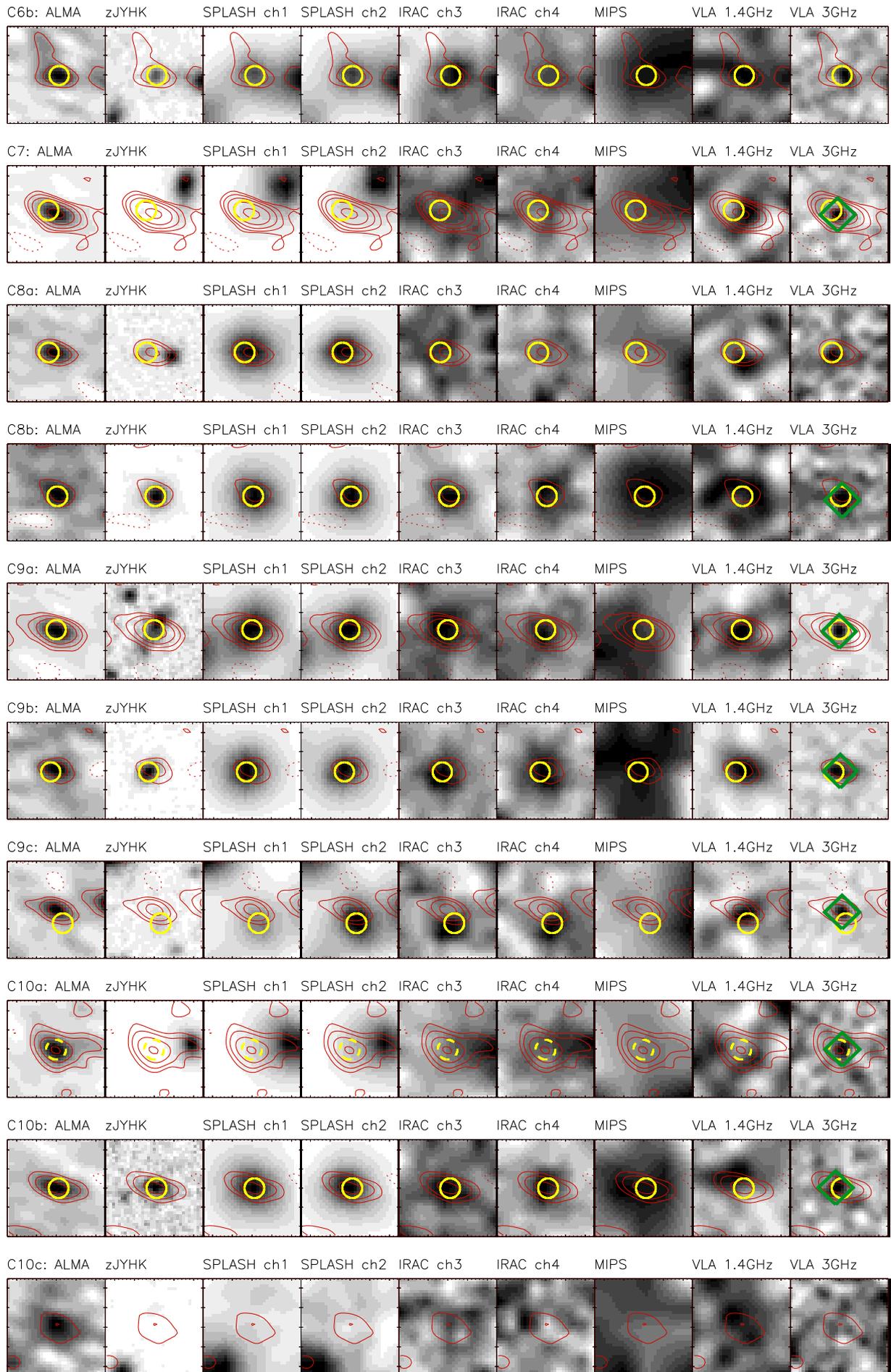| Source AzTEC	UVISTA u+	B	V	g+	r+	i+	z++	Y	J	H	Ks	IRAC1	IRAC2	IRAC3	IRAC4
C1a	–	–	–	–	–	–	–	–	–	–	–	21.0±0.1	21.1±0.1	20.7±0.1	20.1±0.2
C2b	–	–	–	–	–	–	–	–	–	–	25.1±0.2	23.2±0.1	22.70±0.09	21.92±0.09	21.3±0.2
C6a	–	27.3±0.4	–	–	26.1±0.3	25.9±0.3	–	24.5±0.2	23.5±0.2	23.0±0.2	22.5±0.2	21.1±0.1	20.50±0.03	20.32±0.05	20.6±0.1
C10a	–	–	–	–	–	–	–	–	–	–	–	–	–	21.19±0.09	21.8±0.2
C15	–	–	–	26.9±0.5	–	26.8±0.3	–	–	–	–	24.6±0.2	23.0±0.1	22.24±0.09	22.42±0.09	21.0±0.2
C17	–	–	–	–	–	–	–	24.2±0.2	24.9±0.2	24.3±0.2	23.2±0.2	22.1±0.2	22.7±0.1	22.9±0.1	21.2±0.2
C21	–	–	–	–	–	–	–	–	–	–	–	21.3±0.1	20.82±0.10	20.30±0.09	20.1±0.2
C22b	–	–	–	–	–	–	–	–	–	–	–	–	–	–	–
C23	24.7±0.4	23.9±0.4	23.8±0.3	23.0±0.5	22.5±0.3	23.1±0.3	23.5±0.2	20.7±0.2	20.8±0.2	20.9±0.2	20.5±0.2	19.6±0.1	19.23±0.09	19.42±0.09	19.9±0.2
C31a	–	–	–	–	–	–	–	–	–	–	–	21.3±0.1	20.92±0.09	20.86±0.09	20.3±0.2
C31b	–	–	–	–	–	–	–	–	–	–	–	22.1±0.1	21.84±0.09	21.38±0.09	21.5±0.2
C32	–	–	–	–	–	–	–	–	–	–	–	21.3±0.1	20.99±0.09	21.62±0.09	19.8±0.2
C37	–	–	–	–	–	–	–	–	–	24.8±0.2	24.0±0.2	22.5±0.1	21.63±0.09	21.78±0.09	20.7±0.2
C43a	–	–	–	–	–	–	–	–	–	–	–	21.2±0.1	20.77±0.09	20.72±0.09	21.3±0.2
C49	–	–	–	–	–	–	–	–	–	–	–	23.2±0.1	24.21±0.09	22.11±0.09	21.7±0.2
C51a	–	–	–	–	–	–	–	–	–	–	–	–	22.86±0.09	22.01±0.09	22.1±0.2
C60a	–	–	–	–	–	–	–	–	–	–	–	24.0±0.2	23.9±0.2	22.03±0.09	22.7±0.2
C62	25.8±0.4	25.0±0.4	24.9±0.3	24.5±0.5	24.2±0.3	24.9±0.3	25.2±0.2	21.9±0.2	22.3±0.2	23.3±0.2	–	23.4±0.1	22.73±0.09	21.77±0.09	21.9±0.2
C64	–	–	–	–	–	–	–	–	–	–	–	22.6±0.1	21.88±0.09	21.33±0.09	21.4±0.2
C66	–	–	–	–	–	–	–	–	21.6±0.2	21.3±0.2	20.9±0.2	19.6±0.1	19.33±0.09	19.52±0.09	19.8±0.2
C73	–	–	–	–	–	–	–	–	–	–	–	22.6±0.1	21.90±0.09	21.98±0.09	21.4±0.2
C77b	–	–	–	–	–	–	–	–	–	24.3±0.2	23.4±0.2	22.5±0.1	21.44±0.10	21.41±0.09	21.1±0.2
C81	–	–	–	–	–	–	–	–	–	–	–	23.9±0.1	23.70±0.09	21.83±0.09	–
C87	–	–	–	–	–	–	–	–	–	–	–	19.9±0.1	19.63±0.09	19.66±0.09	20.0±0.2
C88	–	–	–	–	–	–	–	–	–	–	–	22.1±0.1	21.67±0.09	21.59±0.10	22.4±0.2
C90a	–	–	–	–	–	–	–	–	22.5±0.2	21.9±0.2	–	20.7±0.1	20.40±0.09	20.34±0.09	20.5±0.2
C90b	–	–	–	–	–	–	–	–	22.5±0.2	21.9±0.2	–	20.7±0.1	20.40±0.09	20.34±0.09	20.5±0.2
C92a	–	–	–	–	–	–	–	–	–	–	–	21.3±0.1	20.65±0.09	20.10±0.09	20.2±0.2
C99	–	–	–	–	–	–	–	–	23.9±0.2	23.8±0.2	–	22.6±0.1	22.03±0.09	21.72±0.09	21.3±0.2
C101a	–	–	–	–	–	26.7±0.3	–	–	–	–	24.2±0.2	22.1±0.1	21.45±0.09	22.12±0.09	20.5±0.2
C107	–	–	–	–	–	–	–	–	–	–	–	24.2±0.1	22.98±0.09	21.70±0.09	20.8±0.2
C108	–	–	–	–	–	–	–	–	–	24.4±0.2	24.1±0.2	21.7±0.1	20.82±0.09	20.56±0.09	20.5±0.2
C115b	–	–	–	–	–	–	–	–	–	–	–	23.3±0.1	22.41±0.09	21.81±0.09	21.4±0.2
C118	–	–	–	–	–	–	–	24.2±0.2	24.4±0.2	23.9±0.2	22.9±0.2	21.1±0.1	20.78±0.09	20.02±0.09	19.7±0.2
C119	–	–	–	–	–	–	–	–	–	25.1±0.2	24.3±0.2	23.3±0.1	22.47±0.09	21.54±0.09	21.3±0.2
C122b	–	–	–	–	24.7±0.3	24.1±0.3	23.6±0.2	23.7±0.2	23.3±0.2	21.3±0.2	20.8±0.2	21.7±0.1	21.99±0.09	20.91±0.09	22.1±0.2
C126	–	–	–	26.3±0.5	25.3±0.3	25.1±0.3	24.7±0.2	24.1±0.2	24.0±0.2	23.8±0.2	23.2±0.2	22.2±0.1	21.69±0.09	21.77±0.09	21.3±0.2
C129	–	27.0±0.4	–	–	–	25.6±0.3	–	–	–	–	–	25.2±0.1	–	21.38±0.09	22.0±0.2
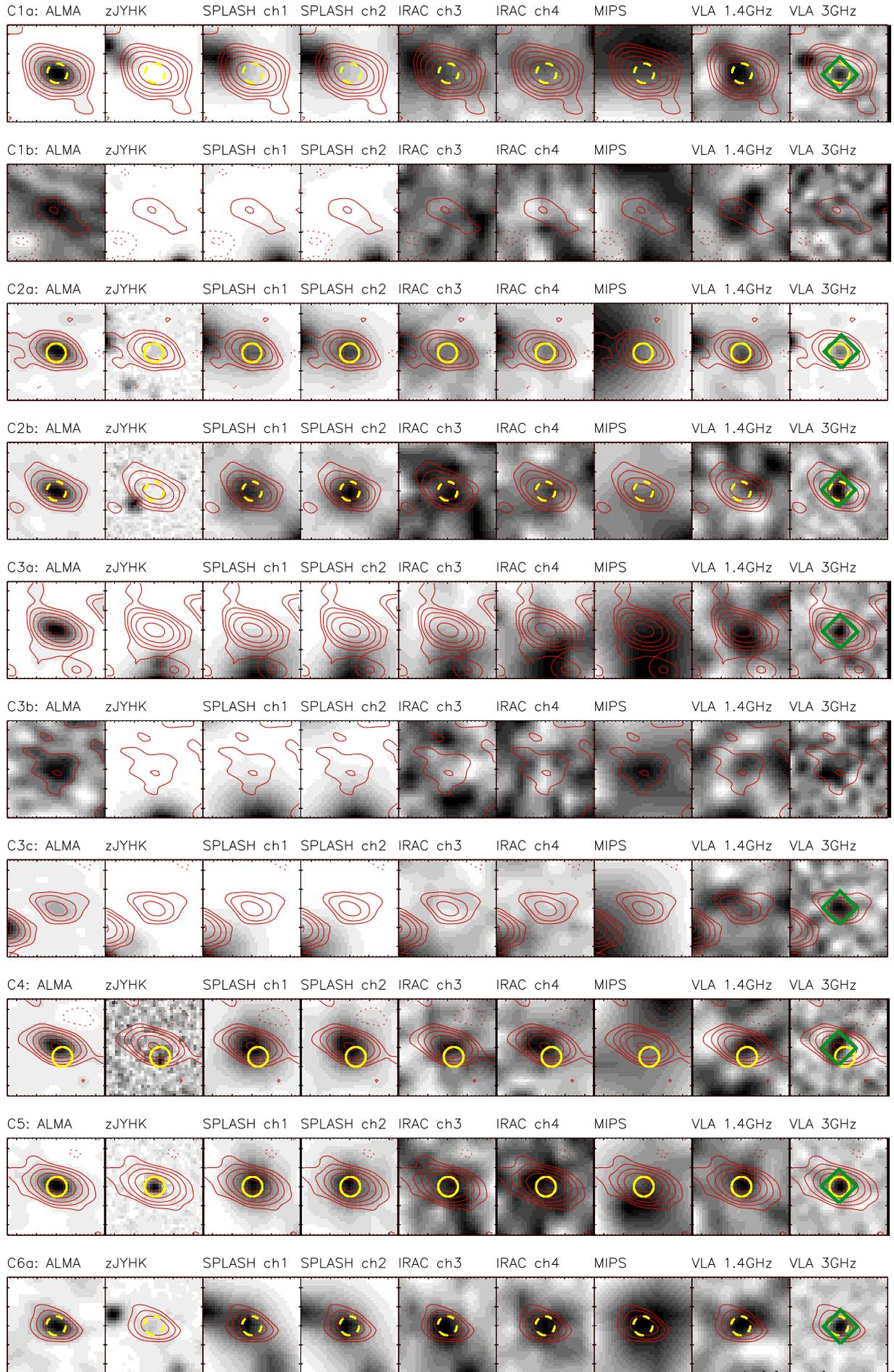
Fig. 10: Gray-scale images (5″ on the side) in various bands (indicated above each panel) for each ALMA detected SMG. The contours shown by solid lines represent the flux levels in the ALMA maps at $2^n \times$ rms for $n = 2, 3, 4...$ (negative contours at the same levels are shown by dotted lines). The assumed counterparts are encircled by a full yellow line if present in the COSMOS2015 catalog, otherwise by a dashed yellow line (indicating that the multi-wavelength photometry was specifically extracted here; see text for details). Radio counterparts at 3 GHz are marked by the green diamond.
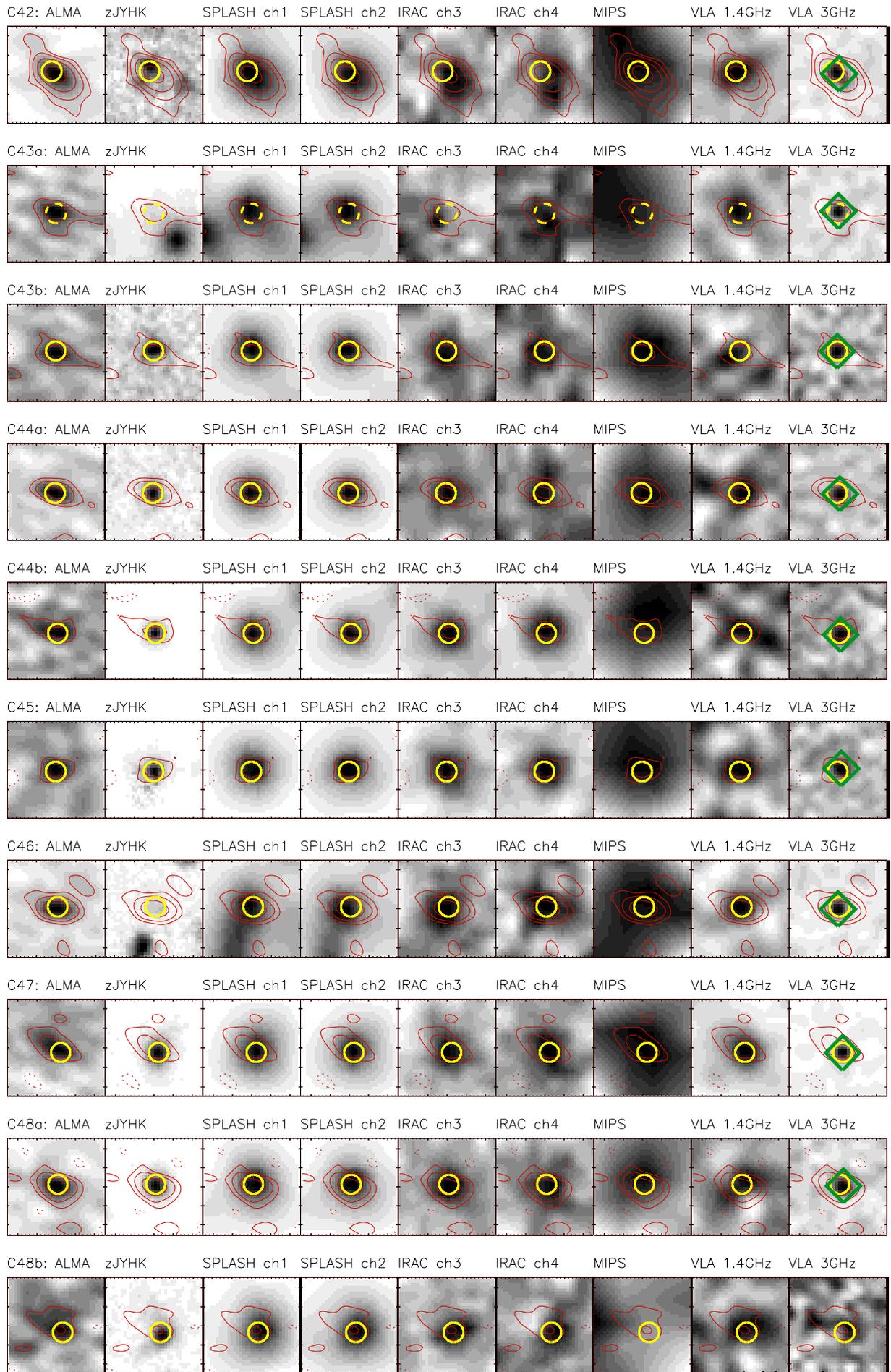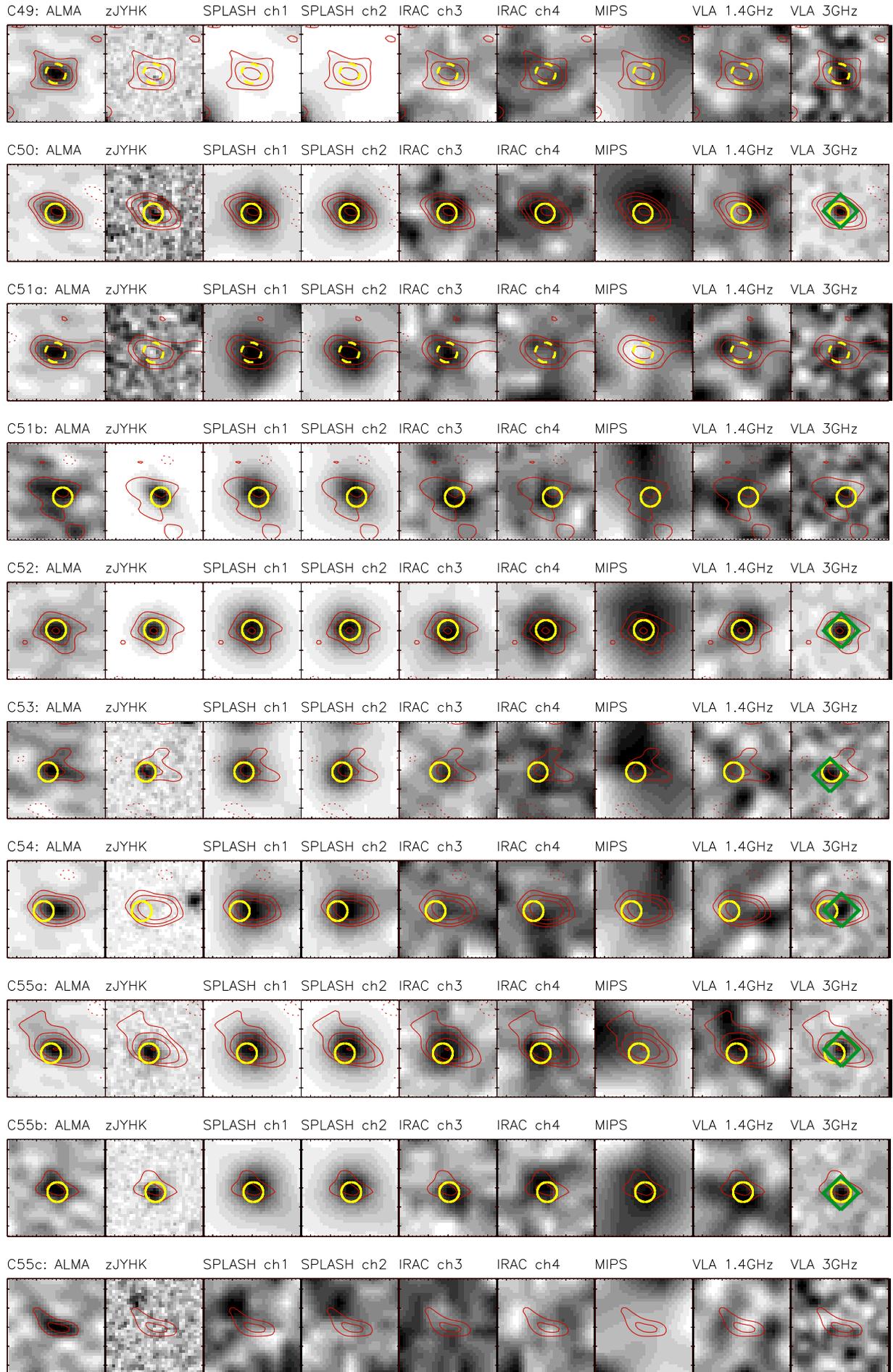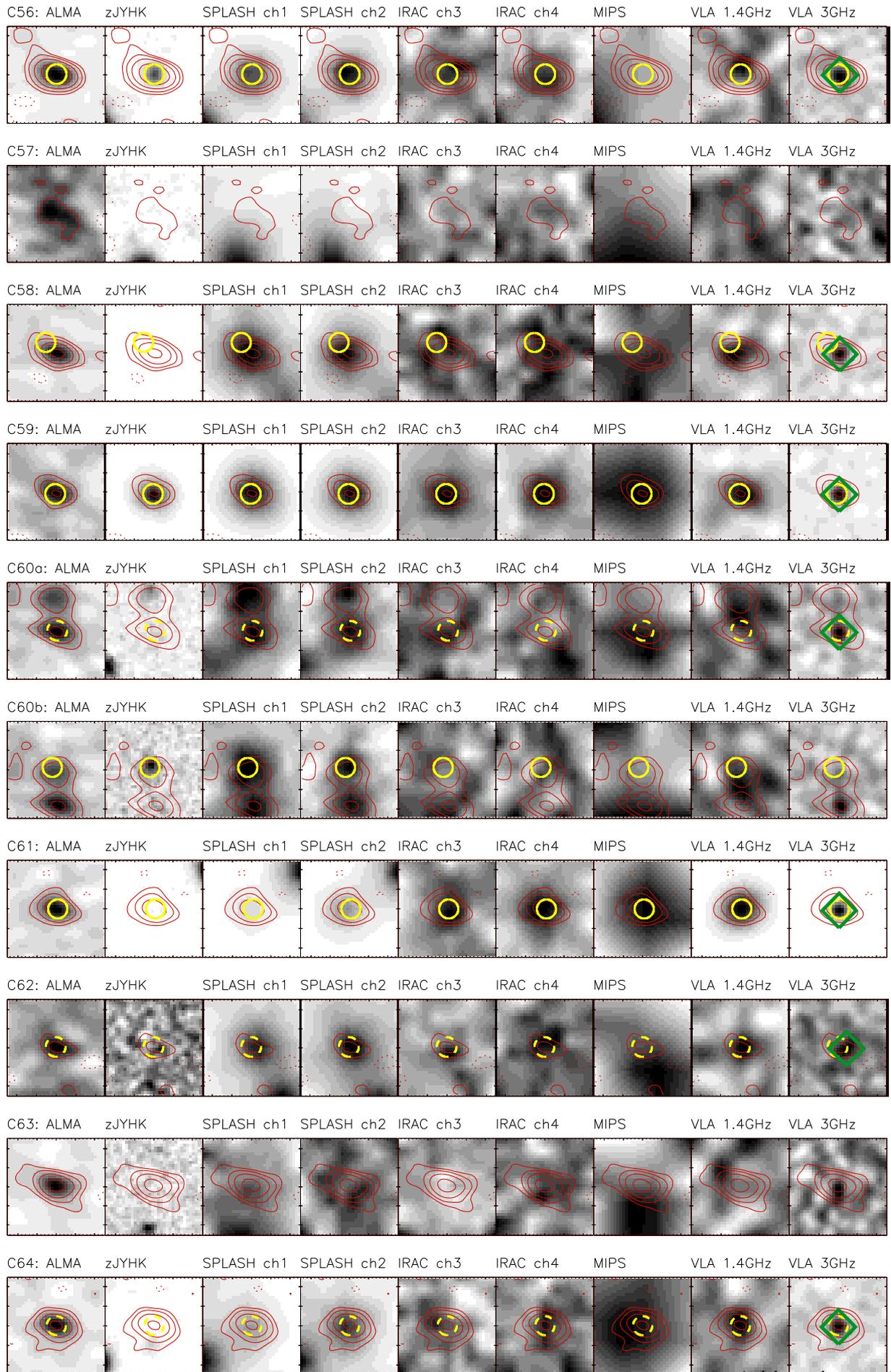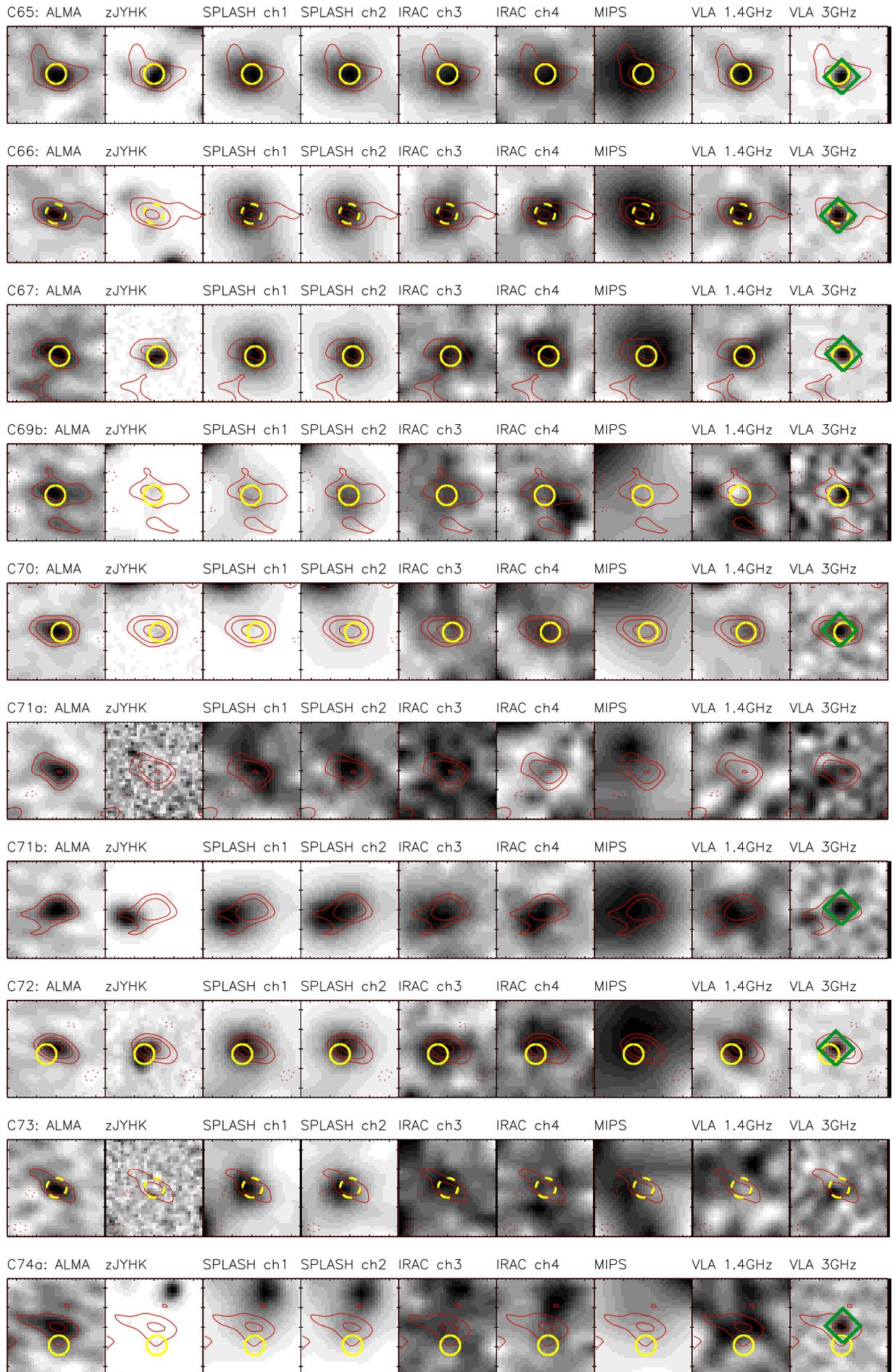
Fig. 10: continued.

Fig. 10: continued.

Fig. 10: continued.

Fig. 10: continued.

Fig. 10: continued.

Fig. 10: continued.
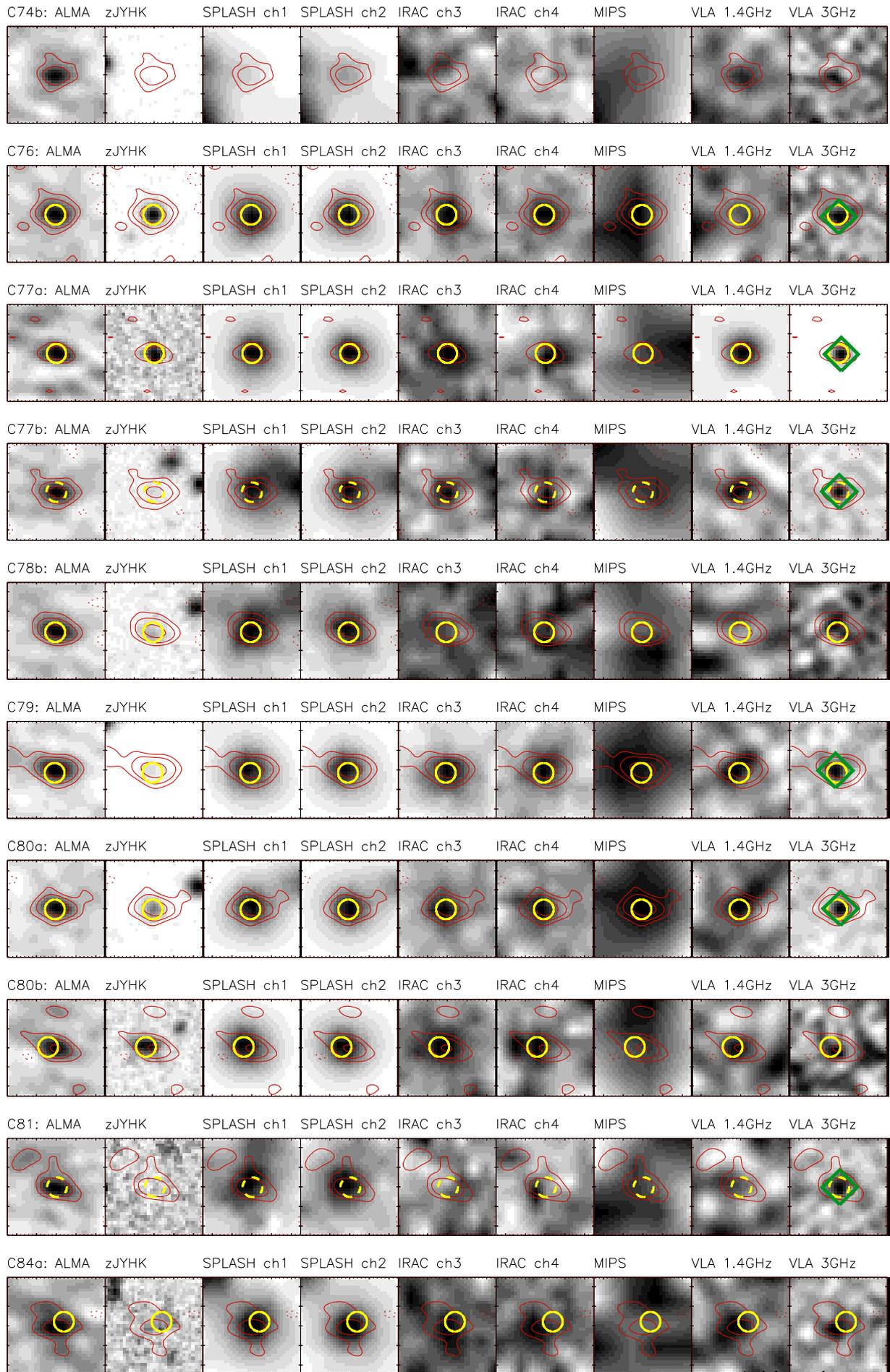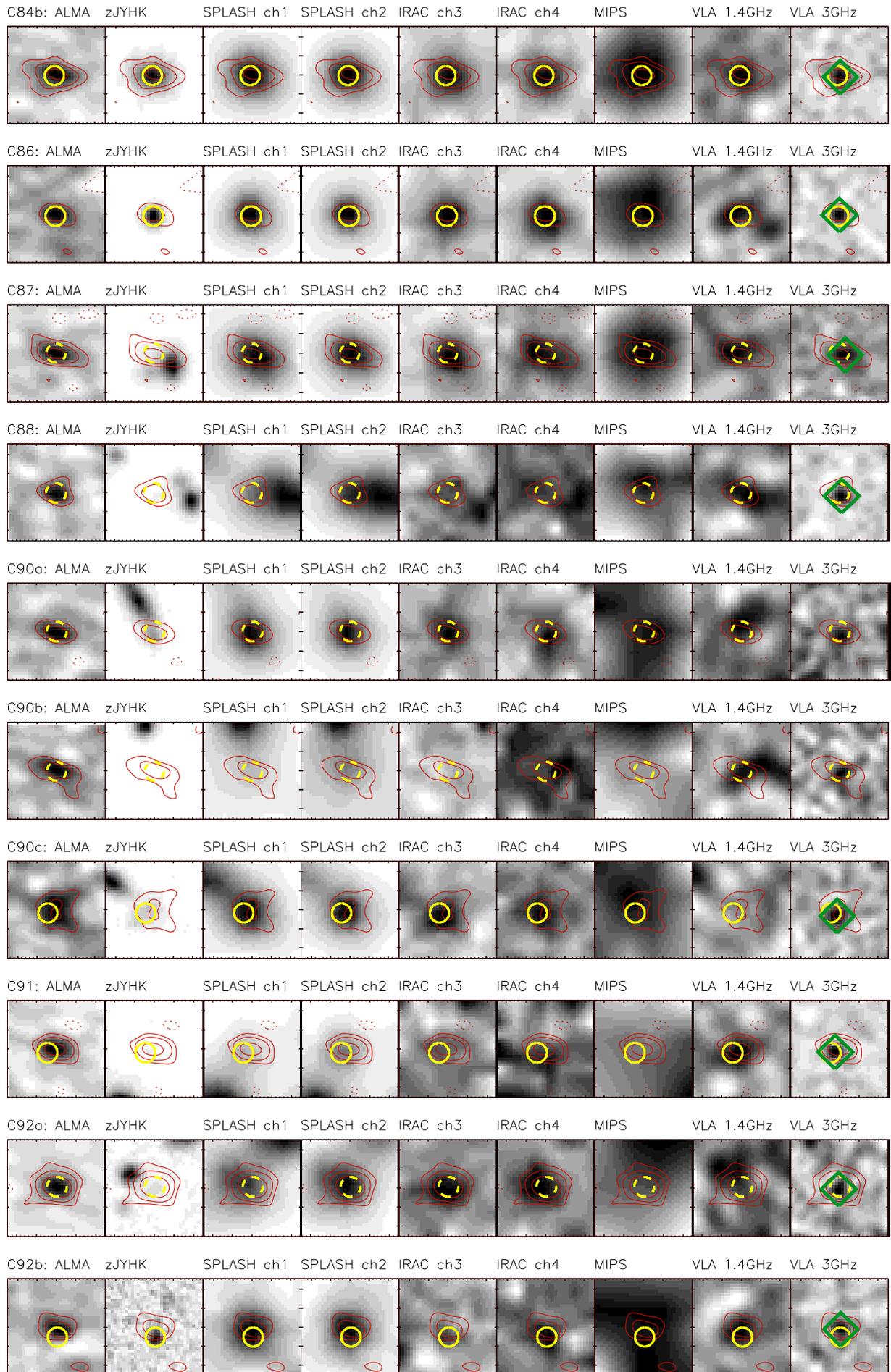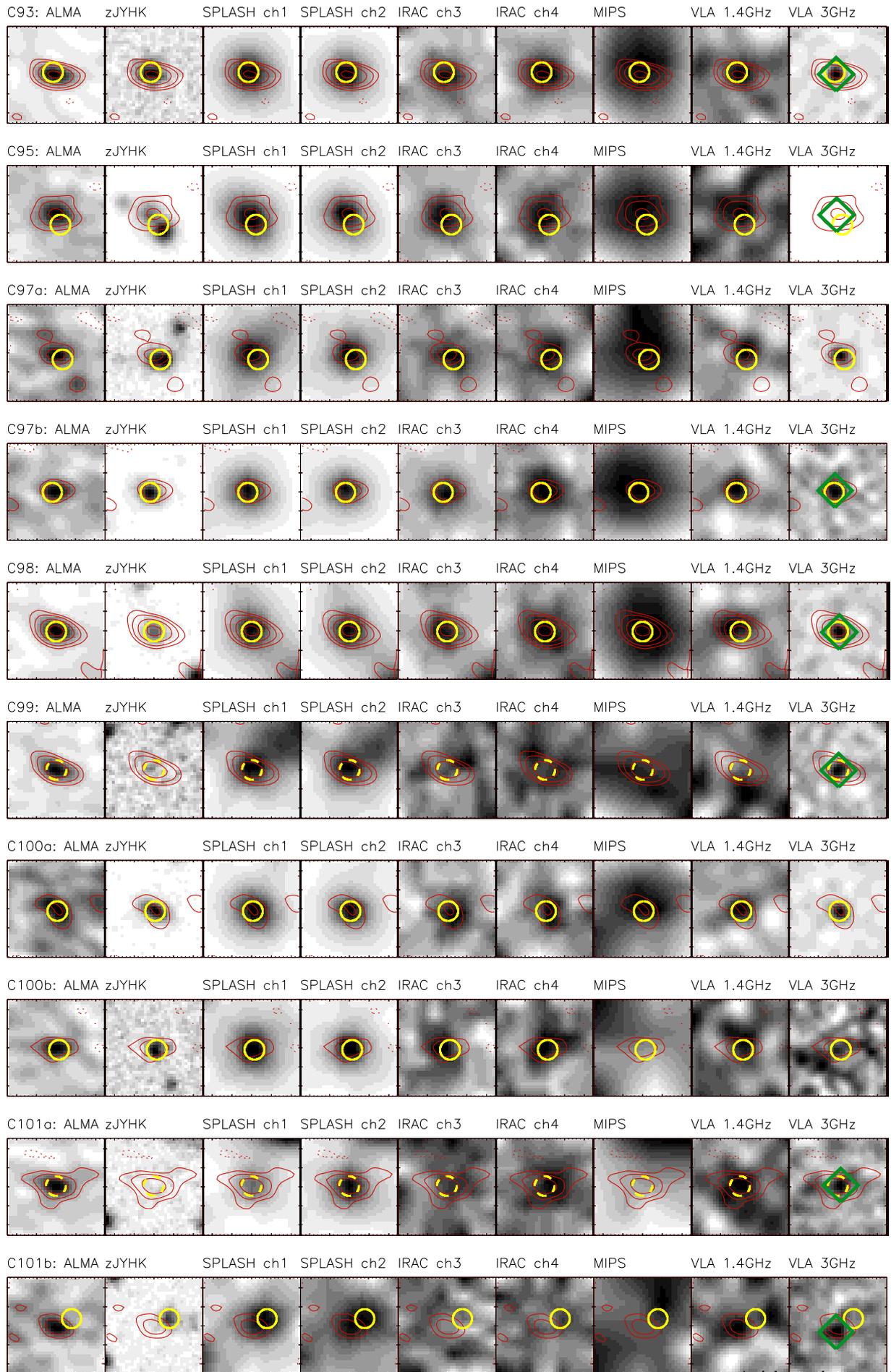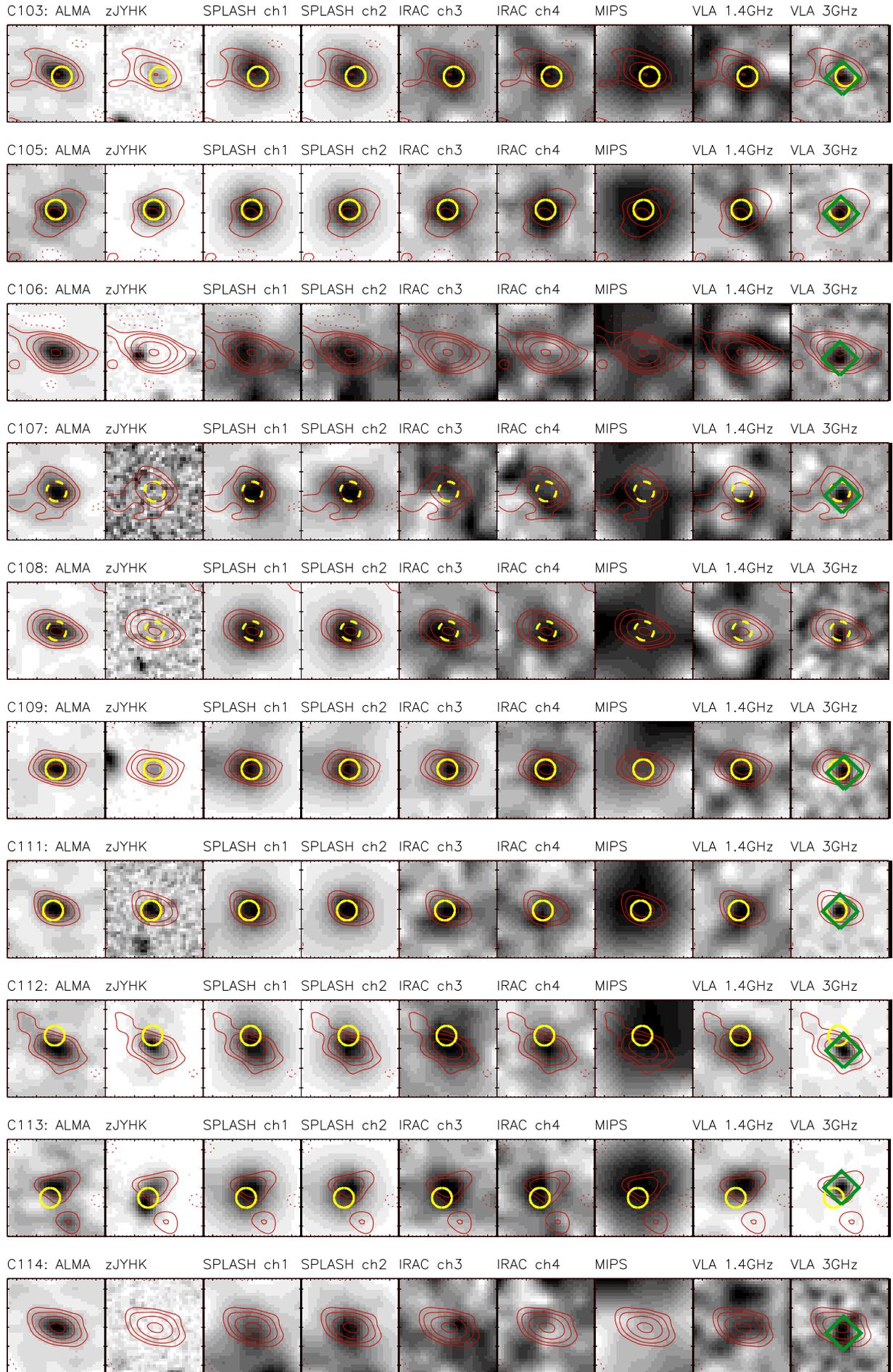
Fig. 10: continued.

Fig. 10: continued.

Fig. 10: continued.

Fig. 10: continued.
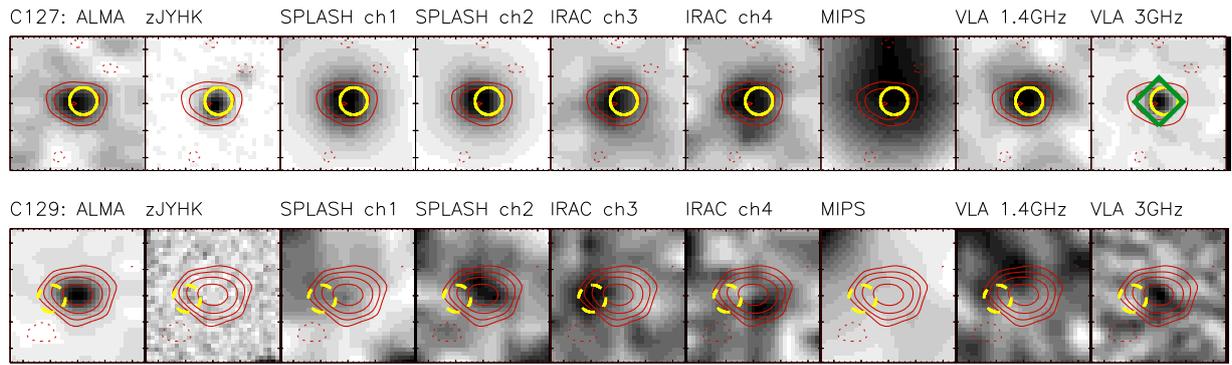
Fig. 10: continued.

:

C93: ALMA   zJYHK   SPLASH ch1   SPLASH ch2   IRAC ch3   IRAC ch4   MIPS   VLA 1.4GHz   VLA 3GHz

C95: ALMA   zJYHK   SPLASH ch1   SPLASH ch2   IRAC ch3   IRAC ch4   MIPS   VLA 1.4GHz   VLA 3GHz

C97a: ALMA   zJYHK   SPLASH ch1   SPLASH ch2   IRAC ch3   IRAC ch4   MIPS   VLA 1.4GHz   VLA 3GHz

C97b: ALMA   zJYHK   SPLASH ch1   SPLASH ch2   IRAC ch3   IRAC ch4   MIPS   VLA 1.4GHz   VLA 3GHz

C98: ALMA   zJYHK   SPLASH ch1   SPLASH ch2   IRAC ch3   IRAC ch4   MIPS   VLA 1.4GHz   VLA 3GHz

C99: ALMA   zJYHK   SPLASH ch1   SPLASH ch2   IRAC ch3   IRAC ch4   MIPS   VLA 1.4GHz   VLA 3GHz

C100a: ALMA zJYHK   SPLASH ch1   SPLASH ch2   IRAC ch3   IRAC ch4   MIPS   VLA 1.4GHz   VLA 3GHz

C100b: ALMA zJYHK   SPLASH ch1   SPLASH ch2   IRAC ch3   IRAC ch4   MIPS   VLA 1.4GHz   VLA 3GHz

C101a: ALMA zJYHK   SPLASH ch1   SPLASH ch2   IRAC ch3   IRAC ch4   MIPS   VLA 1.4GHz   VLA 3GHz

C101b: ALMA zJYHK   SPLASH ch1   SPLASH ch2   IRAC ch3   IRAC ch4   MIPS   VLA 1.4GHz   VLA 3GHz

Fig. 10: continued.

Fig. 10: continued.

:

C115b: ALMA zJYHK   SPLASH ch1   SPLASH ch2   IRAC ch3   IRAC ch4   MIPS   VLA 1.4GHz   VLA 3GHz

C116: ALMA   zJYHK   SPLASH ch1   SPLASH ch2   IRAC ch3   IRAC ch4   MIPS   VLA 1.4GHz   VLA 3GHz

C117: ALMA   zJYHK   SPLASH ch1   SPLASH ch2   IRAC ch3   IRAC ch4   MIPS   VLA 1.4GHz   VLA 3GHz

C118: ALMA   zJYHK   SPLASH ch1   SPLASH ch2   IRAC ch3   IRAC ch4   MIPS   VLA 1.4GHz   VLA 3GHz

C119: ALMA   zJYHK   SPLASH ch1   SPLASH ch2   IRAC ch3   IRAC ch4   MIPS   VLA 1.4GHz   VLA 3GHz

C122a: ALMA zJYHK   SPLASH ch1   SPLASH ch2   IRAC ch3   IRAC ch4   MIPS   VLA 1.4GHz   VLA 3GHz

C122b: ALMA zJYHK   SPLASH ch1   SPLASH ch2   IRAC ch3   IRAC ch4   MIPS   VLA 1.4GHz   VLA 3GHz

C123: ALMA   zJYHK   SPLASH ch1   SPLASH ch2   IRAC ch3   IRAC ch4   MIPS   VLA 1.4GHz   VLA 3GHz

C124: ALMA   zJYHK   SPLASH ch1   SPLASH ch2   IRAC ch3   IRAC ch4   MIPS   VLA 1.4GHz   VLA 3GHz

C126: ALMA   zJYHK   SPLASH ch1   SPLASH ch2   IRAC ch3   IRAC ch4   MIPS   VLA 1.4GHz   VLA 3GHz

Fig. 10: continued.

C127: ALMA zJYHK SPLASH ch1 SPLASH ch2 IRAC ch3 IRAC ch4 MIPS VLA 1.4GHz VLA 3GHz

C129: ALMA zJYHK SPLASH ch1 SPLASH ch2 IRAC ch3 IRAC ch4 MIPS VLA 1.4GHz VLA 3GHz

Fig. 10: continued.

Fig. 11: Total χ^2_{tot} distributions and probability distribution functions (PDF $\propto e^{-0.5\chi^2_{tot}}$) of the photometric redshift for each ALMA SMG with a counterpart in the COSMOS2015 catalog. The red vertical full lines with shown (horizontal) errors indicate the best fit photometric redshift and its 68% confidence interval. The degrees of freedom in the fit are also indicated in the panels. For sources where they are available, synthetic redshift χ^2_{tot} distributions and PDFs are indicated by gray dashed lines.

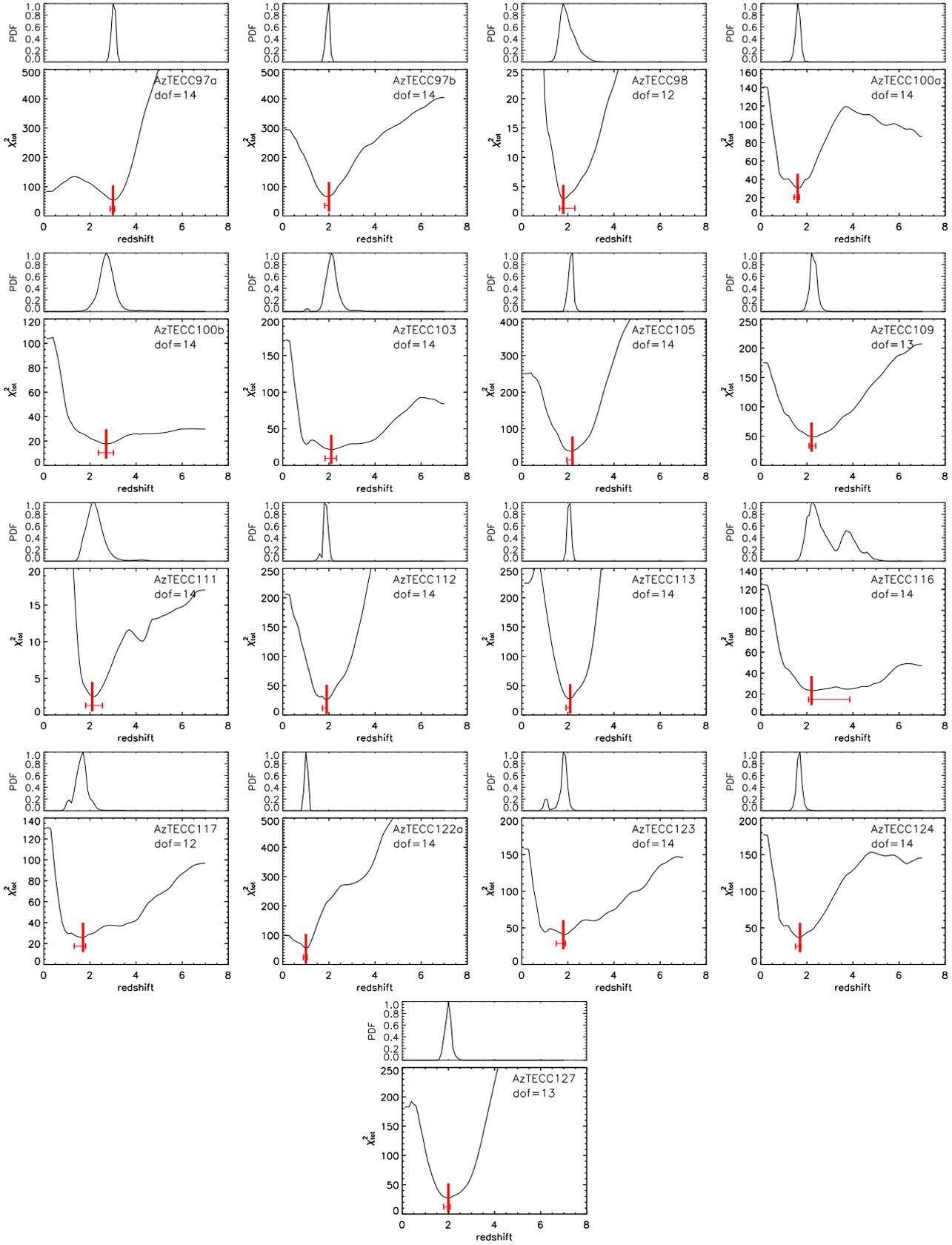Fig. 11: continued.

:
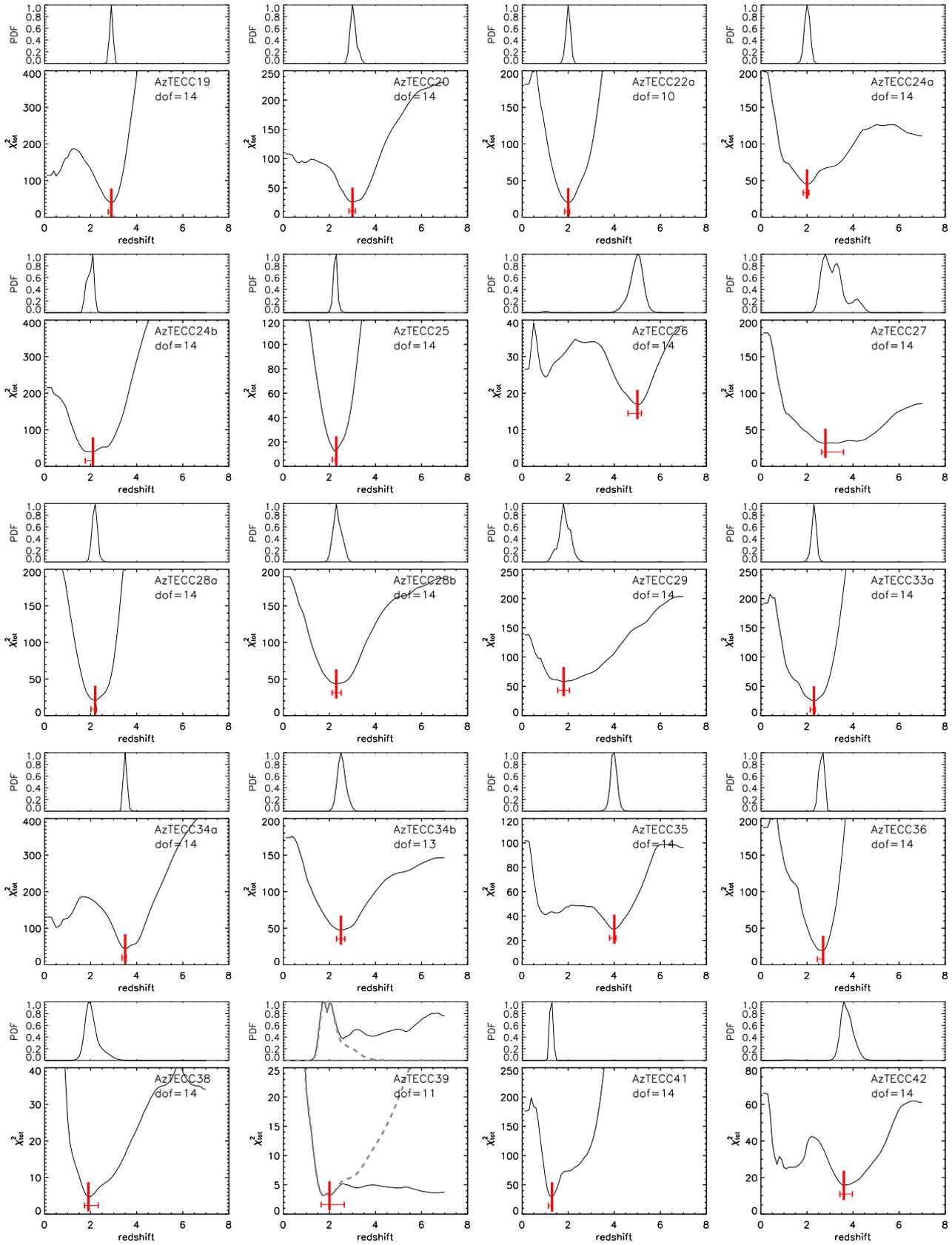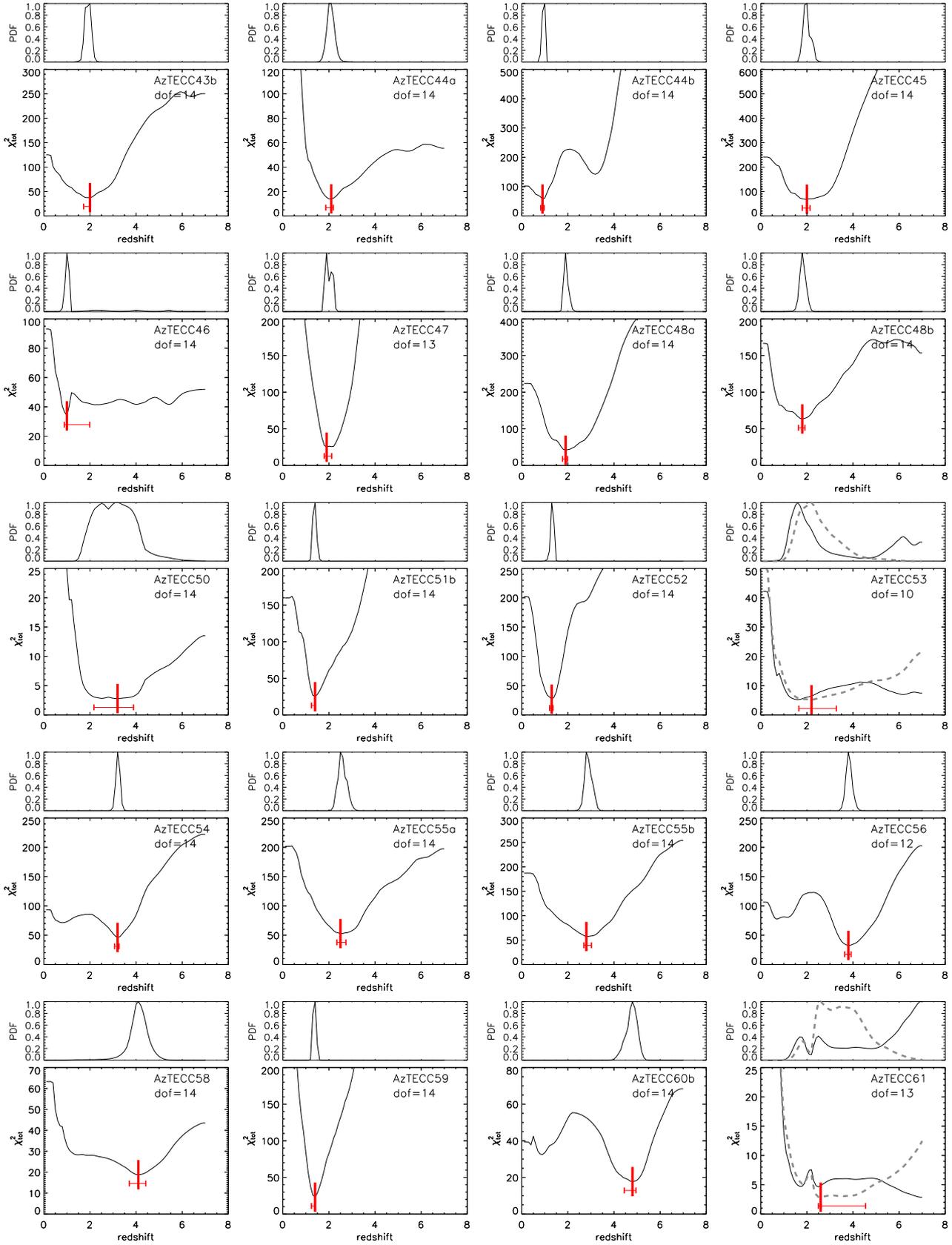
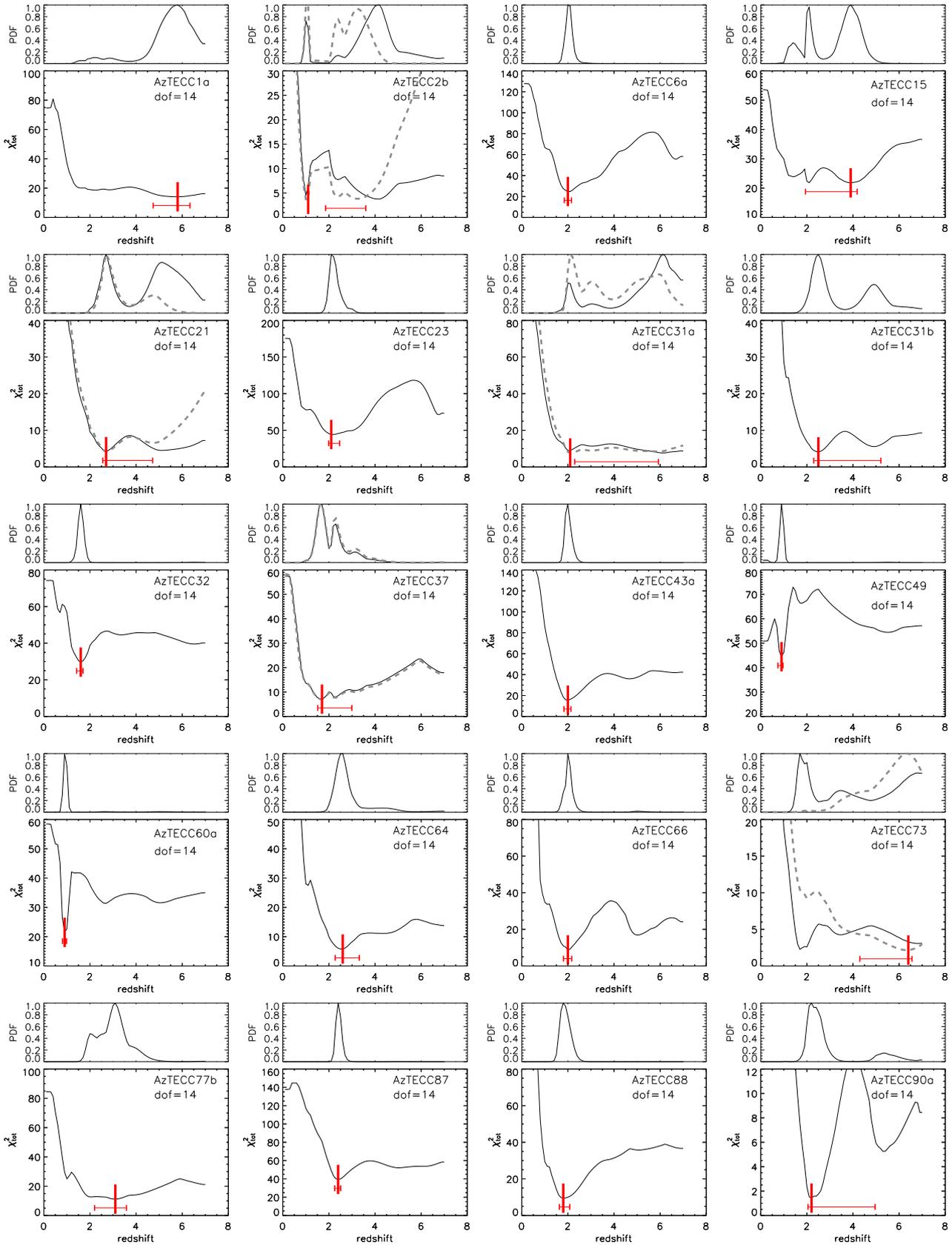Fig. 11: continued.
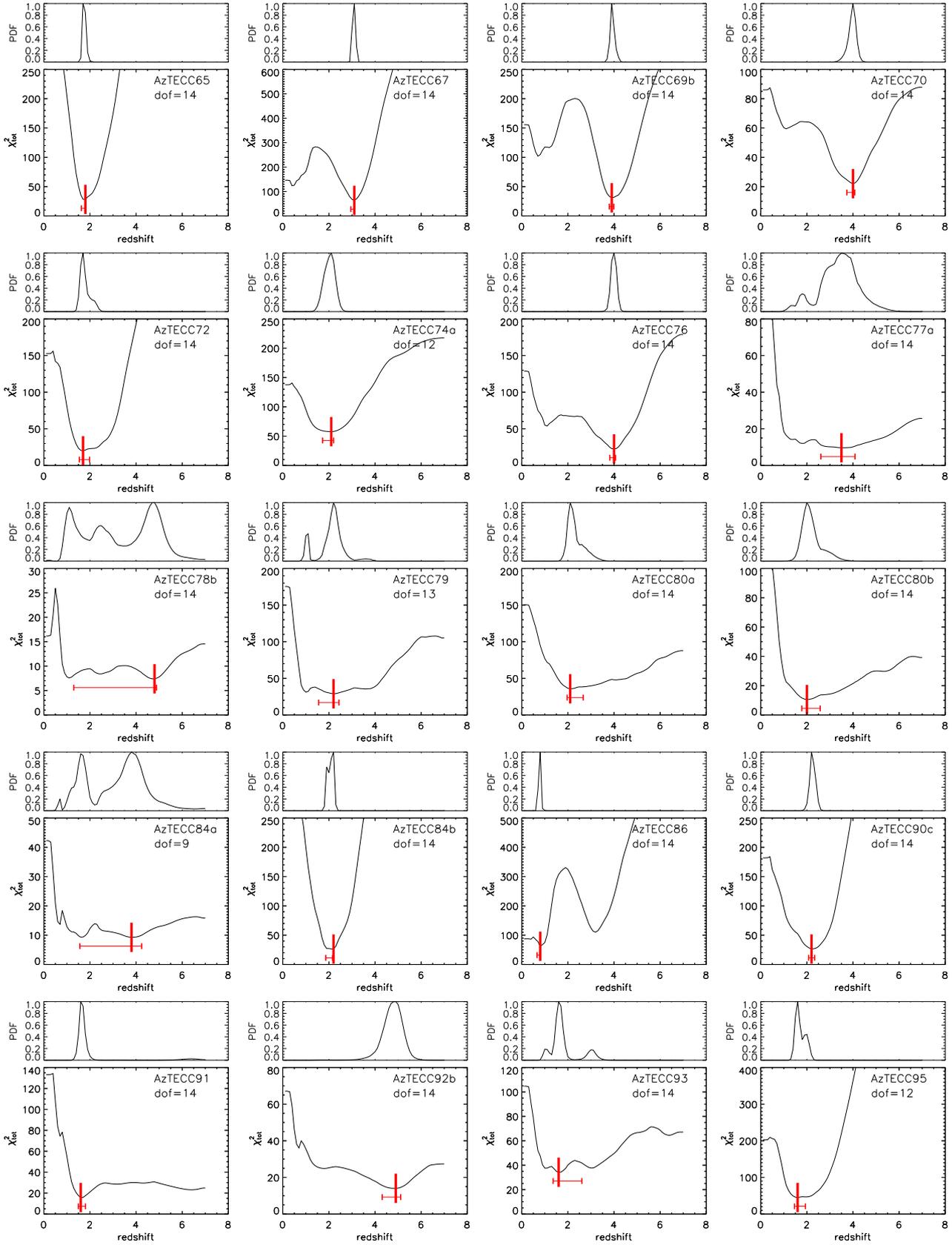
Fig. 11: continued.

Fig. 11: continued.

Fig. 12: The same as Fig. 11, but for sources with specifically extracted photometry (dashed yellow circles in Fig. 10).
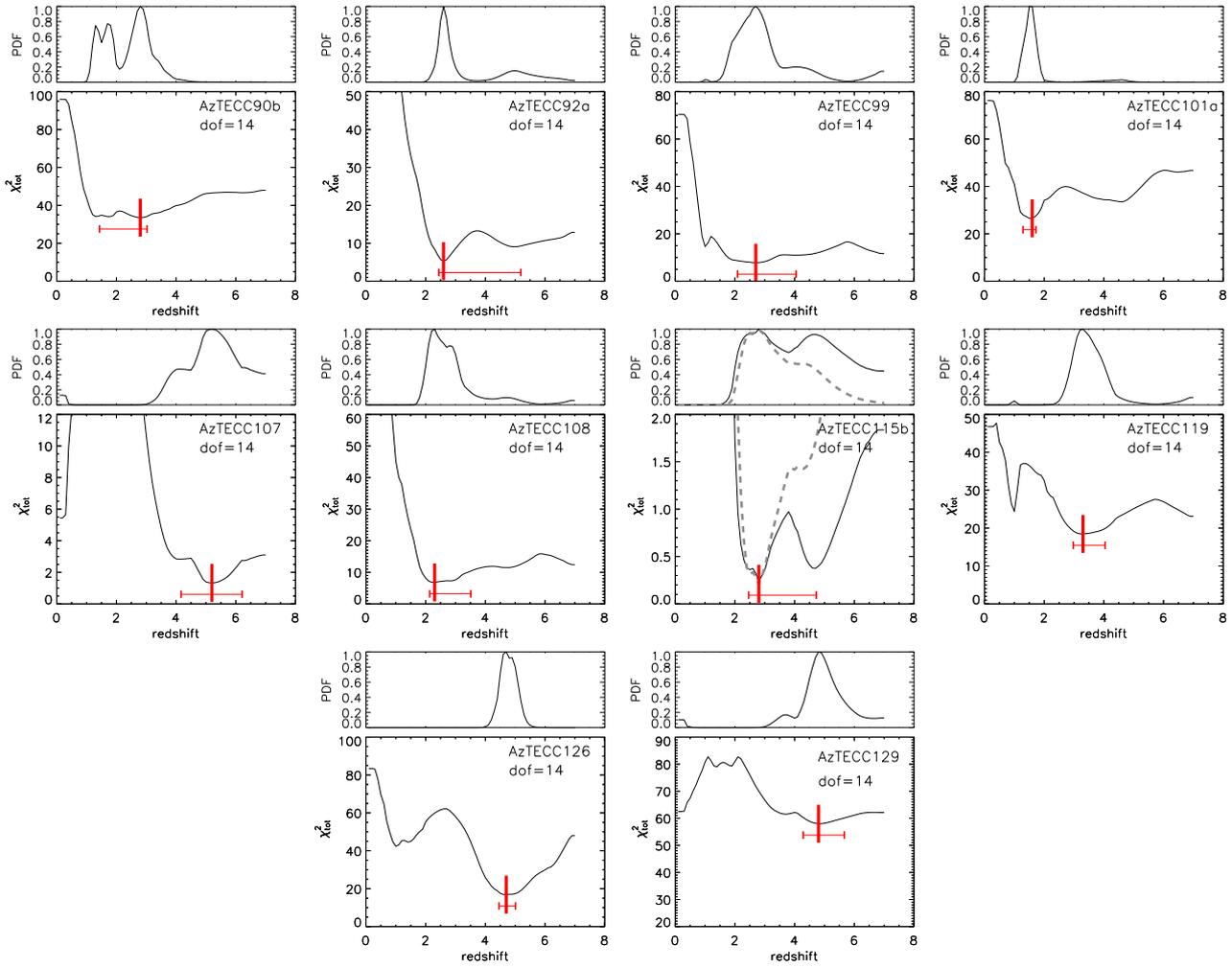
Fig. 12: continued.

:

Fig. 12: continued.